Title

Observational Constraints on Reactive Trace Gas Air-Sea Exchange and Impacts on Atmospheric Chemistry in the Marine Boundary Layer

Author

Kim, Michelle Jee Eun

Publication Date

2015

Peer reviewed|Thesis/dissertation

UNIVERSITY OF CALIFORNIA, SAN DIEGO

Observational Constraints on Reactive Trace Gas Air-Sea Exchange and Impacts on Atmospheric Chemistry in the Marine Boundary Layer

A dissertation submitted in partial satisfaction of the
requirements for the degree Doctor of Philosophy

in

Earth Science

by

Michelle J. Kim

Committee in charge:

Timothy H. Bertram, Chair
Grant B. Deane
Lynn M. Russell
Jeffery Severinghaus
Mark Thiemens

2015

The Dissertation of Michelle J. Kim is approved, and it is acceptable in quality and form for publication on microfilm and electronically:

Chair

University of California, San Diego

2015

DEDICATION

This dissertation is dedicated to my parents.

To my father, who taught me the joy of inquiry for its own sake.

To my mother, who taught me the value of asking meaningful questions.

TABLE OF CONTENTS

LIST OF FIGURES

LIST OF TABLES

ACKNOWLEDGEMENTS

First, I offer my sincere thanks and appreciation to my doctoral advisor, Timothy Bertram. I've enjoyed collaborating with him on such a multi-faceted and engaging project and I've grown to admire his example of scientific creativity, work ethic and collegiality. I would also like to thank my co-advisor, Grant Deane for his continual enthusiasm for interdisciplinary collaborations and atmospheric science. I thank all the current and former members of the Bertram Group for their support, both in and out of science. Finally, I want to offer my heartfelt gratitude to my close friends and family for their encouragement, perspective and good humor that have carried me throughout this degree. I could not have done this work without them.

Chapter 1, in full, is currently being prepared submission for publication of the material. Kim, M.J., Zoerb, M.C., Campbell, N.R., Zimmermann, K.J., Blomquist, B., Huebert, B., and T.H. Bertram. The dissertation author was the primary investigator and author of this paper.

Chapter 2, in full, is currently being prepared for submission for publication of the material. Kim, M. J., Yang, M., Blomquist, B., Huebert, B., and T.H. Bertram. The dissertation author was the primary investigator and author of this paper.

Chapter 3, in full, is a reprint of the material as it appears in Geophysical Research Letters, 2015, with slight modifications. Kim, M.J., Michaud, J. M., Williams, R., Sherwood, B.P., Pomeroy, R., Azam, F., Burkart, M., and T. H. Bertram (2015), "Bacteria-driven production of alkyl nitrates in seawater." *Geophysical*

Research Letters. 42(2), 597-604. The dissertation author was the primary investigator and author of this paper.

Chapter 4, in full, is a reprint of the material as it appears in the *Proceedings of the National Academy of Sciences* 2014 with slight modifications. Kim, M.J., Farmer, D.K., and T.H. Bertram (2014), "A controlling role for the air-sea interface". *Proc. Natl. Acad. Sci. U. S. A.*111:3943-3948. The dissertation author was the primary investigator and author of this paper.

VITA

Education

2005 B.A. Chemistry, Wellesley College

2010 M.S. Civil and Environmental Engineering, Stanford University

2015 Ph.D. Earth Science, University of California, San Diego

Publications

M. J. Kim, et al., (2015) Bacteria driven emissions of alkyl nitrates from the ocean. Geophysical Research Letters, 42, doi:10.1002/2014GL062865.

M. J. Kim, et al., (2014) A controlling role for the air-sea interface in the chemical processing of reactive nitrogen in the coastal marine boundary layer. Proceedings of the National Academy of Sciences of the United States of America. 111(11) 3943-8.

T. Guasco, L. Cuadra-Rodriguez, B. Pedler, A. Ault, D. Collins, D. Zhao, **M. Kim**, M. Ruppel, S. Wilson, R. Pomeroy, V. Grassian, F. Azam, T. Bertram, K. Prather, (2013) Transition metal associations with primary biological particles in sea spray aerosol, Environmental Science & Technology. 48(2), 1324-1333.

K.A. Prather, T.H. Bertram, V.H. Grassian, G.B. Deane, M.D. Stokes, P.J. DeMott, L.I. Aluwihare, B.P. Palenik, F. Azam, J.H. Seinfeld, R.C. Moffet, M.J. Molina, C.D. Cappa, F.M. Geiger, G.C. Roberts, L.M. Russell, A.P. Ault, J. Baltrusaitis, D.B. Collins, C.E. Corrigan, L.A. Cuadra-Rodriguez, C.J. Ebben, S.D. Forestieri, T.L. Guasco, S.P. Hersey, **M. J. Kim**, W. Lambert, R. Modini, W. Mui, B. Pedler, M. Ruppel, O. Ryder, N. Schoepp, R. Sullivan, D. Zhao, (2013) Bringing the ocean into the laboratory to probe the chemical complexity of sea spray aerosol. Proceedings of the National Academy of Sciences of the United States of America. 110 (19) 7550-5.

ABSTRACT OF THE DISSERTATION

Observational Constraints on Reactive Trace Gas Air-Sea Exchange and Impacts on Atmospheric Chemistry in the Marine Boundary Layer

by

Michelle J. Kim

Doctor of Philosophy in Earth Science

University of California, San Diego, 2015

Professor Timothy H. Bertram, Chair

The marine boundary layer (MBL) serves as host to great exchanges of mass and energy across the air-sea interface that drive multi-scale dynamics, biogeochemical cycles and global climate change. Reactive trace gases in the MBL can set the atmosphere's oxidative capacity, aerosol production rates and greenhouse gas warming potential. The ocean surface is a broad source and sink for important reactive trace gases, but direct observations of trace gas air-sea exchange have been limited to a handful of species, to date. This doctoral dissertation addresses this deficit by developing methods for the measurement of reactive trace gas air-sea exchange,

as well as novel observations of air-sea exchange rates of ozone and secondary organic aerosol (SOA) precursors.

Terrestrial biogenic volatile organic compounds (BVOCs) determine global SOA production rates, but estimates of their marine source span several orders of magnitude. A chemical-ionization method for the sensitive detection of BVOC was developed and deployed to the remote MBL aboard a research vessel during the High Wind Gas Exchange Study. Direct observations of BVOC (dimethyl sulfide, isoprene and monoterpene) mixing ratios and air-sea exchange were taken *via* eddy covariance. Dimethyl sulfide and monoterpene air-sea exchange rates were positive (i.e. emitted) in both remote and coastal waters. In coastal areas, monoterpene air-sea exchange rates rivaled dimethyl sulfide.

Reactive nitrogen species (NO_y) including alkyl nitrates ($RONO_2$), dinitrogen pentoxide (N_2O_5) and nitryl chloride ($ClNO_2$) are the main source of nitrogen oxides (NO_x) to the remote MBL and set ozone production rates. During a realistic mesocosm study and detailed laboratory monoculture experiments, alkyl nitrates were found to be driven by heterotrophic bacteria abundance suggesting a dark production mechanism for short-chained $RONO_2$. In an ambient coastal polluted atmosphere, simultaneous eddy covariance measurements of N_2O_5 and $ClNO_2$ air-sea exchange were taken from a pier. Contrary to what was predicted by heterogeneous chemistry, measurements demonstrated that the air-sea interface is a sink for both species, thus a terminal sink for NO_x. Depending on aerosol surface area, this demonstrates the air-sea interface can play a controlling role in NO_x processing in polluted coastal environments.

Introduction

Comprising 71% of global surface area, the majority of the Earth's atmosphere is in direct contact with an ocean surface. The marine boundary layer (MBL) is the site of significant energy and mass transfer processes that dictate its chemical and physical properties (1). Through these turbulent exchange processes, the lower atmosphere and upper-ocean are tightly coupled across various spatial and temporal scales. In the case of trace gas air-sea exchange, the ocean serves as a vast source or sink for these spectroscopically and chemically active trace gases. Trace gases are defined as volatile molecules that make up less than 1% by volume of the atmosphere (2), with water vapor typically excluded due to its variability. This definition includes longer-lived greenhouse gases such as carbon dioxide (CO_2) and methane, as well as short-lived reactive gases such as nitrogen oxides (NO_x) and volatile organic compounds (VOCs).

To date, direct measurements of trace gas air-sea exchange *via* eddy covariance have largely focused on two species closely related to climate change: carbon dioxide and dimethyl sulfide (i.e. (3–13) and others). Eddy covariance is the most direct measure of flux and computed as the variation of a scalar, such as gas mixing ratio (**x'**), with vertical wind (**w**') (14). Despite its conceptual simplicity, instrument capabilities have only recently advanced to meet the stringent instrument requirements of this technique (15). Eddy covariance measurements have driven the most recent advances in the physically-based parameterization of air-sea exchange and its dependence on quickly evolving environmental variables such as wind speed (i.e.

(16)) or bubble exchange/white cap fraction (i.e. (12)), among others. The oceanic uptake of CO_2 is driven by rising atmospheric loadings due to anthropogenic activities and the burning of fossil fuels. With CO_2 in disequilibrium across the air-sea interface, air-sea flux is negative or into the ocean. The dissolution of CO_2 leads to the acidification of sea water, shifts in carbonate chemistry and myriad consequences for marine biogeochemistry (i.e. (17)). Due to its global significance, there is considerable interest in improving physically-based parameterizations of air-sea exchange for global climate models, particularly in poorly constrained high-wind regimes where different models vary by as much as a factor of two (18, 19).

For shorter-lived chemically reactive species, the primary marine trace gas of interest since the 1980's has been dimethyl sulfide (20, 21). DMS is the largest natural source of reduced sulfur to the atmosphere (22). Formed in the water column by marine phytoplankton, most of the planet's surface ocean is supersaturated in DMS leading to its emission to the atmosphere (23) at rate that is estimated between 24-27 Tg S yr^{-1} (24).With an atmospheric lifetime of about 1 day (25), DMS quickly undergoes a series of oxidation steps to form oxidation products that readily condense onto existing aerosol surfaces (26). Models suggest that oceanic DMS emissions account for 18-42% of global sulfate aerosol mass (27, 28). Under select conditions, DMS can initiate new particle formation (29). Both processes have the potential to increase the number of cloud condensation nuclei (CCN) and increase cloud albedo resulting in a cooling effect on global climate (30).

Beyond its implications for climate, DMS air-sea exchange measurements *via* eddy covariance have informed much of the current best practices for direct

measurements of short-lived trace gas air-sea exchange, which today includes (excluding this dissertation) species with critical impacts on oxidant cycling in the remote boundary layer including: acetone, methanol, acetaldehyde, carbon monoxide, ozone, and glyoxal (31–36). This dissertation work expands direct measurements of trace gas air-sea exchange rates to several novel targets with potential significance for atmospheric chemistry and climate change in the MBL. These targets can be categorized into two classes of molecules: biogenic volatile organic compounds (BVOC) and reactive nitrogen (NO_y). The atmospheric and climatic impacts of both molecular classes will be reviewed here.

Biogenic Volatile Organic Compounds (BVOCs)

Biogenic volatile organic compounds (BVOC) are naturally derived non-methane hydrocarbons. Biogenic sources of VOCs outpace anthropogenic sources, with natural emissions contributing 2.5 to 44.5 Tg yr^{-1} to global SOA, while anthropogenic sources add 0.05 to 2.62 Tg yr^{-1} (37). Total global BVOC emissions are dominated by a class of volatiles known as isoprenoids. Isoprenoid compounds such as isoprene (C_5H_8), monoterpenes ($C_{10}H_{16}$) and sesquiterpenes ($C_{15}H_{24}$) are produced mostly by terrestrial plants such as tropical and temperate trees (38, 39). The most strongly emitted BVOC is isoprene, with emissions estimated at 535 Tg yr^{-1}. The classes of isomers known as monoterpenes and sesquiterpenes are estimated to emit in lower quantities (162 Tg yr^{-1} and 29 Tg yr^{-1} respectively). However, due to their higher reactivity, the latter molecules play a disproportionate role in driving global SOA formation (40).

Like their terrestrial counterparts, marine photosynthetic organisms, such as phytoplankton and other marine flora, are also known to produce isoprenoids (41–44). Originally, the physiological purpose of isoprenoids were not readily apparent and the metabolic dedication of carbon and energy to the formation of these compounds was poorly understood (45). The current understanding of isoprenoids is that they serve as protective and signaling molecules among terrestrial and marine autotrophs (46). Laboratory experiments have demonstrated that the marine production of isoprenoids are increased under heat or oxidative stress (47) with emission rates varying between taxa, species and even strain. This environmental dependence has prompted questions about BVOC's importance in future, warmer climates (48).

In-situ measurements of marine isoprene and monoterpenes, in either the ambient atmosphere or dissolved in seawater, are few (49). Additionally, atmospheric measurements are typically based from coastal sampling locations where relatively weak sources of terrestrial BVOCs could be potentially significant interferences on scale with typical marine mixing ratios. Due to the overall paucity of these ambient measurements, especially in the remote MBL, global models of marine isoprenoid emissions are poorly constrained (50–53) with estimates of global marine emissions spanning several orders of magnitude.

Reactive Nitrogen

Total reactive nitrogen species (NO_y including NO_x, N_2O_5, $ClNO_2$, alkyl nitrates, nitric acid and others) are formed from various reactions of NO_x, a critical tropospheric ozone precursor and pollutant. NO_y species act as temporary NO_x

reservoirs, sequestering NO_x in their formation or releasing it upon their chemical, thermal or photolytic breakdown. Due to their greater stability and lifetime relative to NO_x, their formation and subsequent transport can result in the redistribution of NO_x to pristine regions and drive ozone production in the NO_x limited MBL. Their reactivity with condensed phase surfaces such as aerosol particles can also have a variety of impacts on pollutants, atmospheric radicals and other environmental impacts, such as acid rain. This work studies the behavior of two reactive nitrogen species in MBL: short-chained alkyl nitrates ($RONO_2$) production by marine biota and dinitrogen pentoxide (N_2O_5) removal by the sea surface in coastal polluted regions.

Alkyl nitrates are temporary NO_x reservoirs. They sequester NO_x in the atmosphere by a chain termination reaction between an alkyl peroxy radicals (RO_2) and nitric oxide (NO). Longer chained alkyl groups (R) are favored by this mechanism due to their increased product stability and resistance to thermal degradation (54). However, short-chained alkyl nitrates (C1-C4) had been observed in the remote boundary layer (55–57) and sea water samples demonstrated that the ocean is supersaturated with respect to short-chained alkyl nitrates (58, 59) suggesting that the ocean could serve as a broad, diffuse source of short-chained alkyl nitrates to the MBL. The potential global marine source of methyl- and ethyl- nitrates have been estimated to contribute 1 Dobson Unit of O_3 in the NO_x limited MBL or a 2.4% reduction in the lifetime of methane (60). Later studies outlined an explicit photochemical production mechanism for the production of short-chained alkyl nitrates in the mixed layer (61). However, elevated concentrations of alkyl nitrates below mixed layer (62) strongly suggest an unexplained dark production mechanism.

Dinitrogen pentoxide (N_2O_5) is a also a NO_x reservoir generated at night from the chain termination of two oxidation products of NO_x; nitrogen dioxide (NO_2) and the nitrate radical (NO_3). The nighttime removal of N_2O_5 and the nitrate radical (NO_3) collectively account for up to 50% of NO_x removal overnight (63). However, the overall impact on NO_x depends on the various N_2O_5 loss processes, each of which have vastly different impacts on the NO_x and halogen budget (i.e. (64)). N_2O_5 uptake by sea-spray aerosol surface has been explored for its impacts on halogen activation and NO_x reformation through the formation of nitryl chloride, $ClNO_2$ (65). Despite the physicochemical parallels between the air-sea interface and sea-spray aerosol surfaces, surface reactions on the ocean surface had not been previously considered for its impact on N_2O_5 and $ClNO_2$ reactivity, nor the NO_x or halogen budgets.

This dissertation presents advances in the measurement of BVOCs utilizing a custom field-deployable chemical-ionization time-of-flight mass spectrometry (CI-ToFMS) (Chapter 1) and its performance over 2.5 months in the remote MBL measuring BVOC air-sea exchange *via* eddy covariance (Chapter 2). It also features a controlled mechanistic investigation into the production of short-chained alkyl nitrates by marine bacteria in monocultures, as well as a physically realistic mesocosm (Chapter 3). Finally, I provide the first observations of the air-sea exchange of N_2O_5 and $ClNO_2$, a reactant-product pair, to explore their surface reactions at the air-sea interface and its impact on the NO_x budget in a polluted coastal environment (Chapter 4). These observations offer noteworthy insights into the role of the surface ocean as a source and sink of reactive trace gas species, with important implications for atmospheric chemistry and climate in both remote and coastal marine regimes.

References

1. Fairall CW, Bradley EF, Rogers DP, Edson JB, Young GS (1996) Bulk parameterization of air-sea fluxes for Tropical Ocean-Global Atmosphere Coupled-Ocean Atmosphere Response Experiment. *J Geophys Res* 101:3747.

2. Seinfeld JH, Pandis SN (2006) *Atmospheric Chemistry and Physics: From Air Pollution to Climate Change*.

3. McGillis WR, Edson JB, Hare JE, Fairall CW (2001) Direct covariance air-sea CO2 fluxes. *J Geophys Res* 106(2000):16729 – 16745.

4. Miller S, Marandino C, De Bruyn W, Saltzman ES (2009) Air-sea gas exchange of CO2 and DMS in the North Atlantic by eddy covariance. *Geophys Res Lett* 36.

5. Marandino CA, De Bruyn WJ, Miller SD, Saltzman ES (2008) DMS air/sea flux and gas transfer coefficients from the North Atlantic summertime coccolithophore bloom. *Geophys Res Lett* 35:- ST – DMS air/sea flux and gas transfer coeffici.

6. Marandino CA, De Bruyn WJ, Miller SD, Saltzman ES (2009) Open ocean DMS air/sea fluxes over the eastern South Pacific Ocean. *Atmos Chem Phys* 9:345–356.

7. Bell TG, et al. (2013) Air-sea dimethylsulfide (DMS) gas transfer in the North Atlantic: Evidence for limited interfacial gas exchange at high wind speed. *Atmos Chem Phys* 13:11073–11087.

8. Bell TG, et al. (2015) Dimethylsulfide gas transfer coefficients from algal blooms in the Southern Ocean. *Atmos Chem Phys* 15(1):1783–1794.

9. Yang M, Blomquist BW, Huebert BJ (2009) Constraining the concentration of the hydroxyl radical in a stratocumulus- topped marine boundary layer from sea-to-air eddy covariance flux measurements of dimethylsulfide. *Atmos Chem Phys* 9(23):9225–9236.

10. Yang M, Blomquist BW, Fairall CW, Archer SD, Huebert BJ (2011) Air-sea exchange of dimethylsulfide in the Southern Ocean: Measurements from so GasEx compared to temperate and tropical regions. *J Geophys Res Ocean* 116.

11. Huebert BJ, et al. (2004) Measurement of the sea-air DMS flux and transfer velocity using eddy correlation. *Geophys Res Lett* 31(23):L23113.

12. Blomquist BW, Fairall CW, Huebert BJ, Kieber DJ, Westby GR (2006) DMS sea-air transfer velocity: Direct measurements by eddy covariance and parameterization based on the NOAA/COARE gas transfer model. *Geophys Res Lett* 33:L07601.

13. Blomquist BW, Huebert BJ, Fairall CW, Faloona IC (2010) Determining the sea-air flux of dimethylsulfide by eddy correlation using mass spectrometry. *Atmos Meas Tech* 3(1):1–20.

14. Baldocchi D, Hincks B, Meyers T (1988) Measuring biosphere-atmosphere exchanges of biologically related gases with micrometeorological methods. *Ecology* 69(5):1331–1340.

15. Rowe MD, Fairall CW, Perlinger J a. (2011) Chemical sensor resolution requirements for near-surface measurements of turbulent fluxes. *Atmos Chem Phys* 11(11).

16. Wanninkhof R, McGillis WR (1999) A cubic relationship between air- sea CO2 exchange and wind speed. *Geophys Res Lett* 26:1889–1892.

17. Doney SC, Fabry VJ, Feely RA, Kleypas JA (2009) Ocean Acidification: The Other CO 2 Problem. *Ann Rev Mar Sci* 1:169–192.

18. Ho DT, et al. (2006) Measurements of air-sea gas exchange at high wind speeds in the Southern Ocean: Implications for global parameterizations. *Geophys Res Letters*.

19. Blomquist BW, et al. (2014) Advances in Air-Sea CO2 Flux Measurement by Eddy Correlation. *Boundary-Layer Meteorol*.

20. Charlson RJ, Lovelock JE, Andreae MO, Warren SG (1987) Oceanic phytoplnakton, atmospheric sulphur, cloud albedo and climate. *Nature* 326(16):655–661.

21. Quinn PK, Bates TS (2011) The case against climate regulation via oceanic phytoplankton sulphur emissions. *Nature* 480(7375):51–56.

22. Watts SF (2000) The mass budgets of carbonyl sulfide, dimethyl sulfide, carbon disulfide and hydrogen sulfide. *Atmos Environ* 34:761–779.

23. Kettle AJ, Andreae MO (2000) Flux of dimethylsulfide from the oceans: A comparison of updated data sets and flux models. *J Geophys Res* 105:26793.

24. Boucher O, et al. (2002) Sensitivity study of dimethylsulphide (DMS) atmospheric concentrations and sulphate aerosol indirect radiative forcing to the

DMS source representation and oxidation. *Atmos Chem Phys Discuss* 2(2000):1181–1216.

25. Keller MD, Bellows WK, Guillard RRL (1989) Dimethyl sulfide production in marine phytoplankton. *Biogenic Sulfur in the Environment. ACS Symposium Series*, pp 167–182.

26. Ayers GP, Gras JL (1991) Seasonal relationship between cloud condensation nuclei and aerosol methanesulphonate in marine air. *Nature* 354:56–58.

27. Chin M, et al. (1996) A global three-dimensional model of tropospheric sulfate. *J Geophys Res Atmos* 101:D13, 18667-18690.

28. Gondwe M (2003) The contribution of ocean-leaving DMS to the global atmospheric burdens of DMS, MSA, SO 2 , and NSS SO 4 =. *Global Biogeochem Cycles* 17(2):25–1.

29. Clarke a. D, et al. (1998) Particle production in the remote marine atmosphere: Cloud outflow and subsidence during ACE 1. *J Geophys Res* 103:16397.

30. Twomey S (1977) The influence of pollution on the shortwave albedo of clouds. *J Atmos Sci*.

31. Yang M, Beale R, Smyth T, Blomquist BW (2013) Vertical fluxes and atmospheric cycling of methanol, acetaldehyde, and acetone in a coastal environment. *Atmos Chem Phys Discuss* 13(3):8101–8152.

32. Yang M, et al. (2013) Atmospheric deposition of methanol over the Atlantic Ocean. *Proc Natl Acad Sci U S A* 110(50):20034–9.

33. Yang M, Blomquist BW, Nightingale PD (2014) Air-sea exchange of methanol and acetone during HiWinGS: Estimation of air phase, water phase gas transfer velocities. *J Geophys Res Ocean* 119(10):7308–7323.

34. Bariteau L, et al. (2010) Determination of oceanic ozone deposition by ship-borne eddy covariance flux measurements. *Atmos Meas Tech* 3:441–455.

35. Coburn S, Ortega I, Thalman R, Blomquist B, Fairall CW (2014) Measurements of diurnal variations and Eddy Covariance (EC) fluxes of glyoxal in the tropical marine boundary layer : description of the Fast LED-CE-DOAS instrument. *Atmos Meas Tech* 7:3579-3595.

36. Blomquist BW, Fairall CW, Huebert BJ, Wilson ST (2012) Direct measurement of the oceanic carbon monoxide flux by eddy correlation. *Atmos Meas Tech* 5(12):3069–3075.

37. Tsigaridis K, Kanakidou M (2007) Secondary organic aerosol importance in the future atmosphere. *Atmos Environ* 41:4682–4692.

38. Guenther AB, et al. (2012) The model of emissions of gases and aerosols from nature version 2.1 (MEGAN2.1): An extended and updated framework for modeling biogenic emissions. *Geosci Model Dev* 5(6):1471–1492.

39. Guenther A, et al. (2006) Estimates of global terrestrial isoprene emissions using MEGAN (Model of Emissions of Gases and Aerosols from Nature). *Atmos Chem Phys* 6(1):107–173.

40. Sakulyanontvittaya T, et al. (2008) Monoterpene and sesquiterpene emission estimates for the United States. *Environ Sci Technol* 42(5):1623–1629.

41. Shaw SL, Chisholm SW, Prinn RG (2003) Isoprene production by Prochlorococcus, a marine cyanobacterium, and other phytoplankton. *Mar Chem* 80:227–245.

42. Colomb A, Yassaa N, Williams J, Peeken I, Lochte K (2008) Screening volatile organic compounds (VOCs) emissions from five marine phytoplankton species by head space gas chromatography/mass spectrometry (HS-GC/MS). *J Environ Monit* 10(3):325–30.

43. Yassaa N, et al. (2008) Evidence for marine production of monoterpenes. *Environ Chem* 5(6):391.

44. Meskhidze N, Sabolis a., Reed R, Kamykowski D (2015) Quantifying environmental stress-induced emissions of algal isoprene and monoterpenes using laboratory measurements. *Biogeosciences* 12(3):637–651.

45. Exton D a., McGenity TJ, Steinke M, Smith DJ, Suggett DJ (2015) Uncovering the volatile nature of tropical coastal marine ecosystems in a changing world. *Glob Chang Biol* 21(4):1383–1394.

46. Loreto F, Fineschi S (2014) Reconciling functions and evolution of isoprene emission in higher plants. *New Phytol*:578–285.

47. Exton DA, Suggett DJ, Mcgenity TJ, Steinke M (2013) Chlorophyll-normalized isoprene production in laboratory cultures of marine microalgae and implications for global models. *Limnol Oceanogr* 58(4):1301–1311.

48. Rinnan R, Steinke M, McGenity T, Loreto F (2014) Plant volatiles in extreme terrestrial and marine environments. *Plant Cell Environ*:1776–1789.

49. Shaw SL, Gantt B, Meskhidze N (2010) Production and Emissions of Marine Isoprene and Monoterpenes: A Review. *Adv Meteorol* 2010(1):1–24.

50. Arnold SR, et al. (2009) Evaluation of the global oceanic isoprene source and its impacts on marine organic carbon aerosol. *Atmos Chem Phys* 9(4):1253–1262.

51. Palmer PI, Shaw SL (2005) Quantifying global marine isoprene fluxes using MODIS chlorophyll observations. *Geophys Res Lett* 32(9):1–5.

52. Gantt B, Meskhidze N, Kamykowski D (2009) A new physically-based quantification of marine isoprene and primary organic aerosol emissions. *Atmos Chem Phys* 9:4915–4927.

53. Luo G, Yu F (2010) A numerical evaluation of global oceanic emissions of α-pinene and isoprene. *Atmos Chem Phys* (2008):2007–2015.

54. Arey J, Aschmann SM, Kwok ESC, Atkinson R (2001) Alkyl Nitrate , Hydroxyalkyl Nitrate , and Hydroxycarbonyl Formation from the NO x -Air Photooxidations of C 5 -C 8 n-Alkanes. *J Phys Chem A* 105:1020–1027.

55. Atlas E, Pollock W, Greenberg J, Heidt L, Thompson AM (1993) Alkyl nitrates, nonmethane hydrocarbons, and halocarbon gases over the equatorial Pacific Ocean during SAGA 3. *J Geophys Res* 98:16933.

56. Blake N, Blake D (1999) Aircraft measurements of the latitudinal, vertical, and seasonal variations of NMHCs, methyl nitrate, methyl halides, and DMS during the First Aerosol Characterization. *J Geophys Res* 104.

57. Blake NJ (2003) Latitudinal, vertical, and seasonal variations of C1-C4 alkyl nitrates in the troposphere over the Pacific Ocean during PEM-Tropics A and B: Oceanic and continental sources. *J Geophys Res* 108.

58. Chuck AL, Turner SM, Liss PS (2002) Direct evidence for a marine source of C1 and C2 alkyl nitrates. *Science* 297:1151–1154.

59. Dahl EE, Yvon-Lewis SA, Saltzman ES (2005) Saturation anomalies of alkyl nitrates in the tropical Pacific Ocean. *Geophys Res Lett* 32:1–4.

60. Neu JL, Lawler MJ, Prather MJ, Saltzman ES (2008) Oceanic alkyl nitrates as a natural source of tropospheric ozone. *Geophys Res Lett* 35.

61. Dahl EE, Saltzman ES (2008) Alkyl nitrate photochemical production rates in North Pacific seawater. *Mar Chem* 112:137–141.

62. Dahl EE, Yvon-Lewis S a., Saltzman ES (2007) Alkyl nitrate (C 1 -C 3) depth profiles in the tropical Pacific Ocean. *J Geophys Res* 112(C1):C01012.

63. Alexander B, et al. (2009) Quantifying atmospheric nitrate formation pathways based on a global model of the oxygen isotopic composition (Δ17O) of atmospheric nitrate. *Atmos Chem Phys Discuss* 9:5043–5056.

64. Bertram TH, Thornton JA (2009) Toward a general parameterization of N(2)O(5) reactivity on aqueous particles: the competing effects of particle liquid water, nitrate and chloride. *Atmos Chem Phys* 9:8351–8363 ST – Toward a general parameterization .

65. Finlayson-Pitts B, Ezell M, Pitts J (1989) Formation of chemically active chlorine compounds by reactions of atmospheric NaCl particles with gaseous N2O5 and ClONO2. *Nature*.

Chapter 1

Revisiting benzene dimer cations for the chemical ionization of volatile organic compounds

Benzene dimer cations were revisited as a sensitive reagent ion for the chemical ionization of novel and previously known volatile organic compounds (VOCs). Calibration experiments on a chemical ionization time-of-flight mass spectrometer (CI-ToFMS) demonstrated high sensitivity (>1 normalized counts per second/ppt or nCPS/ppt) and accuracy (10%) to dimethyl sulfide, isoprene, and α-pinene. Parallel measurements on a chemical-ionization quadrupole mass spectrometer with weaker declustering energy demonstrated that ion-molecule reactions likely proceed through a combination of ligand-switching and direct charge transfer mechanisms. Laboratory tests indicate that benzene cations can be used for the selective measurement of sesquiterpenes, where minimal fragmentation was observed for the detection of bicyclic sesquiterpenes (e.g., ß-caryophyllene). The field stability of benzene dimer cations was tested on the CI-ToFMS during a 2.5 month cruise, the last five weeks as part of the High Wind Gas Exchange Study (HiWinGS). During HiWinGS, benzene dimer cations were validated for the detection of dimethyl sulfide against an atmospheric pressure ionization mass spectrometer (APIMS).

Measurements showed excellent agreement ($R^2 = 0.80$) over a wide range of sampling conditions.

1. Introduction

Volatile organic compounds (VOCs) play a central role in atmospheric chemistry, where they can regulate tropospheric ozone and secondary organic aerosol (SOA) production rates (1). Global emissions of non-methane VOCs are dominated by biogenic terpenes, where isoprene (C_5H_8) and monoterpenes (MT; $C_{10}H_{16}$) emissions have been shown to be most significant in terrestrial regions (2). Recent studies have shown that sesquiterpenes (SQT; C_{15} H_{24}) may also play a significant role in secondary organic aerosol production (3), but far less is known about their global emission rates (4, 5). In one of few studies with simultaneous measurements of isoprene, MT, and SQT, Kim et al., inferred ecosystem scale fluxes that suggest that SQT fluxes could be as much as 50% that of MT in deciduous forests (6). The condensable oxidation products of terpenes has been shown to dominate SOA mass in terrestrial regions, particularly in boreal and sub-tropical forests, where monoterpenes and isoprene dominate VOC emissions (4). In contrast, SOA precursors in the marine boundary layer have historically been thought to be dominated by dimethyl sulfide (DMS) emissions, with isoprene and monoterpenes contributing less than 1% to overall marine SOA mass (7).

Due to their reactivity, short lifetimes, and trace abundance, chemical ionization mass spectrometers (CIMS) are increasingly utilized as a fast, sensitive and selective measurement technique for reactive trace gas species (8). These benefits are more pronounced on moving platforms, in pristine environments or instrumentally-tasking methods such eddy covariance. Proton transfer mass spectrometry (PTR-MS) has been used extensively for the sensitive, selective determination of VOCs providing

direct measurements of concentrations and turbulent fluxes from a variety of mobile platforms. While successful in the measurement of small molecules such as DMS and isoprene, PTR-MS detection of larger volatile organic compounds, such as sesquiterpenes, has proved particularly challenging due to extensive fragmentation in traditional proton transfer reactions, thus complicating the interpretation of ambient mass spectra (6). In parallel, separation techniques (e.g., gas chromatography) have been utilized to eliminate isobaric interferences at both nominal and fragment masses, but their low temporal resolution limits their utility for certain applications such as eddy covariance. In what follows, we extend the early work of Leibrock and Huey (2000) (9) to explore the utility of benzene cations, $(C_6H_6)_n^+$, for the selective detection of various SOA precursors *via* chemical ionization mass spectrometry (CIMS), in the marine boundary layer.

The early work of Leibrock and Huey (9, 10) demonstrated the potential for benzene cations for the CIMS detection of isoprene and monoterpenes among a series of other conjugated dienes and aromatics. Leibrock and Huey (9) showed that VOC with ionization energies lower than that for benzene (ca. 9.24 eV) react at or near the collision limit either *via* direct charge transfer (R1) forming the charge transfer product X^+ or through a ligand switching reaction involving the benzene dimer cation (R2) forming the ion-neutral product $X^+(C_6H_6)$.

$$(C_6H_6)_n^+ + X \rightarrow (C_6H_6)_n + X^+ \qquad \text{R1}$$

$$(C_6H_6)_n^+ + X \rightarrow X^+(C_6H_6) + (C_6H_6)_{n-1} \qquad \text{R2}$$

It follows that benzene ion chemistry should be a sensitive measurement for a host of molecules beyond those demonstrated in Leibrock and Huey, including DMS (IE = 8.69 eV) and sesquiterpenes (IE = 9.54 eV) and their first generation oxidation products (Lias, NIST Webbook). Further, due to the high density of states of C_6H_6 and $(C_6H_6)_2$, collisional energy from the ion-molecule reaction can be readily absorbed, permitting the efficient formation of weakly bound ion-neutral clusters and the potential for very soft ionization of large BVOCs such as bicyclic sesquiterpenes.

It is critical to note that, like in many positive ion CIMS techniques, extensive dehydration of alcohols can complicate the interpretation of mass spectra. Specifically, Leibrock and Huey showed that the dehydration of 2-methyl-3-buten-2-ol (MBO), could lead to a positive artifact in the detection of isoprene, despite the fact that the IE for MBO exceeds 9.25 eV. Further, benzene ion chemistry is not exceedingly selective as compared with other ion-molecule chemistries, as such the potential for interferences is high, particularly in polluted air-masses.

Here, we describe laboratory characterization experiments and field observations in the remote marine boundary layer designed to assess the utility to benzene cations for the selective detection of SOA precursors. Laboratory experiments were conducted using both a chemical-ionization time-of-flight mass spectrometer (CI-ToFMS) (11) and a chemical ionization quadrupole mass spectrometer (CI-QMS) to probe ion-molecule reaction mechanisms and adduct stability under different electric field strengths. Field measurements from the remote North Atlantic boundary layer were validated against simultaneous measurements of DMS mixing ratios made

by an atmospheric pressure ionization mass spectrometer with an isotopically labelled standard (APIMS-ILS) (12).

2. Experimental

2.1 Instrument Descriptions

The utility of benzene reagent ion chemistry for the sensitive, selective detection of DMS, isoprene, and monoterpenes was characterized on two CIMS instruments: 1) a field deployable chemical ionization time-of-flight mass spectrometer (CI-ToFMS) (11) optimized for the sensitive detection of trace gases from mobile platforms and 2) a laboratory based chemical ionization quadrupole mass spectrometer (CI-QMS), operated without declustering optics or RF-only ion guides, achieving low field electric strengths at the cost of sensitivity. Despite different ion transmission optics and mass analyzers, the two instruments utilize identical ion-molecule reaction chambers.

2.1.1 Chemical Ionization Time of Flight Mass Spectrometer (CI-ToFMS)

A complete description on the CI-ToFMS hardware can be found in Bertram et al., 2011. Briefly, reagent ions, generated by passing trace neutral precursor gases carried in ultra-high purity (UHP) N_2 over an α-emitting polonium source (Section 2.1.3) are mixed with ambient air in an ion-molecule reaction (IMR) chamber (P_{IMR} = 70 mbar). Reaction times are estimated to be on the order of 100 ms, significantly longer than the time scale for ion-molecule reactions to reach equilibrium. Product ions pass through four additional differentially pumped stages, beginning with the

collisional dissociation chamber (P_{CDC} = 2 mbar), housing an RF-only quadrupole ion guide. In the CDC, ion-molecule adducts can be dissociated by adjusting the electric field strength or pressure of the chamber. After passing through the second RF-only quadrupole ion guide housed at 1.4e-2 mbar and a fourth chamber that contains the final focusing optics that condition the ion beam for entry into the extraction region of the ToF mass analyzer, where ions are orthogonally extracted into a compact time-of-flight mass spectrometer (Tofwerk AG and Aerodyne Research Inc.). Typical extraction frequencies range between 30-85 kHz, resulting in mass spectra spanning between 11 - 319 m/Q. Individual mass spectra are averaged and saved at 10 Hz following the procedures outlined in Bertram et al., 2011.

2.1.2 Chemical Ionization Quadrupole Mass Spectrometer (CI-QMS)

The CI-QMS used in these studies employs the same ion molecule reaction chamber described in Bertram et al (2011), but operated at lower pressure (P_{IMR} = 50 mbar). In contrast to the CI-ToFMS, the CI-QMS was operated to minimize the declustering of weakly bound ion-neutral clusters prior to detection. The CI-QMS was operated with only three stages of differential pumping and with a series of lenses in place of the RF ion guide devices. The resulting instrument achieves minimal collisional declustering, at the expense of sensitivity. Ions were mass selected using a quadrupole mass selector (Extrel Inc.). Transmitted ions were detected using a continuous dynode and electron multiplier, where single ion events were converted to TTL pulses for measurement and analysis *via* custom LabView software. The CI-QMS was operated in parallel with the CI-ToFMS to provide insights into the ion

cluster distributions at the point of reaction, as the stronger electric fields and subsequent dissociation of ion-neutral clusters in the CI-ToFMS limit our ability to elucidate ion chemistry occurring in the IMR.

2.2 Reagent Ion Generation and Chemistry

On both platforms, the reagent ion precursor benzene gas was generated by diluting a certified compressed gas standard (50 ppm ± 0.1 ppm in N_2, Praxair) with UHP N_2 generated from LN2 boil off. The total reagent flow rate is limited by an inline critical orifice (1.8 slpm) which also serves the dual purpose of keeping permeable Teflon gas delivery lines at positive pressure relative to the atmosphere to prevent diffusion of contaminants into the ion delivery lines. Downstream of the orifice, reagent gas flow is passed through an α-emitting polonium-210 source (NRD 2021-1000 at 10mCi initial activity). N_2^+ ions are formed *via* electron transfer reactions with α-particles (Eq. 1) and go on to ionize neutral benzene (13) to form a distribution of benzene cations $(C_6H_6)_n^+$ (R3-4).

$$N_2 + \alpha^{2+} \rightarrow {N_2}^+ + \alpha^+ \qquad \text{R3}$$

$$C_6H_6 + {N_2}^+ \rightarrow (C_6H_6)^+ + N_2 \qquad \text{R4}$$

$$C_6H_6 + (C_6H_6)^+ \rightarrow {(C_6H_6)_n}^+ \qquad \text{R5}$$

3. Laboratory Characterization

3.1 Factors Controlling Primary Ion Distributions

During laboratory experiments, the CI-QMS and CI-ToFMS ion generation systems were identical, with the exception of the IMR pressure. As shown in Fig. 1.1,

the benzene ion distribution as measured by CI-QMS was detected predominantly in the form of $(C_6H_6)_2^+$ at 156 m/Q (Fig. 1.1A). The same distribution was detected by CI-ToFMS in the form of $C_6H_6^+$ at 78 m/Q (Fig. 1.1B). This suggests that the reagent ion distribution primarily exists as $(C_6H_6)_2^+$ in the CI-ToFMS IMR as well, but the field strength of the RF-only quadrupole ion guide in the CDC of the CI-ToFMS exceeds the benzene dimer binding energy of 2-3 kcal/mol (14).

Baseline mass spectra were examined by overflowing the sample inlet with UHP zero air while varying the benzene concentration of the reagent ion flow. On the CI-ToFMS, the benzene monomer accounted for 68 to 91% of the total ion current (Fig. 1.2) for benzene precursor ion concentrations ranging between 1-45 ppm, where $(C_6H_6)_2^+$:$(C_6H_6)^+$ was 2.34e2:1.38e6 at 10 ppm C_6H_6. For both instruments, the main benzene ion peak plateaued at ca.10 ppm (Fig. 1.3). Trace amounts of $(C_6H_6)_2^+$ continued to increase with benzene concentration on the CI-ToFMS (Fig. 1.3B). Although the zero air cylinders were assumed to be nominally dry, trace amounts of water (detected as protonated water clusters), were evident in the sample stream at low benzene concentrations. On the CI-QMS, the weaker monomer ion signal was less than 0.03% of the dimer signal with the $(C_6H_6)_2^+$:$(C_6H_6)^+$ ratio at 1.9e1:6.5e4 at 10 ppm C_6H_6 (Fig. 1.3).

Baseline tests revealed persistent background peaks at 92, 106 and 120 mQ, which collectively accounted for 1-3% of total ion current. As discussed in Section 4.5, during field measurements, the sum of these three peaks comprised an average of 2.6% (1σ = 0.8%) of the total ion current. These background peaks were observed across all CIMS instruments, and their strength increased with benzene concentration

(Fig. 1.2) suggesting they are trace contaminants in the benzene cylinders. We tentatively attribute these peaks to toluene, ethylbenzene, xylene (collectively BTEX) or trimethylbenzene. Background peak strength appeared to decrease very slightly with ambient humidity in laboratory testing (Fig. 1.3), likely due to the titration of ion potential by water molecules.

Instrument baselines were examined as a function of humidity to probe the impact of ambient water vapor on product ion distributions. Reagent ion precursor benzene concentration was held constant at 10 ppm while humid UHP zero air (0-100% relative humidity, room temperature) overflowed the inlet. On the CI-ToFMS, benzene monomers remained >86% of the total ion current (Fig. 1.4A) at 100% relative humidity. Benzene monomer count rates showed minimal sensitivity to ambient water vapor (Fig. 1.3B). Protonated water clusters ($H\text{-}(H_2O)_n^+$) were observed upon the addition of water vapor to sample air. The sum of the ion current for $H\text{-}(H_2O)_n^+$ (n = 1-4) ranged from 0.7-8.5% of the total ion current, increasing with relative humidity. Again, trace amounts of water vapor were detected while sampling nominally dry UHP zero air (Praxair) due to a small amount of condensation in zero air cylinders.

Because the ionization energy of benzene (9.2 eV, NIST Webbook) is less than water (12.6 eV, NIST Webbook), it is unlikely that a benzene mediated pathway for the formation of protonated water clusters is active. Additionally, benzene-water clusters are not observed, suggesting that protonated water clusters are formed by direct ionization (15) due to diffusion of ambient water into the ionizer, or persistent N_2^+ may contribute to direct ionization of water in the IMR. This parallel pathway

accounts for benzene's minimal dependence on ambient humidity. Following this logic, molecular oxygen ions (O_2^+, 12.0 eV) should be and are observed in trace amounts (<1.3% of the total ion current).

3.2 Calibration

Calibration curves were generated using three parallel CIMS systems (CI-ToFMS, CI-QMS, and CIMS that employs a residual gas analyzer for ion selection and quantification, CI-RGA) to determine the sensitivity of benzene reagent ion chemistry to previously identified and novel VOC species: dimethyl sulfide, isoprene, and α-pinene. Results from the first two instruments are included here. Instrument responses to atmospherically relevant mixing ratios (0 to 3.2 ppb) of dimethyl sulfide-d3 (0.1841 ppm ± 10%), isoprene (0.500 ppm ± 10%) and α-pinene (0.497 ppm ± 10%) were measured for specific humidities (Q) from 0 to 16.6 g/kg. VOC standards were supplied from authenticated cylinders (AirGas) and diluted with ultra-high purity (UHP) zero air (Praxair). A separate humidified flow was generated by flowing UHP zero air through three sequential frit bubblers (Ace Glass) containing deionized water. Flow rates for all VOC standards, dry and saturated dilution flows were set with a valved mass flow meter or a mass flow controller (±10%). A mass closure calculation was performed on water levels during portions of the experiments to ensure the bubbled zero air reached saturation. Bubbler temperatures were recorded for specific humidity calculations accounting for cooling at very high flow rates due to gas expansion. All CIMS instruments were positioned around a central manifold (0.25" OD PFA tubing and ¼" PFA Swagelok fittings) sampling from its own radial branch.

Each inlet line was the same length to within 2". Excess flow was directed from the central manifold line to an exhaust system at atmospheric pressure. Humidified air was added furthest downstream to minimize the surface area exposed to significant water vapor levels.

As shown in Fig. 1.6, benzene dimer cations were demonstrated to be sensitive to DMS, as well as isoprene and α-pinene as shown previously by Leibrock and Huey, 2000. Normalized sensitivities were calculated by referencing product ion count rates to a reagent ion reference signal of 10^6 CPS (16). Calibration constants are reported as the slope of the linear fit of each curve (1σ = slope standard deviation). Thus, absolute sensitivity increases with benzene ion current. Maximum normalized sensitivities were as follows: DMS (23.5 nCPS/ppt), α-pinene (41 nCPS/ppt), and isoprene (8.3 ncPS/ppt). All three VOCs calibration factors exhibited unique humidity dependences described in more detail in Section 3.3.

3.3 Adduct Declustering

VOC product ions corresponded to the nominal mass (M^+) or a benzene cluster ($M\text{-}(C_6H_6)^+$). Product ions are thought to proceed through direct charge transfer by the benzene cluster (Reaction 3) or a ligand switching reaction (Reaction 4). However, product clusters in the latter mechanism may dissociate after formation in the IMR before detection by the mass analyser.

$$M + (C_6H_6)_2{}^+ \rightarrow M^+ + (C_6H_6)_2 \qquad (3)$$

$$M(C_6H_6)_2{}^+ \rightarrow M - (C_6H_6)^+ + C_6H_6 \qquad (4)$$

Isoprene was detected as a benzene adduct (146 mQ), while α-pinene appeared at nominal mass (136 mQ) on both the CI-QMS (Fig. 1.1A) and CI-ToFMS (Fig. 1.1B). DMS was detected at M^+ on the CI-ToFMS and as an M-$C_6H_6^+$ cluster on the CI-QMS, while using a dimethyl sulfide-d3 calibration standard. This suggested that DMS ionization proceeds through a ligand-switching reaction (Eq. 4), with the adduct dissociating in the CI-ToFMS. Despite attempts to minimize the field strength of the CI-ToFMS, we were not able to observe the DMS-benzene cluster.

Instrument response to pure, yet unknown mixing ratios of a host of other VOCs, including a sesquiterpene and a monoterpenoid, were assessed with the CI-ToFMS. In these experiments a small volume (1 mL) of pure ß-caryophyllene and 1,8 cineole standards were deposited into clean flasks and delivered to the CI-ToFMS inlet. Product ions were identified and normalized to the sum of all feasible products. As described previously, DMS and α-pinene product ions are dominated by M^+, while isoprene is detected as a benzene adduct (Fig. 1.6). ß-caryophyllene was detected at nominal mass (204 m/Q) with very limited fragmentation. Since ß-caryophyllene has been demonstrated to fragment more readily that other sesquiterpenes (Kim et al., 2009), these tests suggest that benzene dimer cations show excellent promise as an accurate chemical ionization method ion to target easily fragmented terpene species. 1,8 cineole, or 1,3,3-Trimethyl-2-oxabicyclo[2,2,2]octane, an oxygenated monoterpenoid ($C_{10}H_{18}O$) was also detected largely at its nominal mass of 154 m/Q. However, due to its proton affinity (17), a secondary ionization reaction with protonated water clusters was evident at the M-H^+ channel (see Section 2.2). After

accounting for contributions from the carbon-13 isotope, we estimate the ratio of charge transfer to proton transfer product ions are about 2:1.

3.4 Factors Affecting Sensitivity and Selectivity

Benzene dimer cations demonstrated high sensitivity to DMS, α-pinene, and isoprene standards with peak sensitivities occurring at the noted specific humidities: 23 nCPS/pptv (6.7 g/kg), 41 nCPS/pptv (11.7 g/kg), and 8.3 nCPS/pptv (11.7 g/kg) respectively (Fig. 1.4). Calibration constants varied with ambient specific humidity on all CIMS platforms. On the CI-ToFMS, DMS was observed to be least sensitive to changes in ambient water vapor, while α-pinene sensitivity increased almost linearly with humidity for Q values between 0 and 12 g/kg. This suggests that ambient water impacted ion-molecule reactions in a variety of different ways, as suggested by other reagent-ion techniques (18, 19).

Benzene dimer cations have been shown previously to react at the collision limit with conjugated dienes and aromatics with ionization energy below 9.25 eV. Given this criteria, the potential interferences to the described VOCs are few. As shown previously, 2-methyl-3-butene-2-ol (MBO, 164 m/Q) was also observed in our experiments to dehydrate after ionization and interfere with isoprene at 146 mQ. Leibrock and Huey (9) also found benzene dimer cations to be sensitive to trans-l,3-pentadiene at 146 mQ. In what follows we assess the performance metrics for the CI-ToFMS using benzene ion chemistry during ship based field experiments in the remote marine boundary layer, where contamination from anthropogenic sources is of lesser importance.

4. In-field Performance

The CI-ToFMS utilizing benzene reagent ion chemistry was deployed to the Arctic and North Atlantic aboard the R/V *Knorr* during the fall of 2013 for over 2.5 months to measure VOCs concentrations and turbulent fluxes in remote marine boundary layer. Here, we use measurements from the five week High Wind Gas Exchange Study (HiWinGS) to investigate factors controlling reagent ion stability and sensitivity to VOCs in challenging environmental conditions. Isoprene, α-pinene, and UHP zero air gas cylinders were used to determine in-field sensitivities and baselines, respectively. We validate our dimethyl sulfide measurement against DMS mixing ratios provided by the University of Hawaii's atmospheric pressure ionization mass spectrometer with an isotopically-labelled standard (APIMS-ILS).

4.1 Inlet Characterizations

A low-pressure (200 mbar), rapid response, high Reynolds number (Re ~ 2400) inlet assembly was designed based on the inlet manifold described in Ellis et al (2010) and adapted for measurement of VOC mixing ratios and air-sea exchange from research vessels. The complete inlet assembly included separate lines for sample, bypass, baseline and calibration flows sheathed together by a durable weatherproof exterior (80' total length, 60' weatherproofed x ~2-3" OD, Clayborn Labs). All inlet lines were connected to a glass manifold based of the design of Ellis et al., (2010) (20). Inlet flow rates are set by a critical orifice (~1.2 mm ID, 12.56 slpm) housed within the 1" OD cylindrical glass body. Downstream of the orifice (low pressure

side), sample flow is split into a bypass (~2.5 slpm) and sample (10.0 slpm) stream. The bypass branch is in-line with the manifold intake. Upstream manifold surfaces were treated with Fluoropel (Cytonix). The sample flow follows a series of 90° and 180° turns, which serve to eliminate super-micrometer sea spray particles from the sample inlet stream. The manifold was housed in an insulated weather-proofed housing and mounted off the foremast. The sample intake was ca. 20 meters above mean sea level (amsl) and ca. 17 meters aft of the bow (21). The entire inlet sample line and manifold assembly was heated by a single PID heating circuit (Omega) set to 40^{o} C.

The inlet assembly containing the sample (3/8" OD FEP), bypass (¼" OD PFA), baseline (3/8" OD FEP) and calibration (1/8" OD FEP) lines ran between the manifold and a temperature controlled instrument van on the 02 deck housing the CI-ToFMS. Baseline and calibration gas flows were controlled by mass flow controllers on an automated LabView program. Ambient air was directed from the sample line to the front block of the CI-ToFMS, a chamber upstream of the IMR held at the inlet pressure (200 mbar). The CI-ToFMS subsampled from the front block stream, while the rest of the flow rejoined the bypass flow downstream of the instrument. Choked flow conditions in the manifold-sample-bypass-front block assembly were maintained by a 500 lpm scroll pump (Varian TriScroll 600). Front block pressures were recorded by a pirani pressure gauge. UHP zero air and VOC standards were added to the inlet manifold *via* separate ports located upstream of the critical orifice (i.e. high pressure side) to account fully for surface loss to the manifold and inlet surfaces. Instrument baselines were determined by overflowing the critical orifice with 20 slpm of UHP

zero air from a gas tank (Praxair). VOC sensitivity was assessed with several daily standard additions and calibrations. The first several weeks of the research cruise utilized isoprene standards before switching to α-Pinene during the last two weeks (both 0.500 ppm in N_2, Praxair).

4.1.1 Time Response

Ambient VOC signal decays from zero air additions were examined to characterize inlet time response. Fitting a double exponential curve to signal decays yields two characteristic time constants for the inlet (20). The first exponential decay time, τ_1, is attributed the gas evacuation time and related to the physical operation and characteristics of the inlet itself. The second exponential decay time, τ_2, is attributed to the equilibration constant of the gas itself and related to its polarity and solubility. For the n=3 protonated water cluster, DMS, and α-pinene, τ_1 of 2 s agreed well with the volumetric evacuation time of 3.6 seconds at 12.53 slpm . The second characteristic time, τ_2, was long for the protonated water cluster at 22 s, as expected based on the polarity and high surface affinity of water vapor. In contrast, DMS and α-pinene exhibited fast τ_2 time constants at 0.43 s, indicating good turbulent flow and minimal frequency attenuation. Curve fitting to explicitly examine spectral characteristics will be examined in a forthcoming manuscript on VOC air-sea exchange.

4.2 Benzene Stability

Benzene reagent ion signal strength varied between 58 – 89% of the total ion current during HiWinGS. A probability density function of benzene counts during

ambient and baseline periods showed a bimodal distribution but no difference between these sampling periods (Fig. 1.8). This was consistent for standard addition and calibration periods as well. Abrupt step-changes in the benzene ion signal were evident over the course of the research cruise. These shifts also corresponded to nearly equal increases in protonated water cluster peaks (0.7 to 39% total ion current). These abrupt shifts occur independently of ambient specific humidity or other environmental variables. We suspect these shifts are driven by trace levels of condensation in the benzene standard cylinders. Based on the previously described laboratory tests (Section 2.2), benzene remains > 86% and protonated water clusters peaked at 8.5% of total ion current at 100% relative humidity (Fig 1.4A). At typical room temperatures (20-24^{o}C), 100% relative humidity is equivalent to specific humidities between 14.6-18.8 g/kg). Minute average specific humidity during HiWinGS peaked at 13.2 g/kg, which suggests the abrupt increases in protonated water cluster signal (and corresponding decreases in benzene) are driven by water vapor in the reagent ion generation source, rather than ambient humidity. A less probable explanation for the increase in pronated water cluster signals may be attributed to diffusion of water into the permeable gas delivery lines that spanned over 100’ from the gas cylinder rack on the main deck to the instrument van on the 02 deck. Despite being sheathed, the lines were undoubtedly exposed to sea spray and condensation during Force 11 seas. However, this would not explain the step-function changes in benzene and water signal.

4.3 VOC Sensitivity

Absolute sensitivity to VOC standard additions varied with the fluctuating benzene reagent ion current and ambient water vapor. Calibration factors were calculated from raw count rates during each VOC additions after subtracting ambient contributions calculated from interpolating values from bracketed sampling periods. Without an active calibration source, hourly DMS absolute calibration factors were calculated dividing average baseline-adjusted counts by concurrent APIMS-ILS determined mixing ratios (CPS ppt^{-1}). The DMS calibration method is described further in Section 4.4. Mean absolute sensitivities were 19.4, 2.8 and 6.1 CPS ppt^{-1} for DMS, isoprene and α-pinene, respectively.

Background count rates are computed from the mean of raw count rates (1 Hz) measured during valid instrument zero periods throughout the entire campaign as in Kercher et al., 2009 (22). Variability in baseline counts are largely driven by fluctuations in the benzene reagent ion current. Detection limits are calculated as in Bertram et al., 2010 (11) as 3-standard deviations of a Gaussian fit for all baseline count rates over the entire campaign. Because we do not have a measure of the humidity of the zero air used for baselines, detection limits are reported in units of nCPS. Detection limits were 152, 13 and 42 nCPS for DMS, isoprene and α-pinene, respectively (Table 1).

After normalizing to the benzene ion current, the humidity dependence of in-field VOC normalized calibration factors (Fig. 1.9) is consistent with laboratory tests (Fig. 1.4). However, the values of normalized calibration factors were lower by a factor of 4-7 for each VOC molecule. This shift in sensitivity value is highlighted for α-pinene in Fig. 1.10. Possible explanations include VOC standard degradation, inlet

performance (less probable for nonpolar terpenes) or most likely due to shifts in sensitivity from tuning instrument voltages between the two experiments.

4.4 Validation

Baseline adjusted, reagent-ion normalized count rates at 62 m/Q were compared to dimethyl sulfide mixing ratio measurements provided by the University of Hawaii's atmospheric pressure ionization mass spectrometer with isotopically labelled standard (APIMS-ILS). Both instruments were housed in separate, neighboring instrument vans on the Knorr. The CI-ToFMS sample manifold was mounted to the foremast as described in Section 4.1. Alternatively, the APIMS-ILS inlet was mounted to the meteorological mast located at the bow of the ship and ca. 16.3 meters amsl. This is about 17 meters fore and 4 meters below the CI-ToFMS intake position.

Baseline adjusted, normalized count rates were calculated by subtracting interpolated baseline values from ambient 62 m/Q counts and scaling to a benzene ion current of 10^6 CPS (16) (Fig. 1.6). No adjustments based on ambient humidity were made. A regression analysis between the normalized CI-ToFMS signal and APIMS-ILS DMS mixing ratio measurements showed excellent agreement (R^2 = 0.80) over extreme wind speeds, low ambient loadings, and temperatures below freezing (Fig. 1.11). As suggested by laboratory tests, a slight water vapor dependence is evident at specific humidity higher than 10 g/kg but the calibration factor is largely constant over most humidities (Fig. 1.12). The good agreement, despite the disparate sampling

locations, suggests that flow distortion around the ship structure during HiWinGS was minimal.

5. Summary and Future Directions

Benzene dimer cations have been revisited as a chemical ionization method for the detection of volatile organic compounds. DMS and β-caryophyllene were identified as novel VOC targets and product ions exhibited limited fragmentation (<9% β-caryophyllene). Sensitivity to DMS, isoprene, and α-pinene were determined on a CI-ToFMS in laboratory experiments and in-field standard additions with a focus on humidity dependencies for performance in the remote marine boundary layer. Laboratory-based VOC calibration factors ranged between 2 and 41 nCPS, with varying water vapor dependencies. These trends were well conserved between laboratory and field measurements, but normalized sensitivity values were lower in the field by a factor of 4 to 7. Minor background peaks attributed to alkyl-substituted benzene were traced to contamination in the benzene source. Water vapor in the benzene cylinder standards were also found to degrade benzene reagent ion signal significantly. Future directions will explore drier, cleaner benzene sources such as reagent grade liquid benzene and nitrogen from liquid nitrogen boil-off.

6. Acknowledgements

Thanks to the entire High Wind Gas Exchange Study science team and Matt Zoerb for assistance in field installation. A special thanks to the WHOI Marine

Operations staff, Captain Kent Sheasley and the capable crew of the RV Knorr for their dedication that led to the success of this work.

Chapter 1, in full, is currently being prepared for submission for publication of the material. Kim, M.J., Zoerb, M.C., Campbell, N.R., Zimmermann, K.J., Blomquist, B., Huebert, B., and T.H. Bertram. The dissertation author was the primary investigator and author of this paper.

Figures

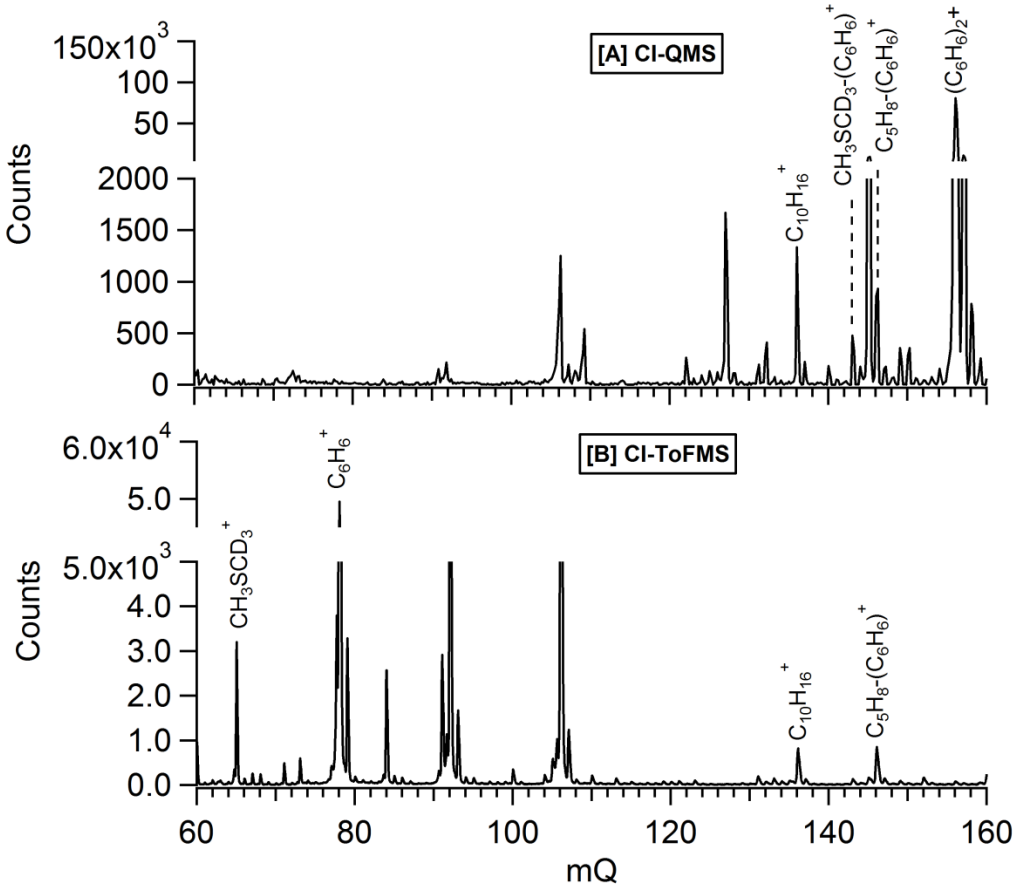

Figure 1.1 Mass spectra generated by the CI-QMS (A) and the CI-ToFMS (B) utilizing benzene dimer cations sampling a mixture of dimethyl sulfide-d3 (methane-d3,(methylthio)), isoprene and α-pinene in 40% relative humidity at room tempeature. The weaker field strength of the CI-QMS transmits clustered forms of benzene ($(C_6H_6)_2^+$) and dimethyl sulfide-d3 (CH_3SCD_3-$C_6H_6^+$). Both are detected at nominal mass by the CI-ToFMS. Isoprene was detected as a benzene cluster (C_5H_8-$C_6H_6^+$) and α-pinene ($C_{10}H_{16}^+$) appeared at nominal mass on both instruments.

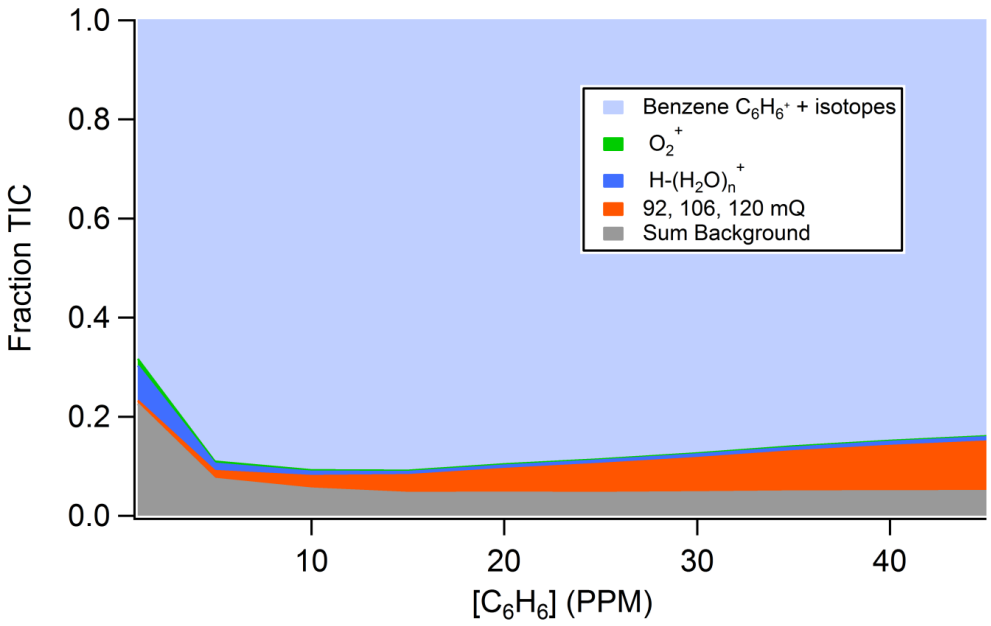

Figure 1.2 Shifts in CI-ToFMS baseline peak distributions (as TIC fraction) as a function of reagent concentration [C_6H_6].
Neutral benzene concentrations ranged from 1 to 45 ppm. Baseline spectra were generated by sampling nominally dry UHP zero air (Praxair), though trace amounts of water vapor were evident. Peaks at 92, 106 and 120 mQ comprised a large fraction of the instrument background signal. This fraction increased with benzene mixing ratio suggesting they are contaminants in the benzene source. The peaks are attributed to alkyl-substituted benzene molecules: C_6H_5-CH_3^+ at 92 mQ, C_6H_4-$(CH_3)_2^+$ at 106 mQ, and C_6H_4-$(CH_3)_3^+$ at 120 mQ.

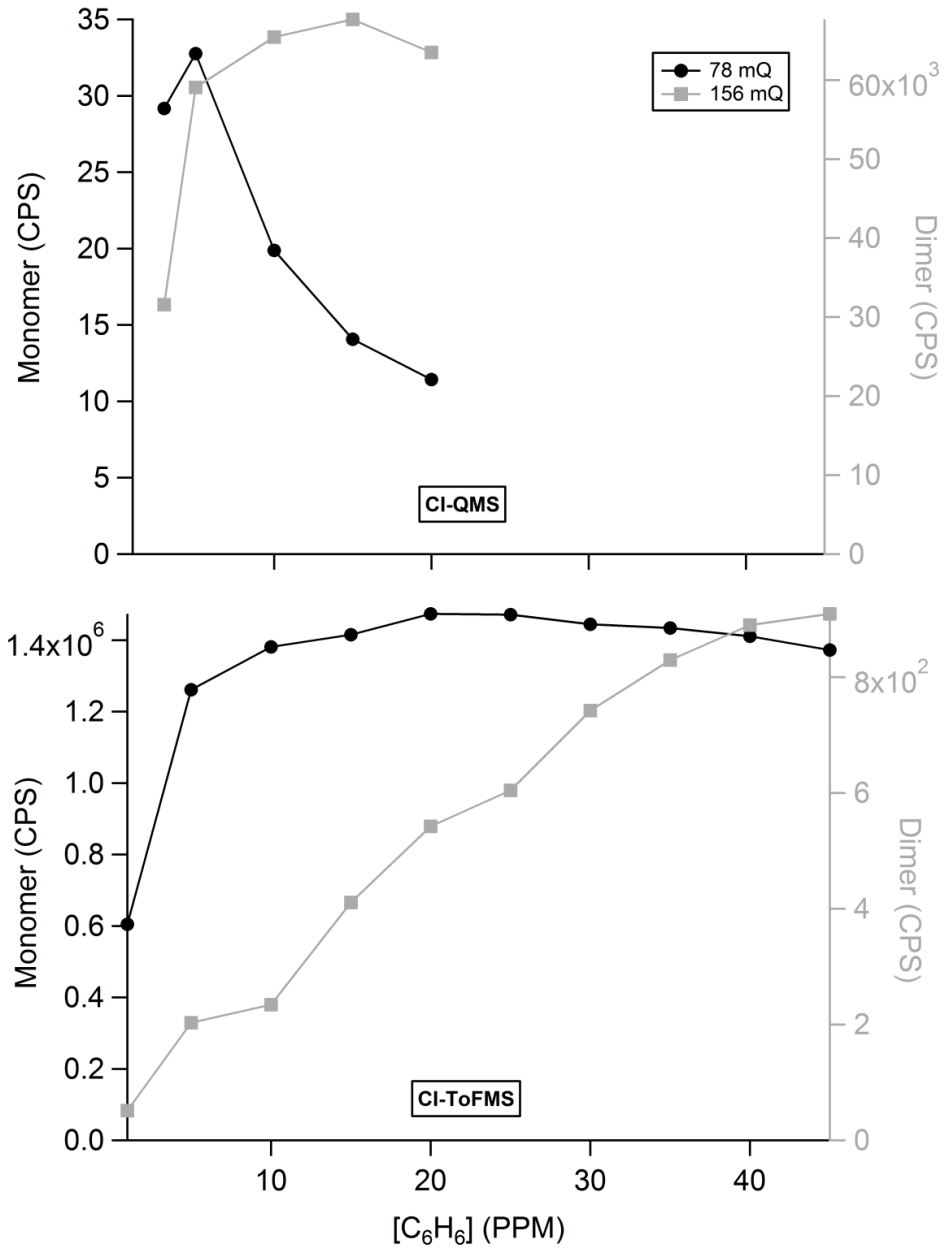

Figure 1.3 Benzene ion currents as a function of [C_6H_6]. Nearly all CI-QMS benzene ion current was in dimer form (156 mQ) while the CI-ToFMS featured monomers (78 mQ). Both dominant benzene peaks plateaued after 10 ppm neutral benzene. Minor peaks comprised < 0.1% of major peak.

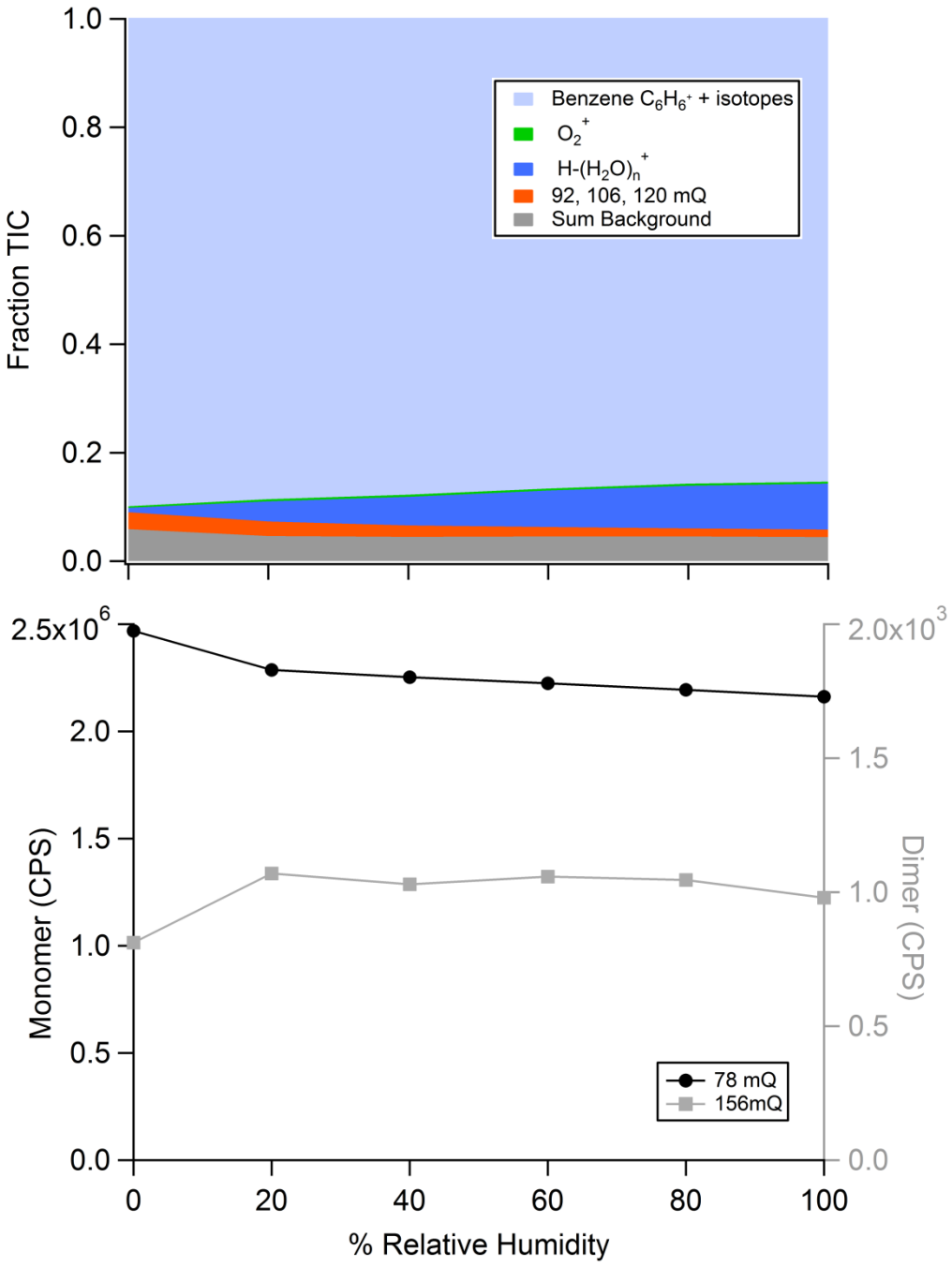

Figure 1.4 CI-ToFMS baselines were examined as a function of ambient relative humidity ([C_6H_6] = 10 ppm).
(Top) CI-ToFMS baseline peak distributions (% TIC) varied as a function of relative humidity and remained above 85% of total ion current. Experiments demonstrated that ambient water vapor drives the formation of protonated water clusters. (Bottom) Raw benzene count rates are not significantly impacted by ambient relative humidity.

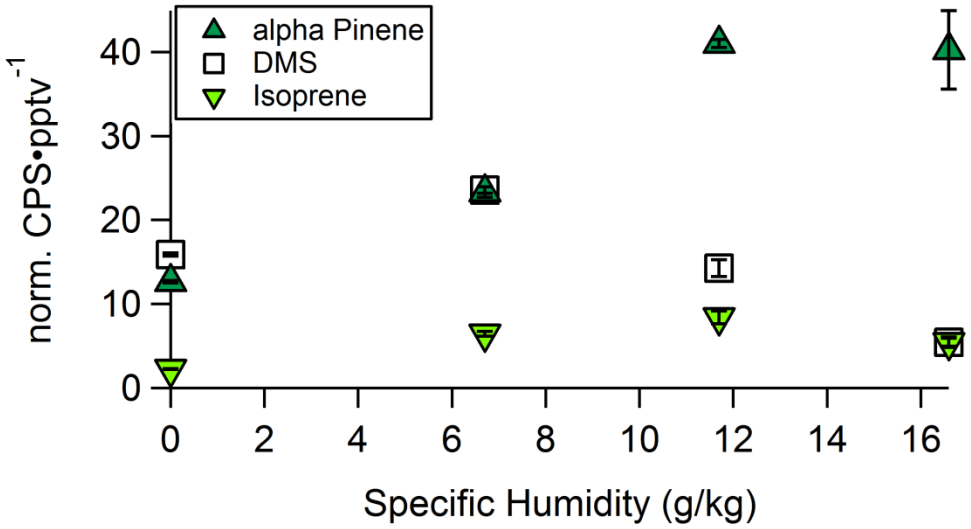

Figure 1.5 Laboratory calibration experiments yielded benzene dimer cation sensitivity to select volatile organic compounds. Dimethyl sulfide, α-pinene, and isoprene calibration constants (normalized counts per second/ppt) varied with ambient humidity. Error bars correspond to 1σ error of the calibration curve slope.

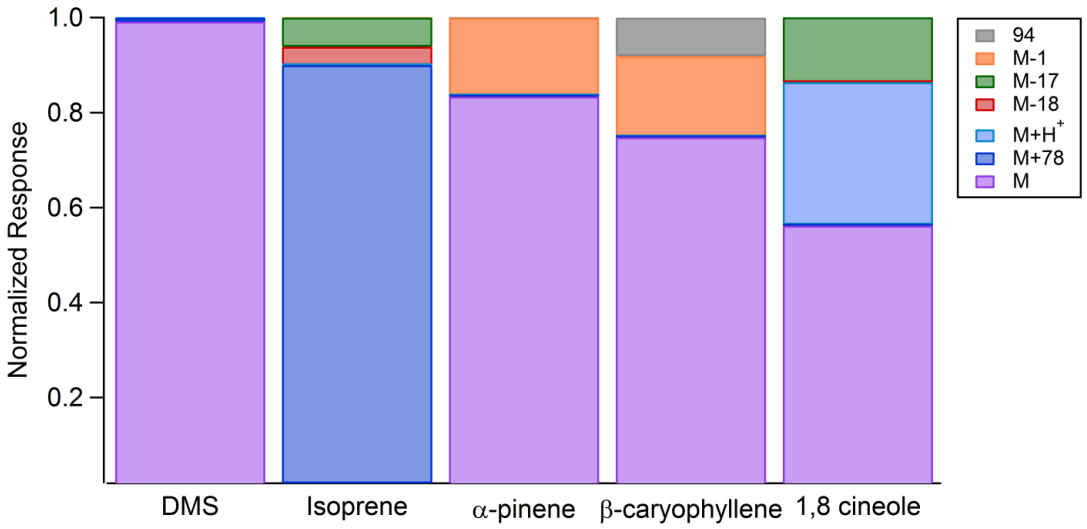

Figure 1.6 Qualitative trace amounts of VOC standards were wafted in front of the CI-ToFMS in ambient air to examine product ion distributions. Product ions were identified visually from time traces and flagged if it was > 5% of the total response. Expected contributions from carbon-13 isotopes were accounted for in calculated proton transfer products. For 1,8 cineole, the ratio of charge transfer to proton transfer products were roughly 2:1.

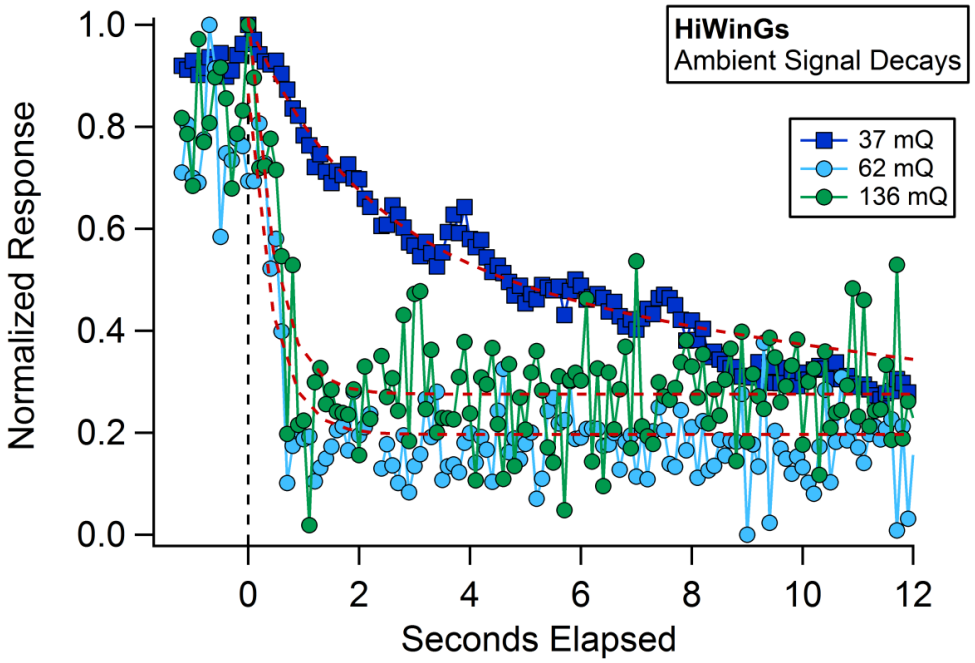

Figure 1.7 In-field responsiveness of a custom low-pressure, high Reynolds number inlet was assessed by fitting a bi-exponential curve to signal baseline decays. The first decay is attributed to the gas evacuation time (τ_1) and the second decay is attributed to wall-equilibration times (τ_2).

τ_1 for 37, 62, and 136 mQ (attributed to the protonated water dimer, DMS and monoterpenes respectively) were 2.0 ,0.7 and 0.44 seconds, which agreed with the volumetric evacuation time of the sample inlet (3.6 seconds). τ_2 values were 22, 0.43, and 0.43 seconds respectively

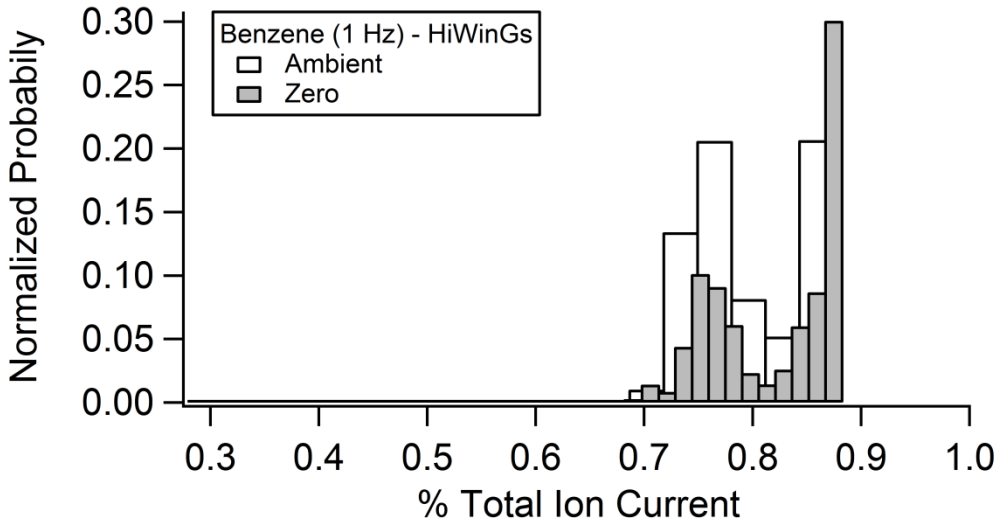

Figure 1.8 Probability density function of benzene signal (% TIC, 1 Hz) during ambient and baseline sampling periods.
Distributions did not differ between ambient and baseline sampling. Bimodal distributions corresponded to shifts in ion current from benzene to protonated water clusters (sum n = 1-4) due to switches in benzene tanks rather than ambient specific humidity, indicating the bimodal distribution is driven by trace water vapor contamination in the reagent ion source.

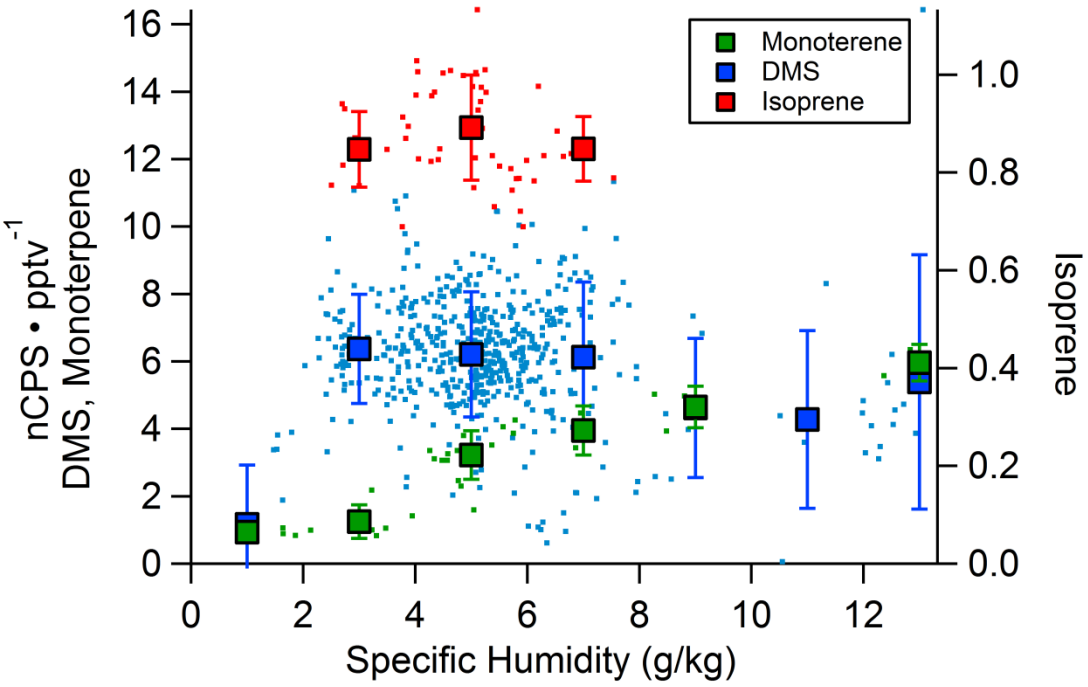

Figure 1.9 In-field sensitivities calculated from standard additions (or comparison between to APIMS-ILS mixing ratios) as a function of ambient humidity. Dots are calibration factors from standard additions and squares are binned values for a 2 g/kg specific humidity range.
Each VOC shows a very similarly shaped humidity dependence as were demonstrated by laboratory tests, but normalized calibration factors differ by a factor of 4 to 7 by species.

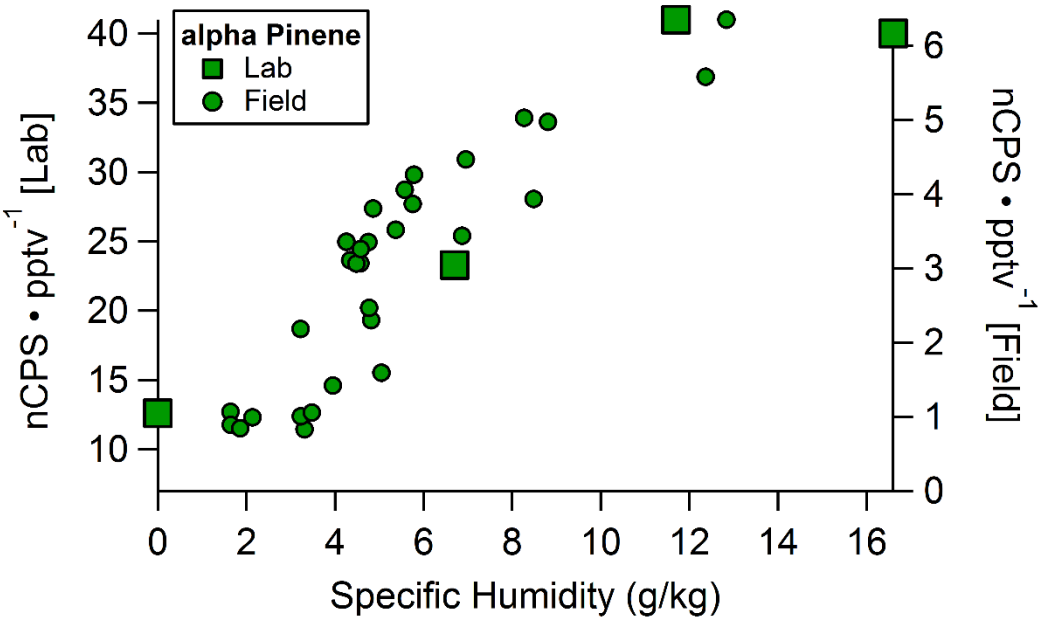

Figure 1.10 Comparison of α-pinene normalized calibration factors observed during laboratory (left axis) and in-field standard additions (right axis) show similar attenuation with specific humidity. In-field values are lower by a factor of 7 suggesting a shift in instrument performance outside of ion generation.
Possible factors include different voltage settings, degraded calibration standards or losses to the exposed glass surfaces of the sample manifold.

Table 1.1 Summary of in-field CI-ToFMS performance on the HiWinGS research cruise for select volatile organic compounds. Isoprene and a-pinene were calibrated against in-field standards. DMS figures of merit utilized simultaneous, independent DMS mixing ratios from the University of Hawaii's APIMS-ILS.

VOC	**Sensitivity (CPS/pptv,** 1σ**)**	**Background (Hz,** 1σ**)**	**Detection Limit (nCPS, 3σ)**
Dimethyl sulfide	19.4 ± 10.5	495 ± 320	152 nCPS
Isoprene	2.8 ± 0.9	13 ± 49	13 nCPS
α-pinene	6.1 ± 3.4	115 ± 86	42 nCPS

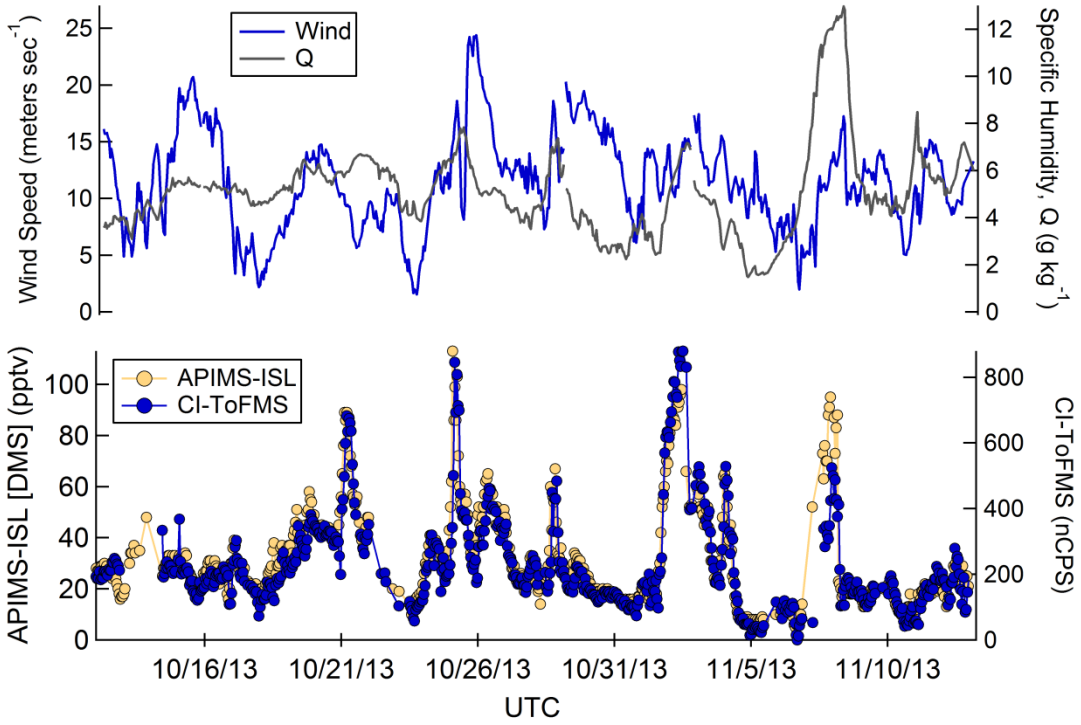

Figure 1.11 Hourly wind, specific humidity and DMS measurements from the High Wind Gas Exchange Study (HiWinGS). Winds peaked around 25 meters per second. DMS mixing ratios were low (< 137 pptv) indicating low biological activity. Due to a lack of an active DMS standard, no humidity corrections were made.

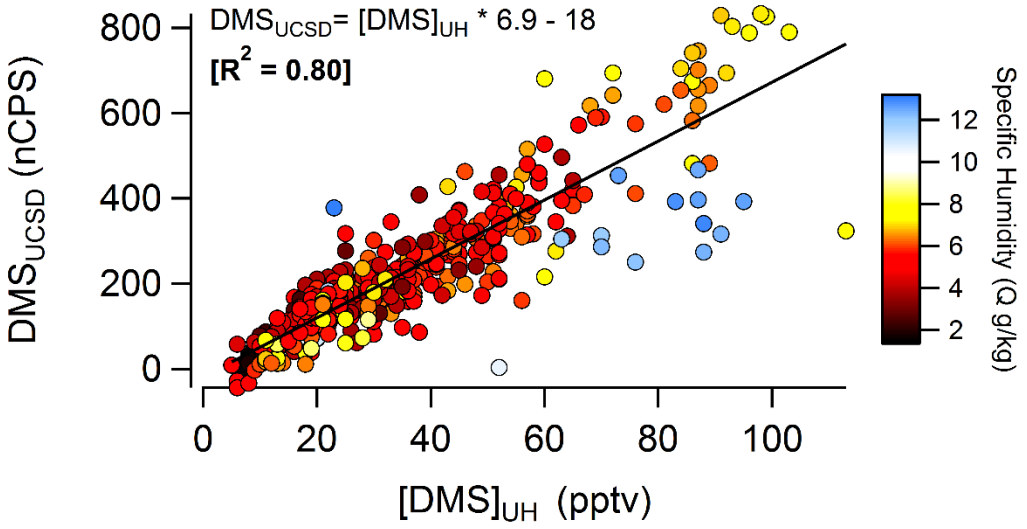

Figure 1.12 Regression of background- and benzene-normalized DMS counts indicate excellent agreement (0.80 R^2 value) to DMS mixing ratios observed by APIMS-ISL. A campaign average CI-ToFMS sensitivity of 6.9 nCPS/pptv is estimated. A slight sensitivity attenuation at Q > 10 g/kg, was observed and confirmed in laboratory tests.

References

1. Goldstein A, Galbally I (2007) Known and unexplored organic constituents in the earth's atmosphere. *Environ Sci Technol*.

2. Arnold SR, et al. (2009) Evaluation of the global oceanic isoprene source and its impacts on marine organic carbon aerosol. *Atmos Chem Phys* 9(4):1253–1262.

3. Jaoui M, et al. (2006) Analysis of secondary organic aerosol compounds from the photooxidation of d-limonene in the presence of NOx and their detection in ambient PM2.5. *Environ Sci Technol* 40(12):3819–3828.

4. Guenther AB, et al. (2012) The model of emissions of gases and aerosols from nature version 2.1 (MEGAN2.1): An extended and updated framework for modeling biogenic emissions. *Geosci Model Dev* 5(6):1471–1492.

5. Kanakidou M, et al. (2005) Organic aerosol and global climate modelling: a review. *Atmos Chem Phys* 5(4):1053–1123.

6. Kim S, et al. (2009) Measurement of atmospheric sesquiterpenes by proton transfer reaction-mass spectrometry (PTR-MS). *Atmos Meas Tech* 2(1):99–112.

7. Myriokefalitakis S, et al. (2010) Global Modeling of the Oceanic Source of Organic Aerosols. *Adv Meteorol* 2010:1–16.

8. Huey LG (2007) MEASUREMENT OF TRACE ATMOSPHERIC SPECIES BY CHEMICAL IONIZATION MASS SPECTROMETRY : SPECIATION OF REACTIVE NITROGEN AND FUTURE DIRECTIONS. *Mass Spectrom Rev* 26(2):166– 184.

9. Leibrock E, Gregory L (2000) Ion Chemistry for the Detection of Isoprene and other Volatile Organic Compounds in ambient Air of (STP)) • - Pinene Air or dry nitrogen mixture of benzene were. 27(12):1719–1722.

10. Leibrock E, et al. (2003) Ground-based intercomparison of two isoprene measurement techniques. *Atmos Chem Phys* 3:67–72.

11. Bertram TH, et al. (2011) A field-deployable, chemical ionization time-of-flight mass spectrometer. *Atmos Meas Tech* 4(7):1471–1479.

12. Blomquist BW, Huebert BJ, Fairall CW, Faloona IC (2010) Determining the sea-air flux of dimethylsulfide by eddy correlation using mass spectrometry. *Atmos Meas Tech* 3(1):1–20.

13. Sinnokrot MO, Valeev EF, Sherrill CD (2002) Estimates of the ab initio limit for pi-pi interactions: The benzene dimer. *J Am Chem Soc* 124:10887–10893.

15. Good A, Durden DA, Kebarle P (1970) Mechanism and Rate Constants of Ion–Molecule Reactions Leading to Formation of H+(H2O)n in Moist Oxygen and Air. *J Chem Phys* 52(1):222.

16. Warneke C, van der Veen C, Luxembourg S, de Gouw J., Kok a (2001) Measurements of benzene and toluene in ambient air using proton-transfer-reaction mass spectrometry: calibration, humidity dependence, and field intercomparison. *Int J Mass Spectrom* 207(3):167–182.

17. Maleknia SD, Bell TL, Adams MA (2007) PTR-MS analysis of reference and plant-emitted volatile organic compounds. *Int J Mass Spectrom* 262(3):203–210.

18. Lee BH, et al. (2014) An iodide-adduct high-resolution time-of-flight chemical-ionization mass spectrometer: application to atmospheric inorganic and organic compounds. *Environ Sci Technol* 48(11):6309–17.

19. Crounse JD, McKinney KA, Kwan AJ, Wennberg PO (2006) Measurement of Gas-Phase Hydroperoxides by Chemical Ionization Mass Spectrometry. *Anal Chem* 78(19):6726–6732.

20. Ellis R a., et al. (2010) Characterizing a Quantum Cascade Tunable Infrared Laser Differential Absorption Spectrometer (QC-TILDAS) for measurements of atmospheric ammonia. *Atmos Meas Tech* 3(2):397–406.

21. Yang M, Blomquist BW, Nightingale PD (2014) Air-sea exchange of methanol and acetone during HiWinGS: Estimation of air phase, water phase gas transfer velocities. *J Geophys Res Ocean* 119(10):7308–7323.

22. Kercher JP, Riedel TP, Thornton JA (2009) Chlorine activation by N 2 O 5 : simultaneous , in situ detection of ClNO 2 and N 2 O 5 by chemical ionization mass spectrometry. (2):193–204.

Chapter 2

Direct Observations of Biogenic Volatile Organic Compound (BVOC) Air-Sea Exchange in the North Atlantic from the High Wind Gas Exchange Study (HiWinGS)

Biogenic volatile organic compound air-sea exchange was measured via eddy covariance over the remote North Atlantic Ocean as part of the High Wind Gas Exchange Study. Monoterpenes, isoprene and dimethyl sulfide mixing ratios and fluxes were measured with a field-deployable chemical ionization time-of-flight mass spectrometer utilizing benzene dimer cation reagent ion chemistry. A custom designed low-pressure, high Reynolds number (Re ~ 2300) inlet was utilized for eddy covariance measurements of trace volatile organic compounds. Dimethyl sulfide air-sea exchange measurements showed good agreement (R^2 = 0.77) with the University of Hawaii's atmospheric pressure ionization mass spectrometer. Monoterpenes fluxes were observed to be positive (i.e. emitted) over remote locations as well as in coastal productive waters. Isoprene remained around the detection limit in remote regions and peaked around 50 pptv in coastal regions.

1. Introduction

Biogenic volatile organic compounds (BVOC) are naturally derived, non-methane organic gases. Due to their high reactivity, they play significant roles in global atmospheric chemistry and climate. The majority of global BVOC emissions are driven by isoprenoid compounds such as isoprene (C_5H_8) and monoterpenes (MT, $C_{10}H_{16}$). Recent model estimates place the global annual isoprene burden around 500 Tg yr^{-1} (~50% total BVOC) while MT emission rates are lower at 162 Tg yr^{-1} (15% total BVOC), with the vast majority emitted from continental regions (1). Another abundant BVOC, dimethyl sulfide (DMS, $(CH_3)_2S$) is the largest biogenic source of reduced sulfur to the atmosphere (2) with well-documented impacts on marine atmospheric chemistry and cloud condensation nuclei distributions (3, 4). Estimates of DMS contributions to sulfate aerosol mass range between 18 – 24% (5, 6)

While marine DMS fluxes comprise between 80 to 99% of global emissions, marine isoprene sources are estimated to contribute between 0.2 to 3.1% of global emissions (7). However, due to their high reactivity and aerosol yields, marine isoprenoids have been suggested to play an important role in marine aerosol (8) and cloud albedo (9, 10). Isoprene and monoterpene oxidation products have also been found in submicron aerosol particle samples collected from pristine marine air masses (11, 12)

Marine phytoplankton have been demonstrated to produce BVOCs in seawater in several laboratory experiments where both DMS, isoprenoids and organohalides have been detected in monoculture headspace sampling experiments and seawater analysis (13–16). BVOC production rates have been shown to be related to

phytoplankton species (17), seawater temperature (18), nutrients (19), chlorophyll-α concentrations (20, 21) and photosynthetically active radiation (22) with temperature and light driving enhancements to BVOC production, similar to terrestrial production mechanisms (23).

Isoprenoids may perform an anti-oxidant role with production demonstrating enhancement during temperature and oxidative stress (7, 15, 24). Studies of the various biochemical origins of isoprene implicate several important production mechanisms. In studies of terrestrial plants, isoprene is enzymatically synthesized by the action of isoprene synthase (IspS) on 1-deoxy-D-xylulose-5-phosphate (DMADP) (25) formed from the methylerythiritol 4-phosphate (MEP) pathway. This pathway is common to most bacteria, photosynthetic eukaryotes and the plastids of plant cells (26).

From these laboratory-derived parameterizations of BVOC production rates, physically-based global models of BVOC air-sea exchange have provided initial estimates of marine BVOC as well as their impacts on marine SOA production rates. Gantt et al. (27) suggested that isoprene may contribute as much as 30% of submicron aerosol organic mass fraction on a monthly basis during periods of high biological activity in the tropics, and possibly up to 50% on an hourly basis during midday. However, due to an extreme paucity of observations on air-sea exchange rates of isoprene and no observations of monoterpenes, estimates span several orders of magnitude. Isoprene emission rates range between 0.1 Tg C yr^{-1} (bottom up) and 11.6 Tg C yr^{-1} (top-down) (27–30). Estimates of global marine α-pinene emissions range between 0.013 Tg C yr^{-1} and 29.5 Tg C yr^{-1} (30).

In-situ constraints of ambient atmospheric BVOC beyond DMS are rare, particularly in the remote marine boundary layer where potential interferences from strong continental sources of BVOC would be minimized. A ship-based study by Yasaa et al. (14) report evidence of the marine monoterpene mixing ratios between 100-200 pptv while sampling ambient air downwind of an active phytoplankton bloom in the remote South Atlantic Ocean. A few indirect measurements of isoprene flux have been documented. Baker et al. (31) measured isoprene flux rates between about 1 - 4 nmol $m^{-2}hr^{-1}$ in the Eastern Atlantic Ocean during May. To our knowledge, no observations of monoterpene air-sea exchange have been reported in the literature. This work represents the first direct (i.e. eddy covariance) observations of BVOC air-sea exchange.

2. Methods

2.1. The High Wind Gas Exchange Study

The High Wind Gas Exchange Study research cruise (University of Hawaii, NOAA/ESRL) took place over five weeks during fall of 2013 in the North Atlantic (Figure 2.1). The main cruise objective was to improve air-sea exchange parameterizations in high wind regimes (> 10 m s^{-1}). A secondary objective was to target regions of enhanced biological activity that would sustain steep air-sea gradients of biogenically driven trace gases (i.e. carbon dioxide, DMS, isoprenoids). Trace gas air-sea exchange of a suite of molecules, gas transfer velocities, as well as sea state and environmental forcing parameters were characterized.

2.2. BVOC Sampling

Isoprene, monoterpenes and DMS mixing ratios and fluxes were measured with a field-deployable chemical-ionization time-of-flight mass spectrometer (CI-ToFMS) utilizing benzene dimer cation reagent ions (32). The sampling configuration and hardware utilized for mixing ratios has been described in detail in Kim et al. (*in prep.*). Here, we review details related to the flux measurement. Air-sea exchange rate were calculated directly using the eddy covariance method (33–35). Full mass spectra were recorded at 5 Hz. Three-dimensional winds were logged by a sonic anemometer (Wind Master, Gill) and ship motions were captured by an inertial motion unit (Motion Pak II, Systron Donner) both at 10 Hz (36). Both the sonic and IMU were mounted on a "diving board" platform extending from the foremast of the ship. The BVOC sample inlet was mounted on a sidearm off the diving board located about 0.5 meters to the starboard side of the wind-motion package.

A custom sampling inlet was designed for the detection of BVOC air-sea exchange. Two design criteria were considered. First, a high Reynolds number was targeted to limit frequency attenuation of high frequencies in the scalar signal. Second, measures were taken to limit BVOC line losses due to anticipated low atmospheric abundances and high humidity conditions. To this end, line pressures were dropped to 200 mbar to increase volumetric flow rates (liters min^{-1}), which also limited condensation. The line was also heated to 40 degrees Celsius which reduces the Reynolds number slightly, but its prevention of condensation outweighed this small effect on the flow characteristics. The sample line diameter reflected a compromise between narrower widths, which favor turbulent flow and reduce surface area, and a

wider line that would reduce the pressure drop (285 mbar) between the instrument and the intake point. Pressures at the instrument were recorded by a pirani guage at 200 mbar. With the calculated pressure drop, we estimate that the pressure in the sampling manifold on the foremast was approximately 485 mbar which is well below the maximum pressure required to maintain choked flow conditions in the inlet manifold (535 mbar) to maintain the maximum flow rate (12.85 slpm) as well as turbulent flow conditions.

Baselines counts due to instrument noise and inlet-wall off-gassing were recorded every 2 hours by overflowing the inlet manifold with ultra-high purity zero air (UHP, AirGas). This pulse of zero air and resulting ambient signal decay also served the additional purpose of estimating inlet response times and frequency attenuation (37). BVOC calibrations standards were added to the inlet both as standard additions (every 6 hours) and single-point calibrations (every 6 hours, staggered). Standard additions provided in-field constraints on the humidity dependent calibration factors. An isoprene standard was utilized during the month of October and an α-pinene standard was used during November through the end of the cruise (both in N_2, 0.500 ppm; AirGas).

2.3 Data Processing

2.3.1 Mixing Ratios

BVOC mixing ratios were calculated by subtracting interpolated baseline values, then dividing by a calibration factor. Calibration factors were calculated differently for each BVOC target based on an in-field constraints. Isoprene and

monoterpenes calculations utilized active calibration sources, while DMS sensitivities were determined against simultaneous observations from the APIMS-ISL. To avoid potential interferences, only one calibration standard was used at a time. DMS mixing ratios are presented without adjustments for humidity.

In October, isoprene calibration factors were calculated from standard additions and linearly interpolated across ambient sampling periods. Normalized calibration factors were stable over the three weeks (mean 0.92 nCPS $pptv^{-1}$; 1σ = 0.18) of standard additions. Due to this stability, the mean value was applied to portions of the campaign following the active calibration period. Monoterpene normalized calibration factors were based on an α-pinene calibration gas over the month of November. Sensitivities during standard additions demonstrated a linear dependence (R^2 = 0.77) on ambient specific humidity. This relationship was reproduced in laboratory testing. Applying a linear fit between normalized sensitivity and specific humidity (hereafter "Qfit, Fig. 2.3), calibration factors were estimated for the entire campaign. In this manner, a humidity-dependent calibration factor (normalized counts $pptv^{-1}$) was estimated and constrained by in-field standard additions.

A campaign-average normalized calibration factor was calculated for DMS from the linear regression of CI-ToFMS baseline-adjusted normalized counts (62 m/Q) against DMS mixing ratios ($pptv^{-1}$) measured by the APIMS-ILS (38). Lacking a direct calibration standard, no humidity correction was applied to the CI-ToFMS mixing ratio calculations or subsequent flux calculations. CI-ToFMS DMS sensitivity did, however, demonstrate a small humidity dependence during Q > 10 g/kg. This

small humidity dependence was also demonstrated in laboratory tests (Kim et al., 2015, *in prep*).

2.3.2 Eddy Covariance Calculations

Air-sea exchange rates were calculated via the eddy covariance method. Flux is calculated as the average covariance of vertical wind (w') and BVOC mixing ratios (x') over a defined flux interval (E1).

$$F = < w'x' > = k * (C_w - C_a * H) \qquad \text{(E1)}$$

Vertical winds and scalars were corrected for ship motion artifacts according to Edson et al. (1998). Wind and motion data were recorded by a separate computer from BVOC mixing ratios, resulting in a lag times (seconds) between the two data streams. Following Bariteau et al. (37), lag times were determined as the time shift resulting in the maximum covariance between the adjusted wind and BVOC mixing ratio data. This time lag represents the sum of the different in the two system CPU timestamps as well as the time offset due to the transit time of ambient air in the inlet sample tube.

Calculated flux rates underwent quality control measures to meet eddy covariance assumptions of stationarity and homogeneity (39). Corrections for density fluctuations due to water vapor surface exchange (40) are ignored for this work due to the short lifetimes of the BVOC species in this study. When concentration fluctuations, c', are comprise the majority of the mean value, errors due to density fluctuations are likely to be insignificant (35).

3. Results

The RV Knorr departed from Nuuk, Greenland on 9 October, 2013 and arrived at Woods Hole, MA on 14 November 2013 (Figure 2.1). Seven total sampling stations were distinguished by passing storms and related sustained periods of high winds (Figure 2.2). Overall, 66% of hourly mean wind speeds exceed 10 m/s, 26% exceeded 15 m/s and 5% exceeded 20 m/s. Biological activity as indicated by chlorophyll-α over the open ocean, ranging between 1.1 and 2.4 mg/L as measured by the Knorr underway system (values taken only after flushing the intake line between Stations 1 and 2 for biofouling). Due to potential planktonic growth in the line, this data represents the maximum potential chlorophyll-α levels.

3.1 BVOC Mixing Ratios

DMS mixing ratios were relatively low throughout HiWinGS (maximum 137 pptv) (Figure 2.4) (3σ detection limit = 22 ppt or 152 nCPS). Hourly averaged CI-ToFMS agreed well with APIMS-ISL DMS measurements (R^2 = 0.80) (Kim et al., 2015, *in prep*). Monoterpenes hourly average mixing ratios were elevated in remote regions peaking around 70 pptv. Mixing ratios returned to baseline (campaign wide 3σ LOD = 42 nCPS), then reached campaign-wide maximum values around 250-300 pptv in more biologically productive coastal regions near Newfoundland. Isoprene mixing ratios (hourly) remained near the detection limit (3σ LOD = 13 nCPS) in remote regions, but peaked during the coastal sampling station (Station 7) around 50 pptv in the Straight of Belle Isle near Newfoundland (Figure 2.4).

3.2 BVOC Fluxes

Observed monoterpene air-sea exchange rates were positive indicating emission from the surface ocean. Exchange rates ranged between 0 and 0.8 ppt m sec^{-1}, comparable to DMS emission rates in coastal productive waters (Figure 2.5). CI-ToFMS measured DMS air-sea exchange agreed well with the University of Hawaii's eddy covariance measurements (Figure 2.6) with an $R^2 = 0.68$ (Figure 2.7), despite sampling from two spatially disparate positions on the ship.

Simultaneous measurements of DMS and sensible heat flux offered a novel opportunity to examine the impact of sampling location on eddy covariance flux measurements. Sensible heat fluxes computed by the PML WindMaster on the foremast and University of Hawaii's sonic anemometer on the meteorological mast agreed well (36) while CI-ToFMS DMS exchange from the foremast typically underestimated APIMS-ILS values made from the meteorological mast on the bow of the ship. Because the CI-ToFMS mixing ratios were calculated using APIMS-ILS mixing ratios as a proxy calibration standard, this underestimation cannot be related to physical losses of DMS sample in the inlet, but rather frequency attenuation or flow distortion.

Due to the agreement in sensible heat fluxes, the most likely explanation for this discrepancy is frequency attenuation leading to flux signal loss at high frequencies. Spectral similarity plots comparing sensible heat and DMS flux show there is some high frequency attenuation above 0.2 to 0.3 Hz (Figure 2.8). Given that 1/5 of the total sample line flow rate set by the glass manifold critical orifice was directed to a bypass line, the Reynolds number in the sample line itself is about 2245

putting this in the transition regime between laminar and turbulent flow. Applying the parameterization of Lenshow and Raupach (41), the estimated half-power frequency would be at 1.21 Hz, which is typical of frequencies driving turbulent exchange in the surface layer (42). A discrepancy between parameterized and in-field measured half-power frequencies by a factor of 10 is not uncommon i.e. (43), in which case, this estimate agrees with typical half-power frequencies observed throughout the campaign.

Generally, flow distortion is not found to be an issue for the majority of the cruise given the agreement in sensible heat flux calculations between the two sonic anemometers at the respective DMS sampling positions (36). A comparison of the sensible heat fluxes calculated from each sampling position showed excellent agreement except when the incoming wind was from -90 degrees (0 degrees indicating the bow of the ship, -90 port side). These flux periods have been removed from the comparison during quality control.

4. Discussion and Conclusions

Ship-based eddy covariance measurements of biogenic volatile organic compound air-sea exchange and atmospheric mixing ratios were performed for the first time on the High Wind Gas Exchange Study. Equilibrium seawater concentrations were calculated for monoterpenes from eddy covariance flux measurements and atmospheric mixing ratios using Equation 1. Gas transfer velocities were approximated with cubic a wind-speed dependent parameterization based on Wanninkhof 1999 (44). A Schmidt number parameterization based on sea-surface

temperature used previously in the literature for isoprene air-sea exchange models (29) is applied here. Calculated equilibrium seawater concentrations range from 0 to 17 picomolar (Figure 2.5), which are on-scale with previous observations of dissolved isoprenoid seawater concentrations (16).

DMS flux measurements by the CI-ToFMS were in good agreement with the APIMS-ILS, but some high frequency attenuation due to cross-axial diffusion in the sample line was evident. Future deployments can address this issue by increasing the size of the critical orifice in the sample manifold. To our knowledge, this work represents the first measurement of monoterpene air-sea exchange. Net flux was positive (0 to 4.1 ppt meters/sec) during periods of sampling in both remote (< 1.5 μg/L chlorophyll-α) and productive coastal regions (>1.5 μg/L chlorophyll-α), at times rivaling DMS emission rates.

5. Acknowledgements

The authors would like to thank the entire HiWinGS scientific team. Special thanks to WHOI Marine Operations, Captain Kent Sheasley and the crew of the RV Knorr for their dedication to the success of this campaign.

Chapter 2, in full, is currently being prepared for submission for publication of the material. Kim, M. J., Yang, M., Blomquist, B., Huebert, B., and T.H. Bertram. The dissertation author was the primary investigator and author of this paper.

Figures

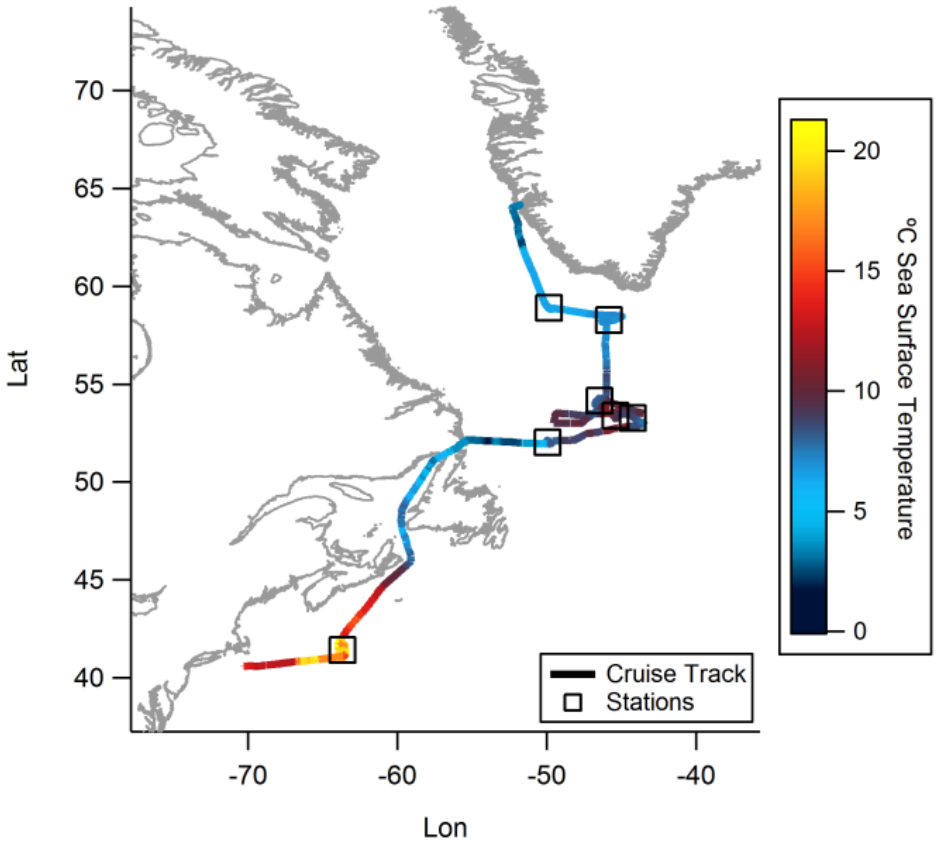

Figure 2.1 The cruise track of the RV Knorr during the High Wind Gas Exchange Study in the North Atlantic. The Knorr disembarked from Nuuk, Greenland on October 9 and arrived in Woods Hole, MA on November 14, 2013. Station locations were chosen based forecasted high-winds.

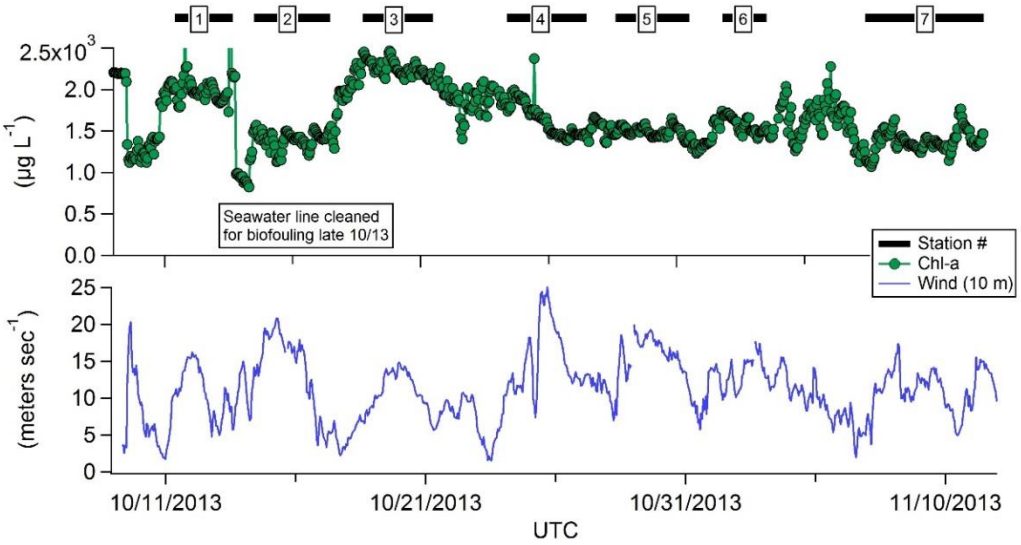

Figure 2.2 Environmental conditions measured during HiWinGs sampling stations (1-7) including chlorophyll-α measured from the Knorr underway system (intake 5 meters below sea level) and 10 meter wind speeds (latter provided by NOAA/ESRL). Chlorophyll-α represent maximum values due to inline growth, as evidenced by the step change between Station 1 and 2 due flushing the underway seawater system.

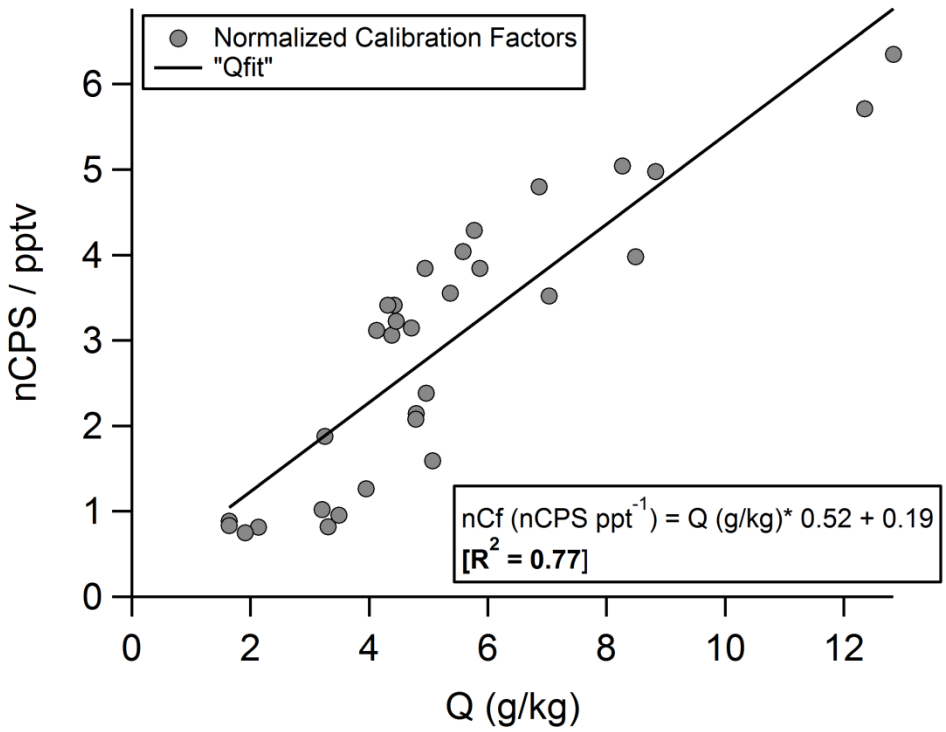

Figure 2.3 Normalized calibration factors from α-pinene standard additions demonstrated a linear dependence on ambient specific humidity, Q. A humidity dependent calibration factor ("Qfit") was calculated from the slope of the regression and applied to all monoterpene mixing ratio calculation on HiWinGS.

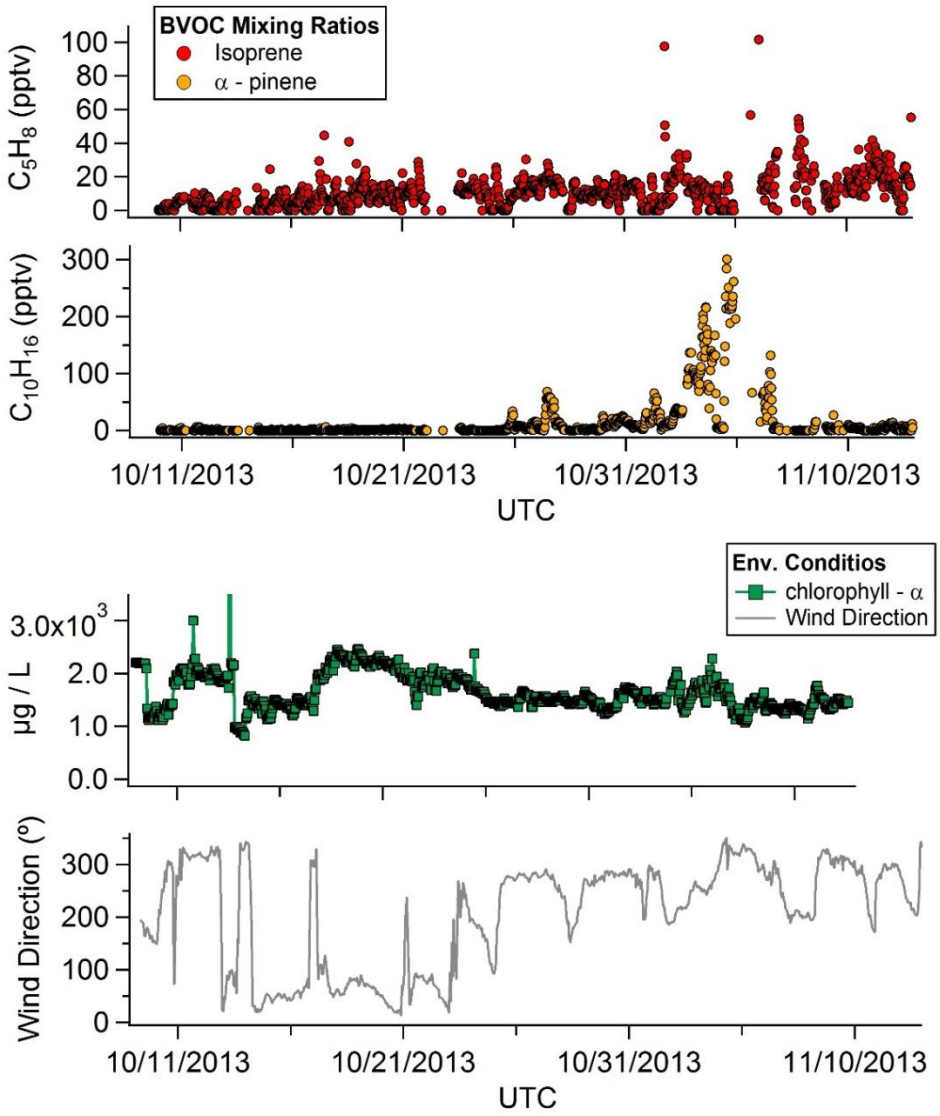

Figure 2.4 Observed BVOC mixing ratios during the High Wind Gas Exchange Study including isoprene and monoterpenes (top). Monoterpene mixing ratios peaked in late October and early November during a large storm in the remote MBL (~70 pptv) and then again elevated concentrations near the coast (between 250 and 300 pptv). Chlorophyll-α levels were slightly elevated in coastal waters.

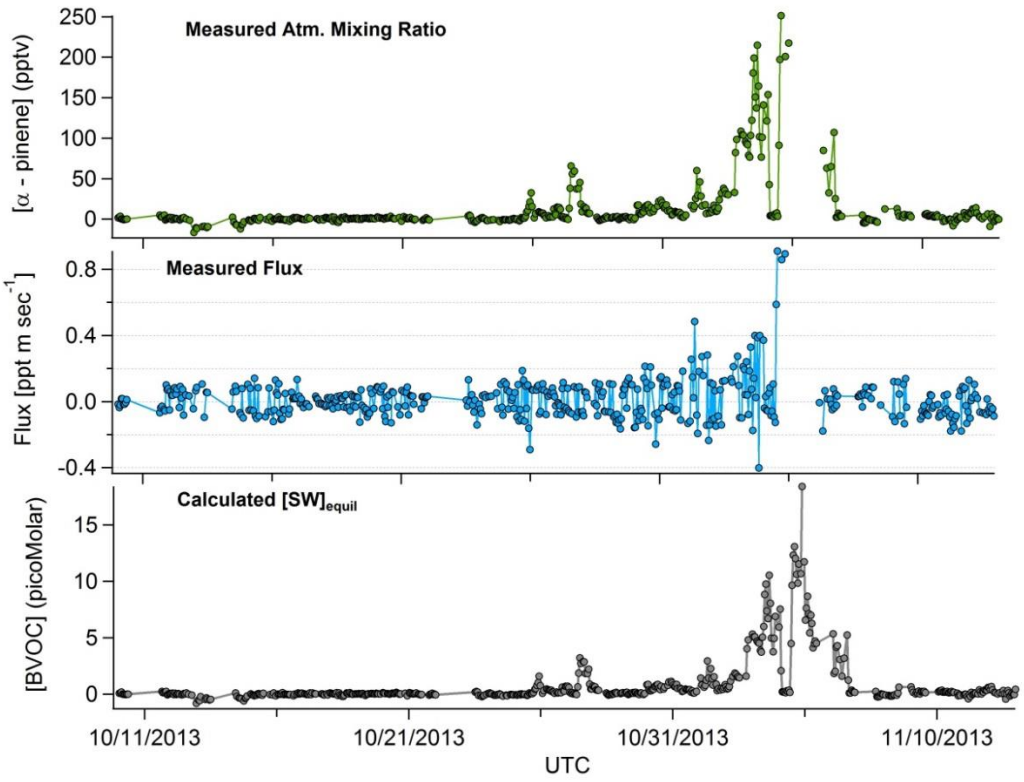

Figure 2.5 Observed hourly monoterpene mixing ratios and air-sea exchange rates calculated *via* eddy covariance. Monoterpene emissions were observed at rates similar to or exceeded dimethyl sulfide at various points throughout the cruise near the coast. Equilibrium seawater concentrations were calculated using Equation 1, as described in Section 4.

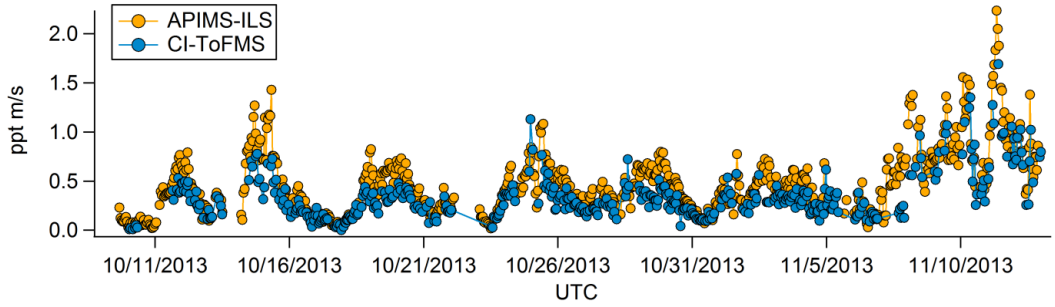

Figure 2.6 A comparison of DMS air-sea exchange observations demonstrates good agreement between CI-ToFMS and APIMS-ILS eddy covariance measurements indicating little flow distortion between the foremast and meteorological mast on the bow.

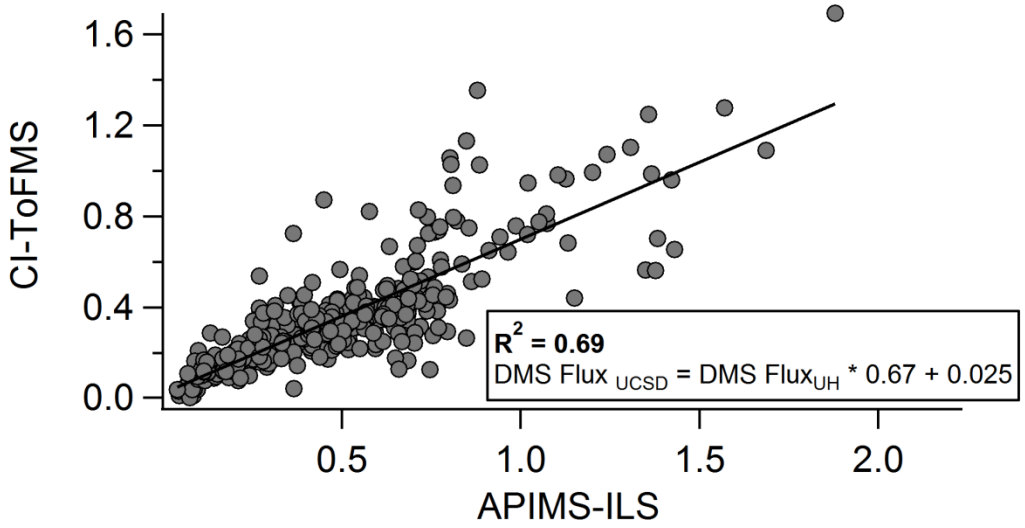

Figure 2.7 A regression analysis of CI-ToFMS measured emission rates with APIMS-ILS shows that the CI-ToFMS underpredicts DMS exchange. This may be due to a number of factors including high frequency attenuation in the sampling line or flow distortion due to the disparate sampling locations of the two measurements.

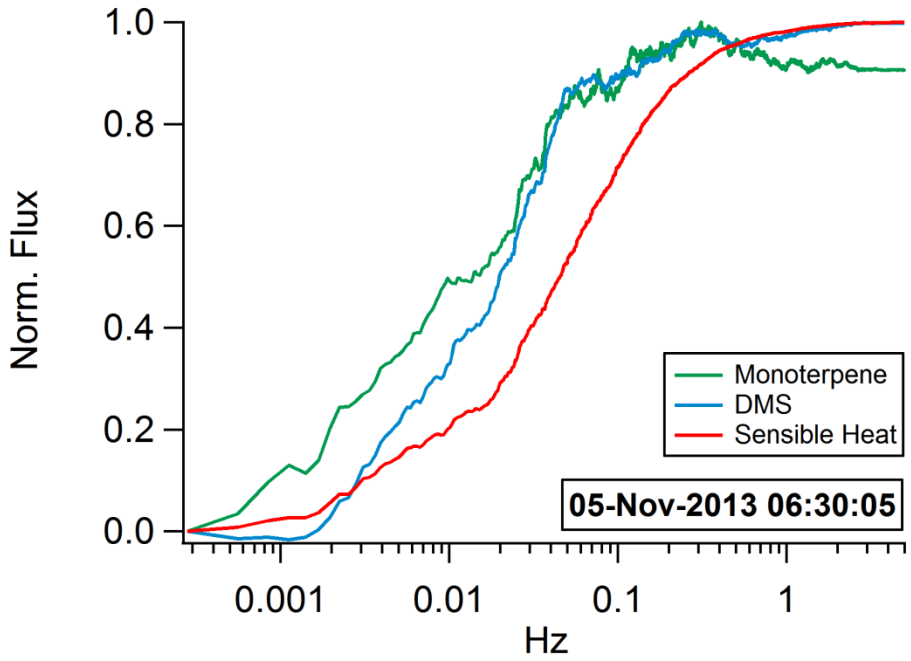

Figure 2.8 A cumulative density function of the normalize flux signal for BVOCs, monoterpenes and DMS, and sensible heat as a function of frequencies driving that flux. The majority of air-sea exchange signal is carried by frequencies between .01 and 1 Hz.

At high frequencies (> 0.5 Hz), it is apparent that some frequency dampening is occurring in the gas sample line. The sensible heat curve more accurately frequency distributions of atmospheric turbulence because it is an open-path sensor.

References

1. Guenther AB, et al. (2012) The model of emissions of gases and aerosols from nature version 2.1 (MEGAN2.1): An extended and updated framework for modeling biogenic emissions. *Geosci Model Dev* 5(6):1471–1492.

2. Watts SF (2000) The mass budgets of carbonyl sulfide, dimethyl sulfide, carbon disulfide and hydrogen sulfide. *Atmos Environ* 34:761–779.

3. Charlson RJ, Lovelock JE, Andreae MO, Warren SG (1987) Oceanic phytoplnakton, atmospheric sulphur, cloud albedo and climate. *Nature* 326(16):655–661.

4. Quinn PK, Bates TS (2011) The case against climate regulation via oceanic phytoplankton sulphur emissions. *Nature* 480(7375):51–56.

5. Chin M, et al. (1996) A global three-dimensional model of tropospheric sulfate acid (MSA). 101.

6. Gondwe M (2003) The contribution of ocean-leaving DMS to the global atmospheric burdens of DMS, MSA, SO_2 , and NSS SO_4. *Global Biogeochem Cycles* 17(2):25–1.

7. Exton D a., McGenity TJ, Steinke M, Smith DJ, Suggett DJ (2015) Uncovering the volatile nature of tropical coastal marine ecosystems in a changing world. *Glob Chang Biol* 21(4):1383–1394.

8. Hu Q-H, et al. (2013) Secondary organic aerosols over oceans via oxidation of isoprene and monoterpenes from Arctic to Antarctic. *Sci Rep* 3:2280.

9. Kruger O, Grassl H, Krüger O, Graßl H (2011) Southern Ocean phytoplankton increases cloud albedo and reduces precipitation. *Geophys Res Lett* 38(8).

10. Meskhidze N, Nenes A (2006) Phytoplankton and cloudiness in the Southern Ocean. *Science (80-)* 314(5804):1419–23.

11. Fu P, Kawamura K, Chen J, Barrie L a. (2009) Isoprene, monoterpene, and sesquiterpene oxidation products in the high arctic aerosols during late winter to early summer. *Environ Sci Technol* 43(11):4022–4028.

12. Fu PQ, Kawamura K, Chen J, Charrière B, Sempéré R (2013) Organic molecular composition of marine aerosols over the Arctic Ocean in summer: Contributions of primary emission and secondary aerosol formation. *Biogeosciences* 10(2):653–667.

13. Colomb A, Yassaa N, Williams J, Peeken I, Lochte K (2008) Screening volatile organic compounds (VOCs) emissions from five marine phytoplankton species by head space gas chromatography/mass spectrometry (HS-GC/MS). *J Environ Monit* 10(3):325–30.

14. Yassaa N, et al. (2008) Evidence for marine production of monoterpenes. *Environ Chem* 5(6):391.

15. Meskhidze N, Sabolis a., Reed R, Kamykowski D (2015) Quantifying environmental stress-induced emissions of algal isoprene and monoterpenes using laboratory measurements. *Biogeosciences* 12(3):637–651.

16. Shaw SL, Gantt B, Meskhidze N (2010) Production and Emissions of Marine Isoprene and Monoterpenes: A Review. *Adv Meteorol* 2010(1):1–24.

17. Milne PJ, Riemer DD, Zika RG, Brand LE (1995) Measurement of vertical distribution of isoprene in surface seawater, its chemical fate, and its emission from several phytoplankton monocultures. *Mar Chem* 48(3-4):237–244.

18. Exton DA, Suggett DJ, Mcgenity TJ, Steinke M (2013) Chlorophyll-normalized isoprene production in laboratory cultures of marine microalgae and implications for global models. *Limnol Oceanogr* 58(4):1301–1311.

19. Zindler C, Marandino CA, Bange HW, Schütte F, Saltzman ES (2014) Nutrient availability determines dimethyl sulfide and isoprene distribution in the eastern Atlantic Ocean. *Geophys Res Lett* 41(9):3181–3188.

20. Shaw SL, Chisholm SW, Prinn RG (2003) Isoprene production by Prochlorococcus, a marine cyanobacterium, and other phytoplankton. *Mar Chem* 80:227–245 ST – Isoprene production by Prochlorococc.

21. Broadgate WJ, Liss PS, Penkett SA (1997) Seasonal emissions of isoprene and other reactive hydrocarbon gases from the ocean. *Geophys Res Lett* 24(21):2675.

22. Broadgate WJ, Malin G, Küpper FC, Thompson A, Liss PS (2004) Isoprene and other non-methane hydrocarbons from seaweeds: A source of reactive hydrocarbons to the atmosphere. *Mar Chem* 88(1-2):61–73.

23. Schwender J, et al. (1997) Incorporation of 1-deoxy-D-xylulose into isoprene and phytol by higher plants and algae. *FEBS Lett* 414(1):129–134.

24. Loreto F, Fineschi S (2014) Reconciling functions and evolution of isoprene emission in higher plants. *New Phytol*:578–285.

25. Silver GM, Fall R (1991) Enzymatic synthesis of isoprene from dimethylallyl diphosphate in aspen leaf extracts. *Plant Physiol* 97(4):1588–1591.

26. Banerjee a, Sharkey TD (2014) Methylerythritol 4-phosphate (MEP) pathway metabolic regulation. *Nat Prod Rep* 31(8):1043–55.

27. Gantt B, Meskhidze N, Kamykowski D (2009) A new physically-based quantification of marine isoprene and primary organic aerosol emissions. *Atmos Chem Phys* 9:4915–4927.

28. Palmer PI, Shaw SL (2005) Quantifying global marine isoprene fluxes using MODIS chlorophyll observations. *Geophys Res Lett* 32(9):1–5.

29. Arnold SR, et al. (2009) Evaluation of the global oceanic isoprene source and its impacts on marine organic carbon aerosol. *Atmos Chem Phys* 9(4):1253–1262.

30. Luo G, Yu F (2010) A numerical evaluation of global oceanic emissions of α-pinene and isoprene. *Atmos Chem Phys* (2008):2007–2015.

31. Baker AR, et al. (2000) Distribution and sea-air fluxes of biogenic trace gases in the eastern Atlantic Ocean. *Global Biogeochem Cycles* 14(3):871.

32. Bertram TH, et al. (2011) A field-deployable, chemical ionization time-of-flight mass spectrometer. *Atmos Meas Tech* 4(7):1471–1479.

33. Baldocchi D, Hincks B, Meyers T (1988) Measuring biosphere-atmosphere exchanges of biologically related gases with micrometeorological methods. *Ecology* 69(5):1331–1340.

34. McGillis WR, Edson JB, Hare JE, Fairall CW (2001) Direct covariance air-sea CO2 fluxes. *J Geophys Res* 106(2000):16729 – 16745.

35. Blomquist BW, Huebert BJ, Fairall CW, Faloona IC (2010) Determining the sea-air flux of dimethylsulfide by eddy correlation using mass spectrometry. *Atmos Meas Tech* 3(1):1–20.

36. Yang M, Blomquist BW, Nightingale PD (2014) Air-sea exchange of methanol and acetone during HiWinGS: Estimation of air phase, water phase gas transfer velocities. *J Geophys Res Ocean* 119(10):7308–7323.

37. Bariteau L, et al. (2010) Determination of oceanic ozone deposition by ship-borne eddy covariance flux measurements. *Atmos Meas Tech* 3:441–455.

38. Blomquist BW, Fairall CW, Huebert BJ, Kieber DJ, Westby GR (2006) DMS sea-air transfer velocity: Direct measurements by eddy covariance and parameterization based on the NOAA/COARE gas transfer model. *Geophys Res Lett* 33:L07601.

39. Foken T, Wichura B (1996) Tools for quality assessment of surface-based flux measurements. *Agric For Meteorol* 78(1-2):83–105.

40. Webb EK, Pearman GI, Leuning R (1980) Correction of flux measurements for density effects due to heat and water vapour transfer. *Q J R Meteorol Soc* 106(447):85–100.

41. Lenschow DH, Raupach MR (1991) The Attenuation of Fluctuations in Scalar Concentrations through Sampling Tubes. *J Geophys Res* 96.

42. Stull RB (1988) *An Introduction to Boundary Layer Meteorology*.

43. Huebert BJ, et al. (2004) Measurement of the sea-air DMS flux and transfer velocity using eddy correlation. *Geophys Res Lett* 31(23):L23113.

44. Wanninkhof R, McGillis WR (1999) A cubic relationship between air- sea CO2 exchange and wind speed. *Geophys Res Lett* 26:1889–1892.

.

Chapter 3

Bacteria driven production of alkyl nitrates in seawater

Aircraft and ship-borne measurements have shown that the ocean is a large, diffuse source for short chain (C1-C3) gas-phase alkyl nitrates ($RONO_2$). Photochemical production of $RONO_2$ has been demonstrated previously as a viable mechanism in surface waters, however, it cannot account for the observed depth profile of $RONO_2$, suggesting an additional, dark $RONO_2$ production mechanism. We present measurements of gas-phase C1-C5 alkyl nitrates emitted from seawater in a controlled mesocosm experiment conducted under low-light conditions in a glass walled wave channel. Ethyl and butyl nitrate emission rates from sea-water are strongly correlated with the abundance of heterotrophic bacteria ($R^2 \geq 0.89$) and show no correlation to chlorophyll-α concentration. Controlled flask experiments conducted using ambient and sterile seawater, inoculated with a heterotrophic bacterium, confirm that bacterial driven production of select $RONO_2$ can proceed efficiently in the absence of light.

1. Introduction

The production rate of tropospheric ozone (O_3), a potent greenhouse gas and radical precursor, is critically dependent on the abundance of nitrogen oxides ($NO_x \equiv NO + NO_2$). In remote regions, the photolysis, chemical processing, and thermal decomposition of reactive nitrogen ($NO_y \equiv NO_x$ + alkyl nitrates ($RONO_2$) + peroxynitrates (RO_2NO_2) + nitric acid (HNO_3) + others) act to control NO_x loadings and in turn, O_3 production rates. Aircraft observations in the equatorial and southern Pacific Ocean have revealed that alkyl nitrates can contribute to as much as 80% of the total NO_y budget in these regions (1), where O_3 production rates are NO_x limited. The lifetime of alkyl nitrates in the troposphere is between days and months depending on the alkyl chain length (2,3) . Atmospheric production of alkyl nitrates is known to proceed through the reaction of alkyl peroxy radicals (RO_2) with nitric oxide (NO), representing a chain termination reaction through the sequestration of both RO_2 and NO.

Aircraft and ship-borne observations in the equatorial and South Pacific Ocean suggest a diffuse oceanic source for short chain (C_1-C_4) alkyl (4-6). Direct measurements of alkyl nitrates in seawater indicate that C_1-C_3 alkyl nitrates can be supersaturated, confirming that the ocean is a source for alkyl nitrates to the atmosphere (7-9). Chemical transport modelling, constrained by atmospheric alkyl nitrate measurements, predict a globally, annually averaged oceanic emission rate of methyl and ethyl alkyl nitrates of 0.35 Tg N yr^{-1}. This equates to approximately 1 Dobson Unit of O_3 and a 2.4% reduction in the lifetime of methane (CH_4) (10).

Recently, Williams et al (11) suggested that oceanic emissions of methyl nitrate could be as large as 0.57 Tg N yr^{-1} and emission of higher order alkyl nitrates could be as large as 0.17 Tg N yr^{-1}. The increased emission rate is balanced in part by a larger dry deposition velocity to the ocean in the source region.

A complete mechanism for oceanic production of alkyl nitrates in seawater that replicates seawater observations has remained elusive. Laboratory and field measurements have demonstrated aqueous photochemical pathways for alkyl nitrate formation, where alkyl peroxy radicals, produced following the photolysis of colored dissolved organic matter (CDOM) react with dissolved NO (12). Dahl and Saltzman (13), through ship-based incubation studies, demonstrated that C_1-C_3 alkyl nitrates could be formed from irradiated seawater, where NO concentrations are sustained by the photolysis of nitrite (NO_2^-). Comparing alkyl nitrate production rates in coastal waters with those previously reported in the North Pacific, Dahl et al. (14) suggested that the molecular nature of CDOM controls relative alkyl nitrate production rates by regulating the relative abundances of their respective peroxy radical precursors. The photochemical production channel has proven to be a viable production mechanism for low molecular weight alkyl nitrates. However, this mechanism cannot explain the vertical distribution of alkyl nitrates observed in seawater. Specifically, Chuck et al. (7) and Dahl et al. (15) report C_1-C_3 alkyl nitrate depth profiles, where elevated alkyl nitrate concentrations are observed down to several hundred meters, where neither local production *via* photochemical pathways nor transport of surface produced alkyl nitrates can sustain the observed concentrations (15). These results suggest a parallel, dark alkyl nitrate production mechanism that may be enzymatically mediated.

Here, we report gas-phase measurements of C_1-C_5 alkyl nitrates made in: 1) an enclosed wave channel during a simulated 5-day mesocosm experiment (16), and 2) controlled flask experiments conducted with ambient and sterile seawater, inoculated with the heterotrophic bacterium *Alteromonas sp.* AltSIO. While the experiments were not designed to directly quantify water side alkyl nitrate production rates, the results permit qualitative exploration of the role of phytoplankton and bacteria in the dark production of C_1-C_5 alkyl nitrates at this location.

2. Experimental

2.1 SIO wave channel and mesocosm experiment

The experiment was conducted in the 33 x 0.5 x 1 m (length x width x height) glass walled wave channel in the Hydraulics Laboratory at the Scripps Institution of Oceanography (SIO). Seawater was pumped directly from the Pacific Ocean to fill the wave channel. Here, we describe a five day mesocosm experiment where on day 1, the wave channel was filled with fresh seawater pumped directly from the SIO pier. During the mescosm experiment, the wave channel was sequentially inoculated with four separate additions of varying combinations of: 1) heterotrophic bacteria isolates (*Alteromonas* sp. AltSIO and TW7, and *Pseudoalteromonas* TW2 and *P. atlantica*, strain 19262), 2) bacterial growth medium (ZoBell 2216E), and 3) a monoculture of marine algae (*Dunaliella tertiolecta*). The timing of the additions and a detailed description of the operation of the wave channel can be found in the supporting information.

2.2 Flask experiments with monocultures of heterotrophic bacteria

Controlled flask studies were conducted to complement the wave channel experiments and study alkyl nitrate production under more controlled seawater conditions. Here, *Alteromonas* sp. AltSIO was inoculated into to an 2.8 L culture flask containing either 1.0 L of sterile seawater or seawater collected from the SIO pier in La Jolla, CA. ZoBell medium concentrate was added (20 mL) to make a 1X final solution (ca. 4.8 g C L^{-1}). Sterile seawater was prepared from plumbed sand/diatomaceous earth filtered seawater described in the Supplemental Information, which was then filtered with 0.2μm polycarbonate disk filters, bubbled with CO_2 (30 s L^{-1}), and autoclaved. Pier water was filtered through a 50μm Nitex mesh upon collection. The flask and tubing was autoclaved then jacketed to prevent photo-initiated radical production mechanisms. The head-space of the flask was monitored continuously in real-time using CI-ToFMS (as described below in section 2.3). In a subsequent small flask experiment, gas phase headspace samples were drawn from the reaction flask for offline confirmation of the presence of alkyl nitrates using GC/MS (Fig. S3.7).

2.3 Gas phase measurements of alkyl nitrates

Short chain alkyl nitrates (C_1-C_5) were measured in real-time at 2Hz *via* chemical ionization time-of-flight mass spectrometry (CI-ToFMS), using protonated water clusters as the reagent ion. The instrument hardware has been described in

detail previously, as applied to the selective detection of organic and inorganic acids using acetate ion chemistry (17). In addition to C_1-C_5 alkyl nitrates, hydrogen sulphide (H_2S) was detected as H^+-H_2S and ammonia (NH_3) as H^+-NH_3 and $H^+(H_2O)_n$-NH_3. Mixing ratios for H_2S and NH_3 are not reported here due to the lack of an in house calibration standard, but the unit mass resolution signal intensity at 35 Th (corresponding to H^+-H_2S is used as a proxy for bacteria abundance. Further information on the CI-ToFMS measurement can be found in the supplemental information.

3. Results

3.1 Alkyl nitrate production during a controlled mesocosm experiment

Fig. 3.1A depicts the biological evolution of seawater in the wave channel, and its response to the sequential additions described in Table S1. The experiment commenced with filling the wave channel with coastal seawater (day 0). Prior to the first addition at day 0.6, the mean chlorophyll-α concentration was 0.18 ± 0.04 mg m^{-3}, mean TOC was 69.1 ± 2.9 μM C, mean photosynthetic eukaryotes was 7.8 x 10^3 ± 4.4 x 10^3 cells mL^{-1}, and mean heterotrophic bacteria was 7.1 x 10^5 ± 4.3 x 10^4 cells mL^{-1}. Approximately one day following the first addition (ca. 1 x 10^{10} cells of the heterotrophic bacteria *Alteromonas* and 18 g C of ZoBell growth media), the measured bacteria number concentrations in the wave channel doubled (from 7.1 x 10^5 to 1.6 x 10^6 cells mL^{-1}), before peaking on day 3 at 6.2 x 10^6 cells mL^{-1}. During this period both chlorophyll-α and the number concentration of photosynthetic eukaryotes

declined steadily, while TOC was slightly enhanced (115.9 μM on day 1). Measured heterotrophic bacteria concentrations responded to the second addition of *Alteromonas* and growth media (day 1.9), displaying a second peak at day 3.5, again approximately 1.5 days after the addition. Since the measurements of the heterotropic bacteria were conducted offline, and thus not available in real time for fine tuning the timing of the additions, two further additions were made to the wave channel before the second peak in heterotrophic bacteria. The third addition (day 2.6) was solely bacteria growth media and the fourth addition (day 2.8) included equal number concentrations of *Pseudoalteromonas atlantica* and *Dunaliella tertiolecta.* The measured chlorophyll-α and photosynthetic eukaryote concentrations respond promptly, rising to 5.5 mg m^{-3} and 1.1 x 10^4 cells mL^{-1} by day 3.5.

The separable enhancements in the concentrations of seawater heterotrophic bacteria and photosynthetic eukaryotes under low light conditions permits assessment of the potential for enzymatically mediated alkyl nitrate production. The time traces for ethyl and butyl nitrate are shown in Fig. 3.1B and 3.1C, where the 30 minute running median is shown with the solid black and blue lines, respectively. The shaded region in both panels B and C represents the variance in the 1Hz measurements. Time traces for methyl, propyl, and pentyl nitrate are shown in supplemental Fig. S3.2. In both Fig. 3.1B and 3.1C, the concentration of heterotrophic bacteria is depicted with red circles. Prior to the first addition (day 0.6), the concentration of C_1-C_5 alkyl nitrates was on average, 40 ± 20, 30 ± 12, < 20, 60 ± 30, and < 20 pptv respectively. The non-zero mixing ratios for C_1, C_2, and C_4 alkyl nitrates reflects either minor

breakthrough of the charcoal filter into the wave channel headspace or non-zero emission from coastal seawater.

As shown in Fig. 3.1B and 3.1C, the ethyl and butyl nitrate mixing ratios track measured heterotrophic bacteria. The mixing ratios for ethyl nitrate ($EtONO_2$) and butyl nitrate ($BuONO_2$) peaked on day 3.25 at 420 and 710 pptv, consistent with peak bacteria concentrations (6.2×10^6 cells mL^{-1}). In contrast methyl nitrate ($MeONO_2$), propyl nitrate ($ProONO_2$), and pentyl nitrate ($PeONO_2$) showed very little enhancement through the bacteria growth phase (Fig. S3.2). In what follows, we focus on the emission of ethyl and butyl nitrate and discuss potential biochemical mechanisms that support enhancement of even carbon numbered alkyl nitrate emissions in Section 4.

$EtONO_2$ and $BuONO_2$ mixing ratios are shown in Fig. 3.2 as a function of the water-side concentration of heterotrophic bacteria and chlorophyll-α. A linear least-squares regression analysis shows a strong positive correlation between $EtONO_2$ and $BuONO_2$ with heterotrophic bacteria throughout the mesocosm experiment (R^2 of 0.89 and 0.9 and P-values of 0.0088 and 0.0391, respectively). In contrast, there is no observable correlation between $EtONO_2$ or $BuONO_2$ mixing ratios and chlorophyll-α or photosynthetic eukaryote abundance. $MeONO_2$, $ProONO_2$, and $PeONO_2$ showed a much weaker correlation with heterotrophic bacteria concentration (R^2 = 0.53, 0.47, and 0.57, and P-values of 0.0462, 0.0939, and 0.4050, respectively) and still no correlation with chlorophyll-α (Fig. S3.3)

For comparison, ocean measurements of heterotrophic bacteria abundance and chlorophyll-α concentration, recently compiled by Li et al. (2004) (18), are shown in

the bottom panel of Fig 3.2. The black line represents the geometric median and the shaded grey region the range in observations for both below and above 50 m. The data shown is a compilation that includes 13,973 concurrent measurements of bacteria abundance and chlorophyll concentration from 15 years of global cruises in the Atlantic, Pacific, Arctic and Antarctic Oceans. The median values reported for bacteria are 6.0×10^5 and 3.3×10^5 cells mL^{-1} for the subset of data above and below 50m, respectively. As such, it should be noted that the bacteria concentrations measured in the wave channel are as much as a factor of ten larger than median ocean conditions, and exceed the highest bacteria concentrations (4.94×10^6 cells mL^{-1}) reported in the Li et al (18) dataset.

3.2 Time-dependent model for alkyl nitrate production from bacteria

In an attempt to place the measured $RONO_2$ mixing ratios in the context of previously reported seawater production rates, we constructed a 0-D time dependent box model to simulate water side $RONO_2$ concentrations in the wave channel. We then estimate the emission rate of C_1-C_5 $RONO_2$ from seawater for comparison with measured $RONO_2$ emission rates calculated from gas-phase concentrations.

Modelled seawater concentrations of $EtONO_2$ and $BuONO_2$ (pM) are shown in panel A with black and blue solid lines, respectively, alongside measured heterotrophic bacteria concentrations (red squares). Modelled emission rates are shown in solid lines in panel B, alongside the emission rates calculated from gas-phase measurements of $EtONO_2$ and $BuONO_2$. The best model-measurement agreement

was achieved when we held k_x at 10 cm hr^{-1} and set c_f at 16 and 24 molecules $cell^{-1}$ s^{-1} for $EtONO_2$ and $BuONO_2$ respectively.

As shown in Fig. 3.3B, the model tends to overestimate $RONO_2$ emission rates following a peak in heterotrophic bacteria concentration (e.g., directly following day 2.0 and day 3.0). This cannot be accounted for in the model with volatilization as the sole loss term. As such, the model-measurement disagreement during these time periods may suggests either: 1) consumption of $RONO_2$ in the seawater that is not accounted for here or 2) a reduction in the per cell production rate of $RONO_2$ at periods of high bacteria abundance, suggesting either that alkyl nitrates are not produced directly by bacteria or that a key nutrient for $RONO_2$ production is limited thus slowing $P_{RONO2.}$ This will be discussed in detail in Section 4.

3.3 Alkyl nitrate production in controlled flask experiments

As shown in Fig. 3.1, alkyl nitrate production is initiated by the simultaneous addition of *Alteromonas* TW7 and AltSIO, and *Pseudoalteromonas* TW2 to the wave channel, approximately 14 hours into the mesocosm experiment. As expected, mixing ratios of hydrogen sulphide (H_2S), a known direct by-product of sulphate reducing bacteria (19), was also strongly correlated with heterotrophic bacteria concentration in the wave channel. As discussed above, the strong correlation (R^2>0.89) between $EtONO_2$ and $BuONO_2$ with heterotrophic bacteria abundance in the wave channel suggests that bacteria govern alkyl nitrate production in this experiment. The controlled flask studies were conducted to shed light on the mechanism by which

heterotrophic bacteria (such as *Alteromonas*) produce alkyl nitrates. Here, *Alteromonas* AltSIO and ZoBell growth media were added to the reaction flask containing sterile seawater. Minor, initial off-gassing of C_1-C_5 alkyl nitrates was observed over the first 6 hours, but returned to baseline values prior to bacteria growth in the flask. Bacteria growth in the flask was monitored periodically through measurements of optical density, while continuous measurement of H_2S concentration in the headspace proved to be an indirect continuous measure of bacterial activity, likely linearly related to bacteria abundance. In what follows, we focus our analysis on $EtONO_2$.

There was no detectable generation of $EtONO_2$ observed in the sterile seawater matrix doped with *Alteromonas* AltSIO, despite significant production of H_2S (ca. 10x that observed in the wave channel). The null result indicates the heterotrophic bacteria AltSIO is not the primary source for alkyl nitrates and that the bacteria mediated alkyl nitrate production observed in the wave channel experiments is likely to be co-dependent on the pool of dissolved organic material. To test this, *Alteromonas* AltSIO was added to the reaction flask containing seawater collected from the SIO pier, again under dark conditions. $EtONO_2$ concentrations directly track H_2S through the bacteria growth phase for the first 24 hours of the experiment (Fig. S3.6). At this time H_2S appears to reach steady state, while $EtONO_2$ concentrations decay back to zero over the following 2 days.

To attain a consistent picture of the factors controlling alkyl nitrate production in the wave channel and flask experiments, $EtONO_2$ signal intensities are shown as a

function of measured CI-ToFMS H_2S signal intensities in Fig. 3.4. Data from the wave channel comprise most of the low intensity signals, yet are highly correlated (R^2 = 0.98). The regression line is extrapolated to higher H_2S values for comparison with the flask experiments that span a wider range in H_2S and $EtONO_2$ concentrations. $EtONO_2$ and H_2S are correlated in both the wave channel experiment and for the first 24 hours of the flask experiments. Following this, ethyl nitrate concentrations exhibit a steady decline over the remaining 48 hours of the experiment, suggesting that either the pool of dissolved organic material has been depleted or that some unknown factor is inhibitory to the production mechanism, thus suppressing alkyl nitrate production. Inhibition might be elicited by a change in chemical conditions such as pH or oxidation-reduction state or by the biochemical production of a molecule that interferes with contributing biosynthetic enzymes, through competitive or regulatory processes. A proposed mechanism, consistent with these results is discussed in Section 4.2.

4. Discussion

4.1 Comparison of alkyl nitrate production rates with prior measurements

A rough comparison of the production rates modelled here can be made with those measured in Dahl et al., (13) during incubation studies performed using seawater samples collected in the North Pacific Ocean, spiked with 1μM nitrite. $EtONO_2$ production rates in that study ranged between 0.6±1.5 and 26.1±8.3 pM hr^{-1} for Warm Pool waters and high chlorophyll-α waters, respectively. $BuONO_2$ concentrations and production rates were not reported. In comparison, our modelled $EtONO_2$ production

rate was 56 pM hr^{-1} for a heterotrophic bacteria concentration of 6.0 x 10^5 cells mL^{-1}. While our model estimate for the dark production rate of $EtONO_2$ in our experiment is of the same order of magnitude of that observed in the Dahl et al.(13) study, our result is not a direct measurement, but a best fit to our model. Nonetheless, our observations made in the wave channel highlight that a bacteria mediated production channel for alkyl nitrates is active, and future work to directly quantify the per cell production rate is warranted. In the following section, we discuss a proposed mechanism for bacteria controlled production of $RONO_2$ from seawater.

4.2 Proposed mechanism for bacteria generated alkyl nitrate production

Several primary (direct) and secondary (indirect) mechanisms are consistent with the dark production of $RONO_2$ observed in both the wave channel and flask experiments. Our experiments rule out the potential for direct production of $RONO_2$ from *Alteromonas* AltSIO in sterile seawater. However, two potential primary production mechanisms are possible: 1) alkyl nitrates are produced directly by other strain(s) of bacteria that become dominant in the experiment, or 2) $RONO_2$ is produced directly by *Alteromonas sp.* AltSIO, but requires the pool of dissolved organic material present in seawater to catalyse production. Based on the studies conducted to date, we cannot rule out these primary production mechanisms.

Alternatively, it is also possible that heterotrophic bacteria could produce $RONO_2$ through secondary production channels, where *Alteromonas* AltSIO generates a limited reactant(s) required for *in situ* production of $RONO_2$ in seawater. We selected *Alteromonas* AltSIO for these studies because its growth and physiology has

been studied in coastal waters (19), and the genomes for *Alteromonas sp.* AltSIO, TW7 and *Pseudoalteromonas* TW2 have been sequenced, thus providing insight on the mechanisms by which $RONO_2$ may be produced. The sequenced genome indicates that AltSIO, like many heterotrophic bacteria, contain nitric oxide synthases (20). Nitric oxide synthases (NOS) have been shown to catalyze the production of nitric oxide (NO) from amino acids (21). If the necessary genes for NO production are expressed, *in situ* alkyl nitrate production could follow an analogous pathway to known photochemical mechanisms, where AltSIO produces NO directly, but alkyl nitrate production is limited by either the availability of peroxy radicals generated from the pool of dissolved organic material or the amino acids required to drive bacteria mediated NO production. Hughes et al (22), using measurements of the vertical distribution of methyl and ethyl nitrate in shallow freshwater lakes, suggested that bacteria may serve as a dark source of NO. Our model predicts that $RONO_2$ production can be rapid (ca. 24 molecules $cell^{-1}$ s^{-1}), suggesting that the production rate of NO by heterotrophic bacteria is fast in these experiment. We are not aware of prior direct determinations of NO production rates for *Alteromonas,* however, studies of NO production rates from terrestrial bacteria have shown that bacteria can efficiently produce NO at rates as high as 135 molecules $cell^{-1}$ s^{-1} (23).

If the alkyl nitrate production observed in these experiments proceeded through a secondary production mechanism involving NO, a parallel, dark production mechanism for peroxy radicals must also be operational. It was recently demonstrated that heterotrophic bacteria (including *Alteromonas*) are capable of efficient, extracellular production of superoxide (O_2^-) and potentially other reactive oxygen

species (ROS) (24). Diaz et al (24) showed that various strains of *Alteromonas* could produce O_2^- as fast as 200 molecules $cell^{-1}$ s^{-1}. In light of this finding, we expect dark production of O_2^-, and likely hydroxyl radicals (OH), following known iron catalysed reactions involving H_2O_2 (25), to be significant in these studies. It follows that bacteria derived ROS may also serve to initiate peroxy radical production following O_2^- and/or OH reactions with the wide range of dissolved organic molecules in surface waters. As such, cogeneration of NO and O_2^- provide the essential initial ingredients to initial prompt alkyl nitrate production in seawater. An interesting result of both the wave channel and flask experiments is that production of even carbon numbered alkyl nitrates (C_2 and C_4) is significantly favoured over the production of odd carbon numbered alkyl nitrates (C_1, C_3, and C_5). This observation may reflect an even-carbon number preference in alkyl nitrate assembly implicating the involvement of biochemical pathways including fatty acid synthesis, fatty acid degradation, and polyketide synthesis. All fatty acid synthases and degradation pathways and many PKS synthases add or remove an acetyl two-carbon unit of in modular fashion resulting in products and intermediates with even numbered acyl chains.

Reactions of nitric oxide in biological matrices have received considerable amount of attention, as NO is released by a wide array of mammalian cells and mediates a host of biological actions [e.g., (26)]. It is believed that bacterial derived NO in the studied bacteria may play similar roles as in mammalian systems but this is not yet well understood (27-28). Cogeneration of NO and O_2^- has been shown to result in peroxynitrite ($ONOO^-$) production, leading to cytotoxic conditions (29). It has been shown that the production of alkyl nitrates in the reaction of lipid peroxy radicals

with NO can serve to inhibit lipid peroxidation (30). It has also been suggested that NO is utilized in bacterial natural product synthases for nitration reactions as well for recovery or protection from radiation exposure or oxidative stress to support virulence (20). If alkyl nitrates are made as consequence of excess NO it may be that alkyl nitrates are an indicator of a bacterial stress response. Whether alkyl nitrates have dedicated biological functions or are just a byproduct of these other processes is not clear at this time.

5. Conclusions and Atmospheric Implications

Our measurements of alkyl nitrate emissions from natural and inoculated seawater matrices suggest that heterotrophic bacteria may play a role in the production of alkyl nitrates, particularly at depth where photochemical production is minimized. It is postulated that alkyl nitrate production in seawater could be initiated by the co-generation of nitric oxide (NO) and superoxide (O_2^-) by bacteria. While the results presented here indicate the role for bacteria in the production of alkyl nitrates, they do not explain existing distributions of $RONO_2$ in marine air, where alkyl nitrates larger than C_3 are rarely observed. At present it is not clear at this time the extent to which this mechanism competes with known photochemical production pathways in the surface ocean or how widespread bacterial production of nitric oxide is relative to that generated from nitrite photolysis. Our results highlight the extreme coupling between biological and chemical mechanisms occurring at the ocean surface and suggest that single component monoculture experiments (either bacteria or phytoplankton) may not capture the mechanisms by which trace gases are produced in the ocean.

6. Acknowledgements

Chapter 3, in full, is a reprint of the material as it appears in Geophysical Research Letters, 2015, with slight modifications. Kim, M.J., Michaud, J. M., Williams, R., Sherwood, B.P., Pomeroy, R., Azam, F., Burkart, M., and T. H. Bertram (2015), "Bacteria-driven production of alkyl nitrates in seawater." *Geophysical Research Letters.* 42(2), 597-604. The dissertation author was the primary investigator and author of this paper.

Figures

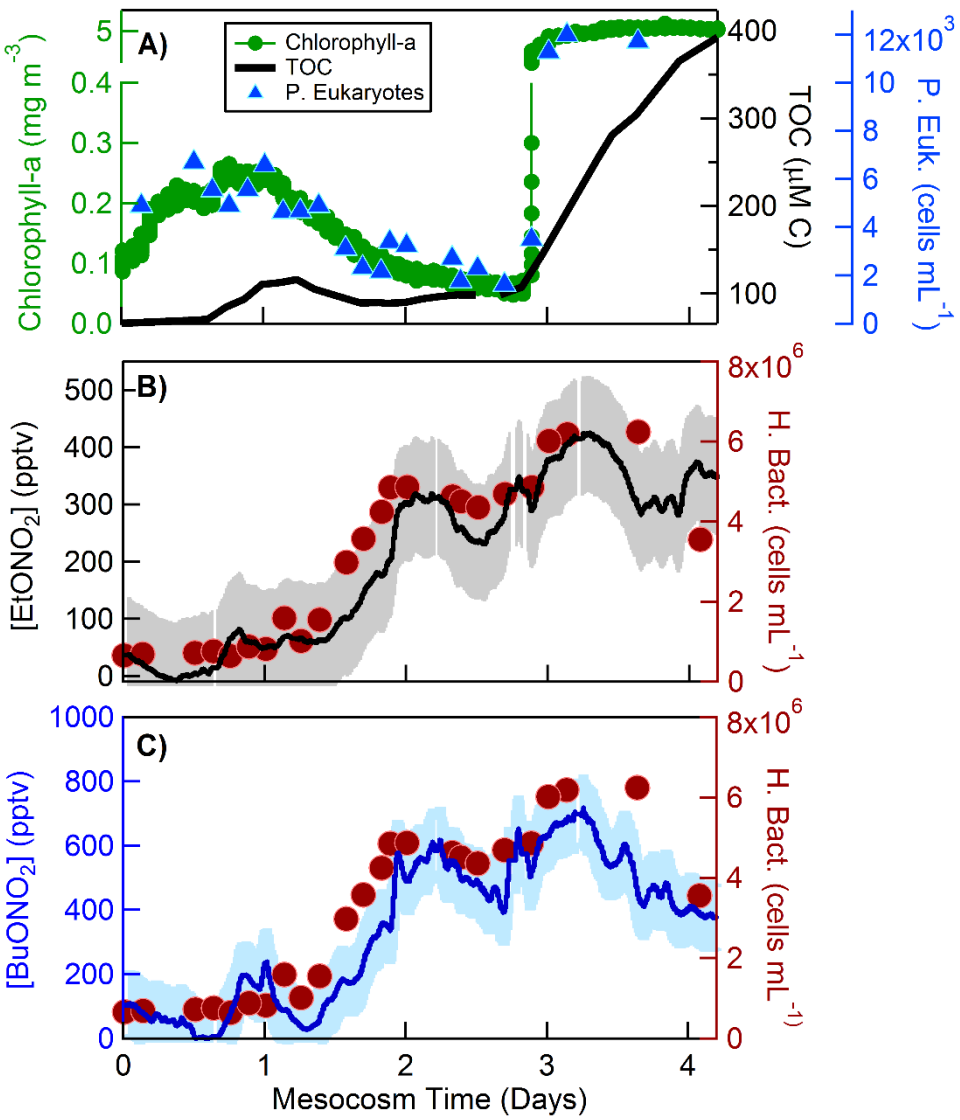

Figure 3.1 A) Time evolution of chlorophyll-α, total organic carbon, and photosynthetic eukaryote abundance in the SIO glass walled wave channel as measured during the November 2011 mesocosm experiment. B,C) Corresponding time series for ethyl nitrate ($EtONO_2$) and butyl nitrate ($BuONO_2$), respectively. The solid line in panels B and C is the 30 minute running median and the shaded region represents the variance in the 1Hz measurements. Waterside concentrations of heterotrophic bacteria (red circles) are shown alongside the $EtONO_2$ and $BuONO_2$ concentration measurements.

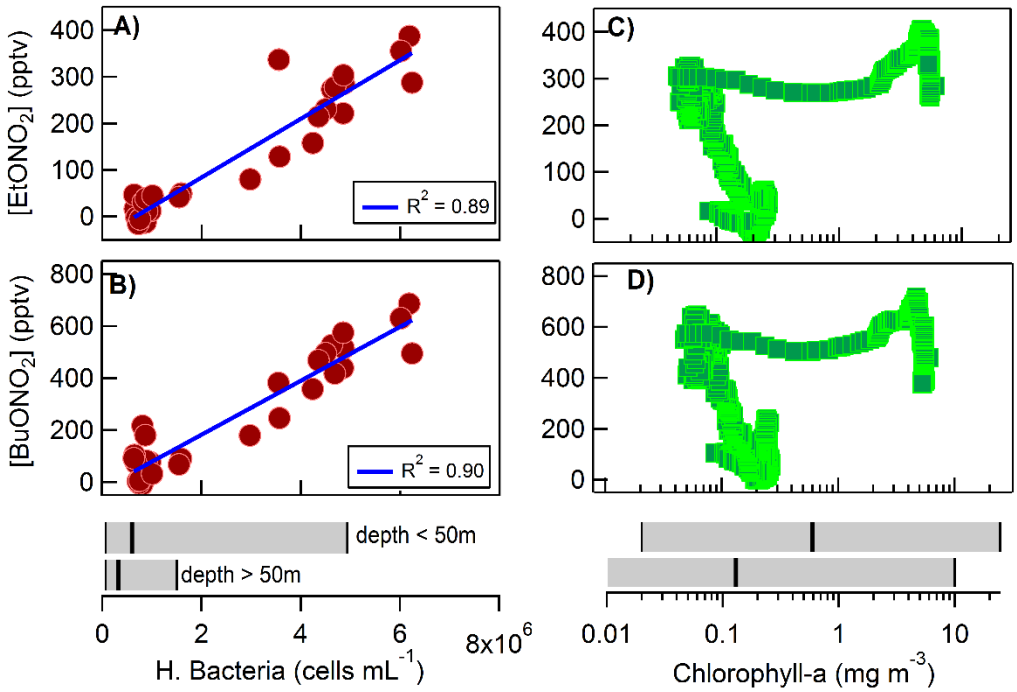

Figure 3.2 Correlation between $EtONO_2$ and $BuONO_2$ with heterotrophic bacteria abundance (A,B) and chlorophyll-α concentration (C,D), respectively as measured in the SIO wave channel during the 2011 mesocosm experiment. Geometric median bacteria and chlorophyll at depths above and below 50 m as reported by Li et al. [2004] (18) from a 15 year dataset from global cruises (n=13,973). The shaded region represents the range in observed concentrations.

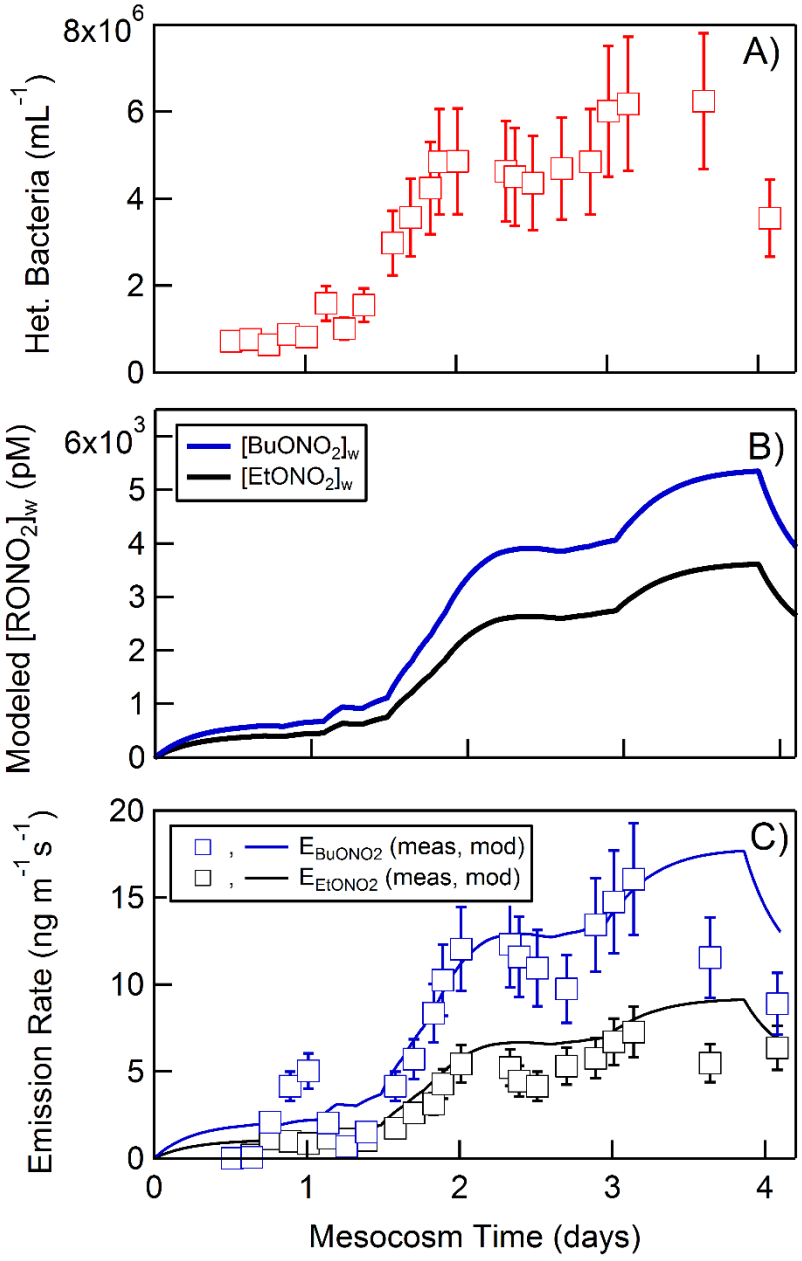

Figure 3.3 A) Measured heterotrophic bacteria concentration in the SIO wave channel during the 2011 intensive measurement campaign (red). Modelled waterside $EtONO_2$ (black) and $BuONO_2$ (blue) concentrations. B) Modelled emission rate of $EtONO_2$ (black lines) and $BuONO_2$ (blue lines) from equation E1, assuming a transfer velocity (k_w = 10 cm hr^{-1}). Emission rates calculated from concentration measurements of $EtONO_2$ and $BuONO_2$ using equation E2 are shown in black and blue squares, respectively.

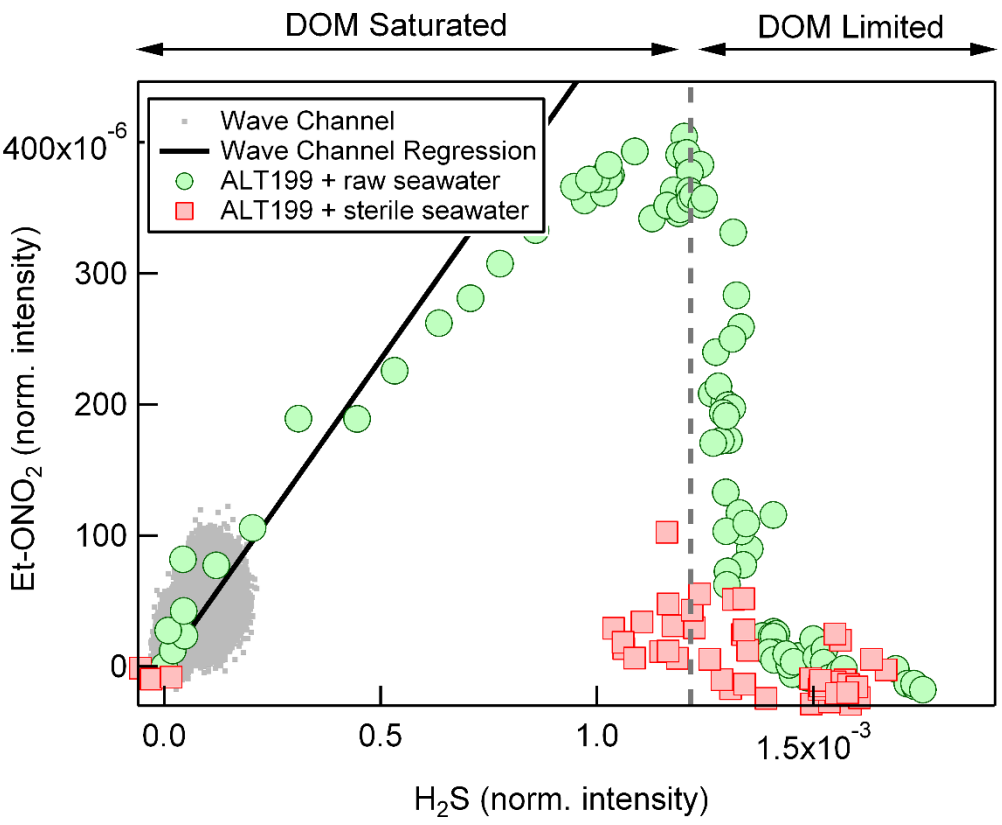

Figure 3.4 Correlation between H_2S and $EtONO_2$ as measured in the wave channel (grey dots) and in the controlled flask experiments using raw, ambient seawater (green circles) and sterilized seawater (red squares) doped with the heterotrophic bacteria *Alteromonas* sp. AltSIO and ZoBell growth media. The solid black line is an extension of the linear regression line for the wave channel mesocosm data to higher H_2S concentrations.

References

1. Talbot, R. W., J. E. Dibb, E. M. Scheuer, J. D. Bradshaw, S. T. Sandholm, H. B. Singh, D. R. Blake, N. J. Blake, E. Atlas, and F. Flocke (2000), Tropospheric reactive odd nitrogen over the South Pacific in austral springtime, *J Geophys Res-Atmos*, *105*(D5), 6681-6694 doi: 10.1029/1999jd901114.

2. Talukdar, R. K., S. C. Herndon, J. B. Burkholder, J. M. Roberts, and A. R. Ravishankara (1997a), Atmospheric fate of several alkyl nitrates .1. Rate coefficients of the reactions alkyl nitrates with isotopically labelled hydroxyl radicals, *J Chem Soc Faraday T*, *93*(16), 2787-2796.

3. Talukdar, R. K., J. B. Burkholder, M. Hunter, M. K. Gilles, J. M. Roberts, and A. R. Ravishankara (1997b), Atmospheric fate of several alkyl nitrates .2. UV absorption cross-sections and photodissociation quantum yields, *J Chem Soc Faraday T*, *93*(16), 2797-2805 doi: 10.1039/A701781b.

4. Atlas, E., W. Pollock, J. Greenberg, L. Heidt, and A. M. Thompson (1993), Alkyl Nitrates, Nonmethane Hydrocarbons, and Halocarbon Gases over the Equatorial Pacific-Ocean during Saga-3, *J Geophys Res-Atmos*, *98*(D9), 16933-16947 doi: 10.1029/93jd01005.

5. Blake, N. J., D. R. Blake, A. L. Swanson, E. Atlas, F. Flocke, and F. S. Rowland (2003), Latitudinal, vertical, and seasonal variations of C-1-C-4 alkyl nitrates in the troposphere over the Pacific Ocean during PEM-Tropics A and B: Oceanic and continental sources, *J Geophys Res-Atmos*, *108*(D2) doi: 10.1029/2001jd001444.

6. Blake, N. J., et al. (1999), Aircraft measurements of the latitudinal, vertical, and seasonal variations of NMHCs, methyl nitrate, methyl halides, and DMS during the First Aerosol Characterization Experiment (ACE 1), *J Geophys Res-Atmos*, *104*(D17), 21803-21817 doi: 10.1029/1999jd900238.

7. Chuck, A. L., S. M. Turner, and P. S. Liss (2002), Direct evidence for a marine source of C-1 and C-2 alkyl nitrates, *Science*, *297*(5584), 1151-1154 doi: 10.1126/science.1073896.

8. Dahl, E. E., S. A. Yvon-Lewis, and E. S. Saltzman (2005), Saturation anomalies of alkyl nitrates in the tropical Pacific Ocean, *Geophys Res Lett*, *32*(20) doi: 10.1029/2005gl023896.

9. Moore, R. M., and N. V. Blough (2002), A marine source of methyl nitrate, *Geophys Res Lett*, *29*(15) doi: 10.1029/2002gl014989.

10. Neu, J. L., M. J. Lawler, M. J. Prather, and E. S. Saltzman (2008), Oceanic alkyl nitrates as a natural source of tropospheric ozone, *Geophys Res Lett*, *35*(13) doi: 10.1029/2008gl034189.

11. Williams, J.E., G. Le Bras, A. Kukui, H. Ziereis, C.A.M. Brenninkmeijer, The impact of the chemical production of methyl nitrate from the NO + $CH3O_2$ reaction on the global distributions of alkyl nitrates, nitrogen oxides and tropospheric ozone: a global modelling study (2014), *Atmos. Chem. and Phys.*, 14, 2363-2382, doi: 10.5194/acp-14-2363-2014.

12. Dahl, E. E., E. S. Saltzman, and W. J. de Bruyn (2003), The aqueous phase yield of alkyl nitrates from ROO+NO: Implications for photochemical production in seawater (vol 30, art no 1271, 2003), *Geophys Res Lett*, *30*(23) doi: 10.1029/2003gl018686.

13. Dahl, E. E., and E. S. Saltzman (2008), Alkyl nitrate photochemical production rates in North Pacific seawater, *Mar Chem*, *112*(3-4), 137-141 doi: 10.1016/j.marchem.2008.10.002.

14. Dahl, E. E., E. M. Heiss, and K. Murawski (2012), The effects of dissolved organic matter on alkyl nitrate production during GOMECC and laboratory studies, *Mar Chem*, *142*, 11-17 doi: 10.1016/j.marchem.2012.08.001.

15. Dahl, E. E., S. A. Yvon-Lewis, and E. S. Saltzman (2007), Alkyl nitrate (C-1-C-3) depth profiles in the tropical Pacific Ocean, *J Geophys Res-Oceans*, *112*(C1) doi: 10.1029/2006jc003471.

16. Prather, K. A., et al. (2013), Bringing the ocean into the laboratory to probe the chemical complexity of sea spray aerosol, *P Natl Acad Sci USA*, *110*(19), 7550-7555 doi: 10.1073/pnas.1300262110.

17. Bertram, T. H., J. R. Kimmel, T. A. Crisp, O. S. Ryder, R. Yatavelli, J. A. Thornton, M. J. Cubison, M. Gonin, and D. R. Worsnop (2011), A field-deployable, chemical ionization time-of-flight mass spectrometer, *Atmos. Meas. Tech.*, *4*, 1963-1987.

18. Li, W.K.W., Head, E.J.H, and Harrison, W.G. (2004), Macroecological limits on heterotrophic bacterial abundance in the ocean, *Deep-Sea Research*, 51, 1529-1540.

19. Pedler, B.E., Aluwihare LI, & Azam F (2014) Single bacterial strain capable of significant contribution to carbon cycling in the surface ocean. *Proceedings of the National Academy of Sciences of the United States of America* **111**(20):7202-7207

20. Crane, B.R., Sudhamsu, J., and Patel, B.A. (2010) Bacterial Nitric Oxide Synthases, *Annual Review of Biochemistry*, 79:445-70.

21. Sal Salard-Arnaud, I., Stuehr, D., Boucher, J.-L. & Mansuy, D. Spectroscopic, catalytic and binding properties of Bacillus subtilis NO synthase-like protein: comparison with other bacterial and mammalian NO synthases. *J. Inorg. Biochem.* **106,** 164–71 (2012).

22. Hughes, C., Kettle, A.J., Unazi, G.A., Weston K., Jones, M.R., Johnson, M.T. (2010) Seasonal variations in the concentrations of methyl and ethyl nitrate in a shallow freshwater lake, Limnol. Oceanorg. 55(1), 305-314.

23. Ren, T., Roy, R., and Knowles, R. (2000), Production and Consuption of Nitric Oxide by Three Methanotrophic Bacteria, *Applied and Environmental Microbiology*, 66, 9, 3891-3897.

24. Diaz, J.M., Hansel, C.M., Voelker, B.M., Mendes, C.M., Andeer, P.F., and Zhang, T. (2013) Widespread Production of Extracellular Superoxide by Heterotrophic Bacteria, *Science* 3401223-1226.

25. Moffett, J.W. and Zika, R.G. (1987) Reaction kinetics of hydrogen peroxide with copper and iron in seawater, *Environmental Science and Technology*, 21(8), 804-810.

26. Nathan, C. (1992), Nitric oxide as a secretory product of mammalian cells, *FASEB J.*, 6(12), 3051-3064.

27. Coletta, C. *et al.* Hydrogen sulfide and nitric oxide are mutually dependent in the regulation of angiogenesis and endothelium-dependent vasorelaxation. *Proc. Natl. Acad. Sci. U. S. A.* **109,** 9161–6 (2012).

28. King, S.B. (2013) Potential biological chemistry of hydrogen-sulfide (H2S) with the nitrogen oxides. Free Radical Biology and Medicine, 55, 1-7.

29. Matheis, G., Sherman, M. P., Buckberg, G.D., Haybron, D.M., Young, H.H., and Ignarro, L.J. (1992) Role L-arginine-nitric oxide pathway in myocardial reoxygenation injury. Am J Physiol 262(2 Part 2): H616-20.

30. O'Donnell, V.B., Chumley, P.H., Hogg, N., Bloodsworth, A., Darley-Usmar, V.M., and Freeman, B.A. (1997) Nitric oxide inhibitoin of lipid peroxidation: Kinetics of reaction with lipid radicals and comparison with □-Tocopherol, *Biochemistry*, 36, 15216-15223.

Supporting Information

Introduction

In what follows we describe important supplementary information on: 1) The SIO wave channel, 2) Chemical Ionization Mass Spectrometric Measurements of alkyl nitrates, 3) GC/MS measurements of alkyl nitrates, and 4) Time dependent box model used to track the temporal evolution of alkyl nitrate production. This information is supported by one table and 8 figures.

SIO wave channel and mesocosm experiment

The wave channel was filled to 0.6 m. The seawater intake is 300m offshore, and 2m above the ocean floor. Seawater is first pumped through two consecutive coarse filter beds (30cm of No. 12 crystal sand, 20cm of pea gravel, and 45cm of rock) prior to being delivered to three $2.2x10^5$ L holding tanks. Seawater is then delivered to the SIO campus, including the Hydraulics lab, where it is again filtered by inline sand and diatomaceous earth filters prior to being added to the wave channel. During the course of experiments, breaking waves were generated continuously (0.6Hz) *via* a hydraulic paddle within the wave channel. The primary purpose of wave breaking was for a concurrent study on sea-spray aerosol production.

The headspace of the wave channel was fully sealed and equipped with an air handling and filtration system to eliminated background aerosol as well as volatile organic compounds (VOC), nitrogen and sulphur oxides. The filtration system consists of four stages: 1) a prefilter, 2) 4mm coal-based, pellet activated charcoal, 3) potassium permanganate ($KMnO_4$), and 4) a 30 x 30 x 29cm HEPA filter. Filter

breakthrough was monitored continuously with a condensation particle counter (CPC, TSI 3010), and a commercial ozone (O_3) and nitrogen oxide (NO_x) detector (Horiba APOA-370 and APNA-370, respectively). The air flow velocity over the wave channel was held to 12.2 cm s^{-1}, equating to a volumetric flow rate in excess of 1400 sLpm. The light intensity in the wave channel was not quantified, however we expect the UV light intensity in the wave channel to be small as: 1) the wave channel is located indoors where the primary light source is the overhead fluorescent lights, 2) the lid is completely opaque, and 3) the glass walls of the wave channel effectively attenuate light up to approximately 350 nm, which would reduce seawater nitrite photolysis as a source for nitric oxide in these experiments [*Chu and Anastasio,* 2007].

Chlorophyll-α concentration was determined in real-time using a WET Labs ECO Triplet fluorometer. Seawater samples were taken every 3-4 hours during the 5-day mesocosm experiment for the offline determination of total organic carbon (TOC) concentrations and number concentrations of heterotrophic bacteria and photosynthetic eukaryotes *via* flow cytometry. Seawater samples collected for flow cytometry were collected in 1 mL polypropylene cryogenic vials, fixed with 50mL of GF/F filtered 10% paraformaldehyde and flash frozen in liquid N_2 before being transferred to a -80°C freezer. Flow cytometry analysis was conducted at the School of Ocean, Earth Science, and Technology (SOEST) Flow Cytometry Facility at the University of Hawaii at Manoa.

CI-ToFMS measurements of alkyl nitrates

In this application, air is drawn from the headspace of the wave channel at 10 slpm through ¼" OD PFA tube, where it is sub-sampled at 1.7 slpm into the ion-molecule reaction chamber of the CI-ToFMS. Protonated water clusters ($H^+(H_2O)_n$) were generated by passing 1.5 slpm of ultra high purity N_2, saturated with water vapour, through a Po-210 radioactive source (NRD P-2021). Under all conditions sampled here, the primary ion count rate was maintained at >90% of the total ion count rate to suppress the potential for secondary ion chemistry.

As a result of the high IMR pressure (70 mbar) and low collisional energies, C_1-C_5 alkyl nitrates in our instrument were detected with minimal fragmentation at the protonated parent ion (e.g., methyl nitrate was detected as H^+-CH_3ONO_2 at 78 m/*Q*) and with either one or two attached water molecules ($H^+(H_2O)_n$-CH_3ONO_2). This is in contrast to the extensive fragmentation of alkyl nitrates observed in traditional proton transfer reaction mass spectrometry [*Aoki et al.*, 2007]. Alkyl nitrate mixing ratios were determined through direct calibration of the instrument with an n-butyl and an n-propyl nitrate standard. The concentrations of the nitrate standards were determined following catalytic conversion of the alkyl nitrate to NO_x, which was subsequently detected *via* chemiluminescence (Thermo Environmental 42C NO-NO_2-NO_x analyzer). Due to the very limited availability of methyl and ethyl nitrate standard, coupled with their instability, we do not have a direct calibration for methyl, ethyl, or pentyl nitrate. As such, we applied the average of the calibration factors retrieved for the n-butyl and n-propyl nitrate standards. The water cluster ion chemistry used here was shown to be much less sensitive toward alkyl nitrates than it is toward other more polar analytes (e.g., dimethyl sulfoxide, ammonia, and acetone). As such, we do not

expect this ion chemistry to be particularly useful for ambient determinations of alkyl nitrates, although it was well suited for the experiments described here at higher alkyl nitrate mixing ratios. In addition to the C_1-C_5 alkyl nitrates, hydrogen sulphide (H_2S) was detected as H^+-H_2S and ammonia (NH_3) as H^+-NH_3 and $H^+(H_2O)_n$-NH_3. Mixing ratios for H_2S and NH_3 are not reported here due to the lack of an in house calibration standard, but the unit mass resolution signal intensity at 35 Th is used as a proxy for the concentration. Baseline measurements were made by overflowing the instrument inlet with ultra-high purity zero air. Further information potential interferences in the CI-ToFMS measurement can be found in the supplemental information.

Given that the CI-ToFMS used for these experiments has low resolving power ($m/\Delta m = 1100$) and the ion chemistry that was employed is not exceptionally specific toward a given class of molecules, there is a possibility that the molecular assignments we have made to the observed ions (78, 92, 106, 120, and 134 Th) is incorrect or incomplete. To assess this possibility, we have scanned all possible molecular matches for the ions observed. Our assignments for the five studied ions was: H^+-CH_3ONO_2, H^+-$CH_3CH_2ONO_2$, H^+-$CH_3(CH_2)_2ONO_2$, H^+-$CH_3(CH_2)_3ONO_2$, and H^+-$CH_3(CH_2)_2ONO_2$ corresponding to protonated C_1-C_5 alkyl nitrates. The vast majority of the molecules with the same nominal mass as those detected are either non-volatile or would not be ionized by $H^+(H_3O)_n$ ion chemistry. A select few amines would be detected if present in the experiment. These include: 2-aminoethanethiol (detected as H^+-$HS(CH_2)_2NH_2$ at 78 Th), trimethylamine (detected as H_3O^+-$N(CH_3)_3$ at 78 Th), 2-(methylthio)-ethylamine (detected as H^+-$CH_3S(CH_2)_2NH_2$ at 92 Th), 3-(methylthio)-propylamine (detected as H^+-$CH_3S(CH_2)_3NH_2$ at 106 Th), 4-(methylthio)-butylamine

(detected as H^+-$CH_3S(CH_2)_4NH_2$ at 120 Th), triethylamine (detected as H_3O^+-$N(CH_2CH_3)_3$ at 120 Th), and 5-(methylthio)-pentylamine (detected as H^+-$CH_3S(CH_2)_5NH_2$ at 134 Th). The primary evidence that the aforementioned amines did not contribute to the signal intensities that we measured comes from the time response of our inlet during background determinations (Fig. S3.1). The inlet used during these experiments was not designed for high transmission of reactive and/or highly polar molecules. As such, the inlet will yield poor time response to such molecules due to inlet wall effects. As shown in Fig. S3.1, the decay in the ammonia signal (detected as H^+NH_3) can be best modelled as bi-exponential decay with a fast time constant depicting the gas-exchange time of the inlet (ca. 1-2 s) and a slow time constant (minutes) that describes the inlet equilibration. In contrast, the decay of the signal at 120 Th (which we have assigned to butyl nitrate) shows only a fast time constant indicating the molecule is not strongly interacting with the inlet. This is inconsistent with the behaviour of the alkyl amines listed above. As such, we conclude that the ions detected at 78, 92, 106, 120, and 134 correspond to the series of C_1-C_5 alkyl nitrates.

Indication of a diel dependence is shown in the time series of $MeONO_2$ (Fig. S3.2). At presence, the source of this is not known. It is likely either a result of the diel temperature fluctuations of the wave channel, temperature driven fluctuations in the air flow rate (driven by fan speed), or a temperature dependence in the CIMS.

GC/MS Measurements of alkyl nitrates

An Agilent 7820A gas chromatographer (GC) was used with a 5975 mass selective detector (MSD) system for the identification of alkyl nitrates. The analytes were collected from the headspace with an air-tight syringe and injected into the GC port with an inlet temperature of 150^{o}C. Separation took place on an Agilent J&W HP-PLOT Q (30 m x 320 μm x 20 μm) column with helium as the carrier gas (flow rate: 0.7 ml/min) in split mode (75:1). The GC method was initiated with an oven temperature of 100^{o}C for 2 min. The temperature was then ramped at 2^{o}C /min until it reached 200^{o}C, and was held at that temperature for 2 min before ramping down to 100^{o}C at 10^{o}C/min (total run time: 65 min). The mass spectrometer was used in full scan mode (range 42:150) with the source and quadrupole temperatures set at 230^{o}C and 150^{o}C, respectively. A sample chromatogram is shown in Fig. S3.7 and the background subtracted, selected ion chromatogram in Fig. S3.8.

Time-dependent model for alkyl nitrate production from bacteria

There are two adjustable parameters in the model: 1) the production rate for C_1-C_5 alkyl nitrates in seawater (P_{RONO2}), and 2) the gas transfer coefficient for air-sea exchange (k_x). It is important to note that neither of these are measured in this experiment. In the model, we relate the water-side production rate of $RONO_2$ to the measured abundance of heterotrophic bacteria, assuming a linear relationship. The conversion factor ($c_f \equiv P_{RONO2}$ / [heterotrophic bacteria]) is expressed in units of molecules cell^{-1}s^{-1} and unique to each alkyl nitrate studied (C_1-C_5). The conversion factors used in this study are shown in Fig. S3.5. The model assumes there are no

waterside losses for $RONO_2$ other than emission to the atmosphere. We calculate the emission rate (or flux) using Equation 1 (E1):

$$E_C = \alpha_C k_x \left([C]_{water} / \alpha_C - [C]_{air} \right) \quad \text{(E1)}$$

where α_C is the dimensionless solubility of the gas in seawater, k_x is the transfer velocity (cm s^{-1}), and $[C]_{water}$ and $[C]_{air}$ are the concentrations of molecule C in the water and air, respectively. Despite very low wind velocities in the wave channel (U = 0.122 m s^{-1}) the transfer coefficient (k_x) is not constrained in this experiment due to continuous wave breaking in the wave channel that disrupts air-sea exchange and sub-surface turbulence. As such, we initially set k_x at 10 cm hr^{-1} broadly consistent with gas transfer parameterizations at low wind speeds [*Johnson*, 2010]. We then iterate to find values for c_f and k_x that best fit the measurements.

To compare with the model calculations, $RONO_2$ mixing ratios as measured in the wave channel were converted to emission rates using a puff model of the wave channel [*Jacob*, 1999]. Here, we integrate the mass balance equation for the time rate of change in the gas-phase concentration of compound C to obtain an analytical expression (E2) for $[C]_x$ as a function of: the initial concentration at the entry point to the wave channel ($[C]_{x0}$), the first order loss rate of C in the channel (k, here taken to be zero), the emission rate from the water surface (E), the height of the air in the wave channel (h = 0.4 m), the air speed in the wave channel (U = 0.122 m s^{-1}), and x the position along the wave channel.

$$[C]_x = [C]_{x_0} e^{-k/U(x-x_0)} + \frac{E}{hk}\left(1 - e^{-k/U(x-x_0)}\right) \quad \text{(E2)}$$

We then solve for the emission rate (E, ng m^{-2} s^{-1}) as a function of time during the mesocosm experiment for comparison with the 0-D box model.

Supplemental Figures

Table 3.1 Timing of the four sequential additions of heterotrophic bacteria, green algae, and bacterial growth medium to the wave channel during the 5-day mesocosm experiment. The approximate quantities of each addition are reported in the right column. At the beginning of the experiment (time = 0 days), fresh seawater, pumped directly from the Scripps Pier was used to fill the wave channel.

Addition #	Time (days)	Material Added	Quantity
1	0.6	Seawater	100 L
		ZoBell media	18 g C
		Alteromonas TW2, TW7, AltSIO	$1x10^{10}$ cells
2	1.9	ZoBell media	13.5 g C
		Alteromonas TW2, TW7, AltSIO	$4.5x10^{12}$ cells
3	2.6	ZoBell media	15 g C
4	2.8	ZoBell media	15 g C
		Pseudoalteromonas atlantica	$1x10^{11}$ cells
		Dunaliella tertiolecta	$1x10^{11}$ cells

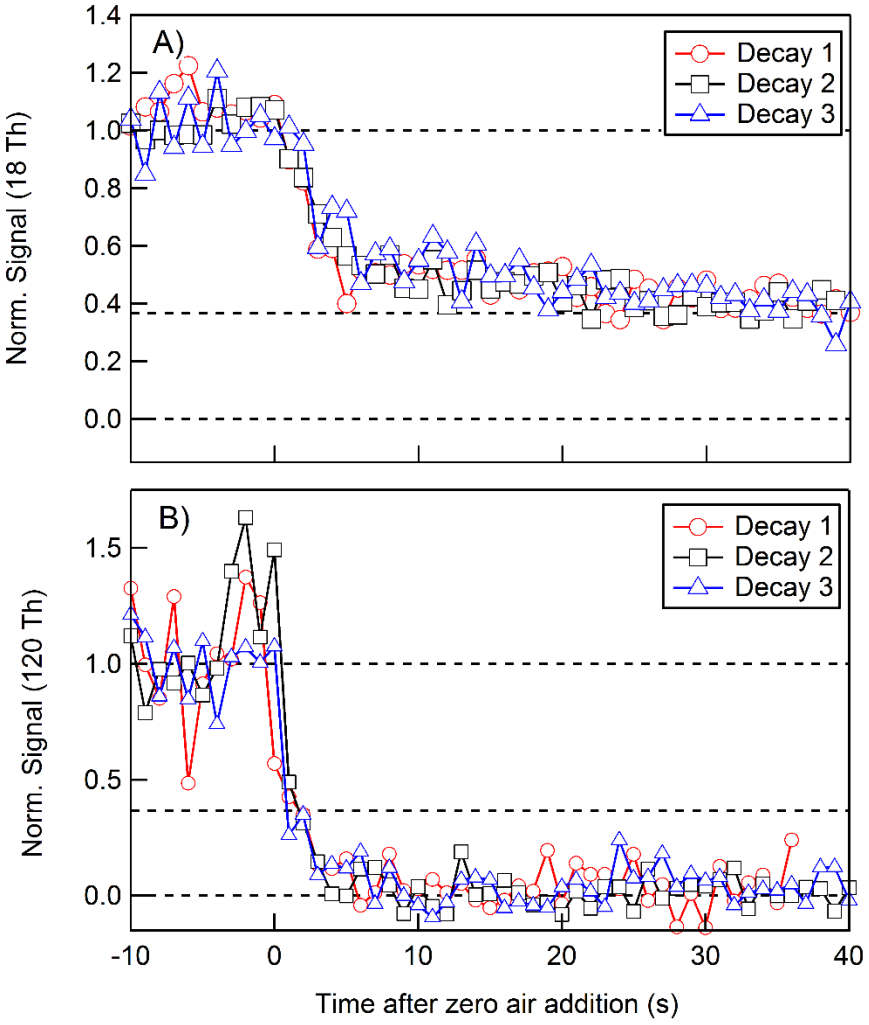

Figure S3.5 A, B) Decay in count rate at 18 Th (assigned as H^+NH_3) and 120 Th ($BuONO_2$, H^+-$CH_3(CH_2)_3ONO_2$) following the injection of dry zero air to the inlet manifold. The decay in the H^+NH_3 signal can be best described by biexponential decay, where the fast time constant is attributed to the gas exchange time of the inlet (ca 1-2 s) and the slow time constant to inlet wall effects. This is typical for a highly polar compound such as ammonia or amines. The decay at H^+-$CH_3(CH_2)_3ONO_2$ is consistent with that expected for an alkyl nitrates, which should display limited inlet wall effects.

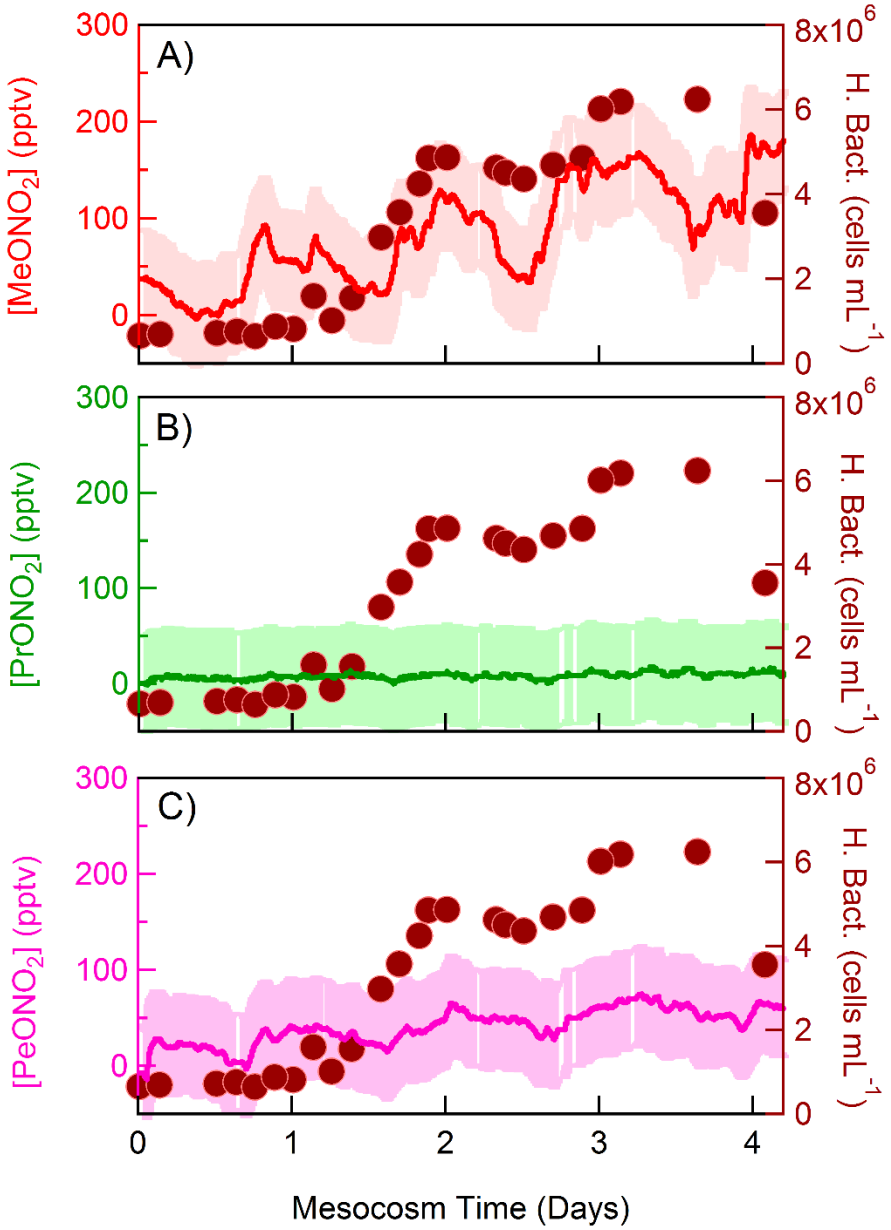

Figure S3.6 Time series for methyl nitrate ($MeONO_2$), propyl nitrate ($ProONO_2$), and pentyl nitrate ($PeONO_2$) during the mesocosm experiment conducted in the SIO wave channel. The solid lines are the 30 minute running median and the shaded region represents the variance in the 1Hz measurements. Waterside concentrations of heterotrophic bacteria (red circles) are shown alongside the $RONO_2$ concentration measurements.

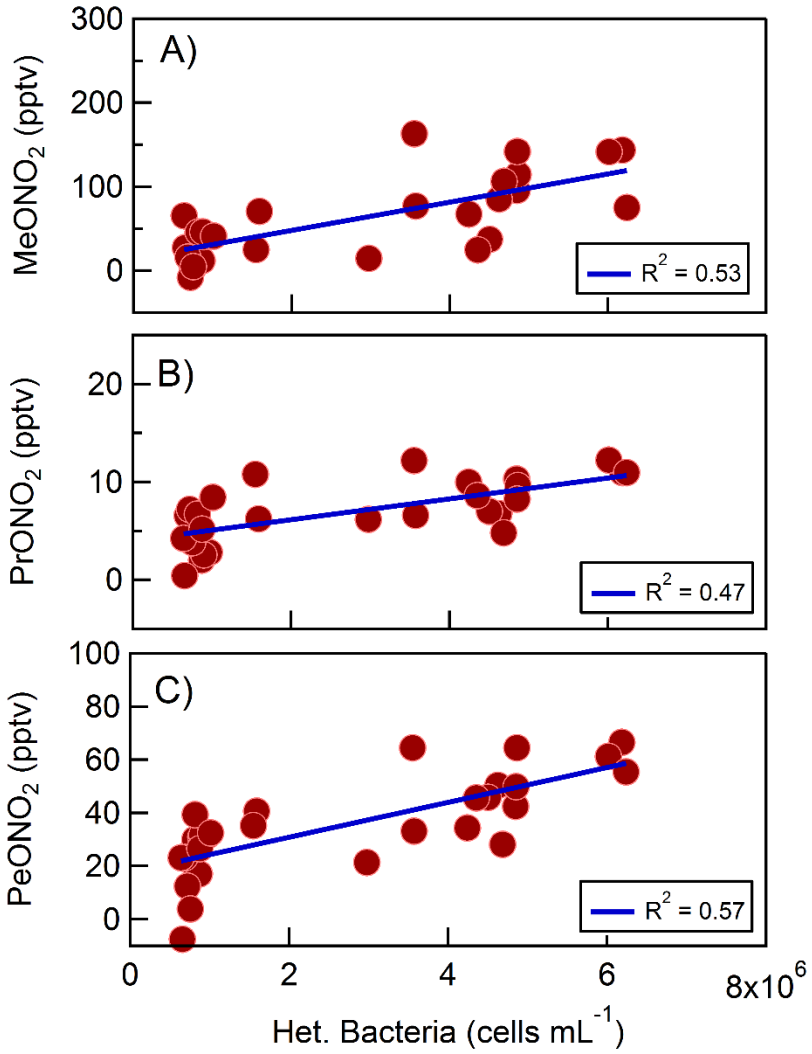

Figure S3.7 Correlation between $MeONO_2$, $ProONO_2$ and $PeONO_2$ with heterotrophic bacteria abundance (A-C) as measured in the SIO wave channel during the 2011 mesocosm experiment.

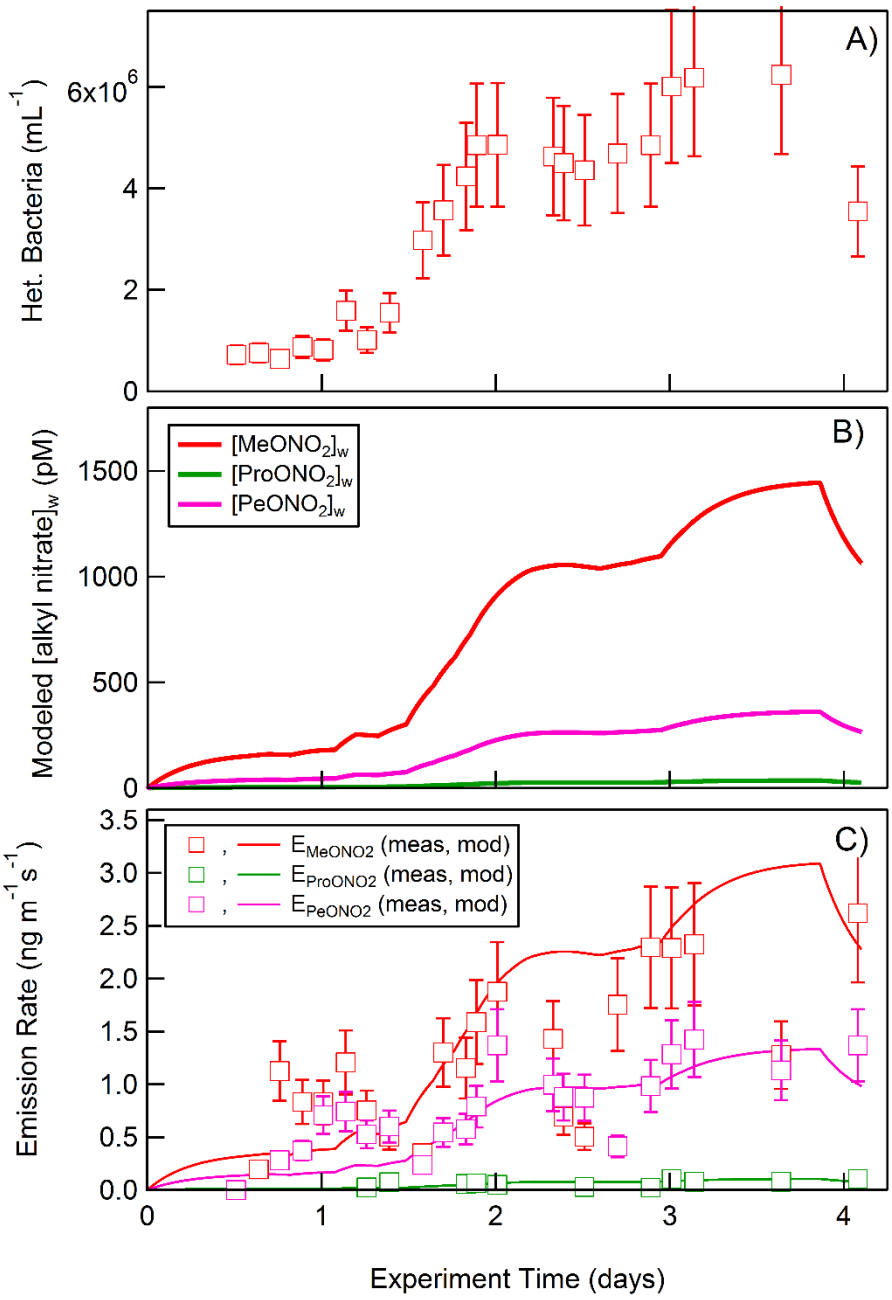

Figure S3.8 A) Measured heterotrophic bacteria concentration in the SIO wave channel during the 2011 intensive measurement campaign. B) Modelled waterside $MeONO_2$ (red), $ProONO_2$ (green), and $PeONO_2$ (pink) concentrations. C) Modelled emission rate of $MeONO_2$ (red lines), $ProONO_2$ (green lines), and $PeONO_2$ (pink lines) from equation E1, assuming a transfer velocity (k_w = 10 cm hr^{-1}). Emission rates calculated from concentration measurements of $MeONO_2$, $ProONO_2$, and $PeONO_2$ using equation E2 are shown in black and blue squares, respectively.

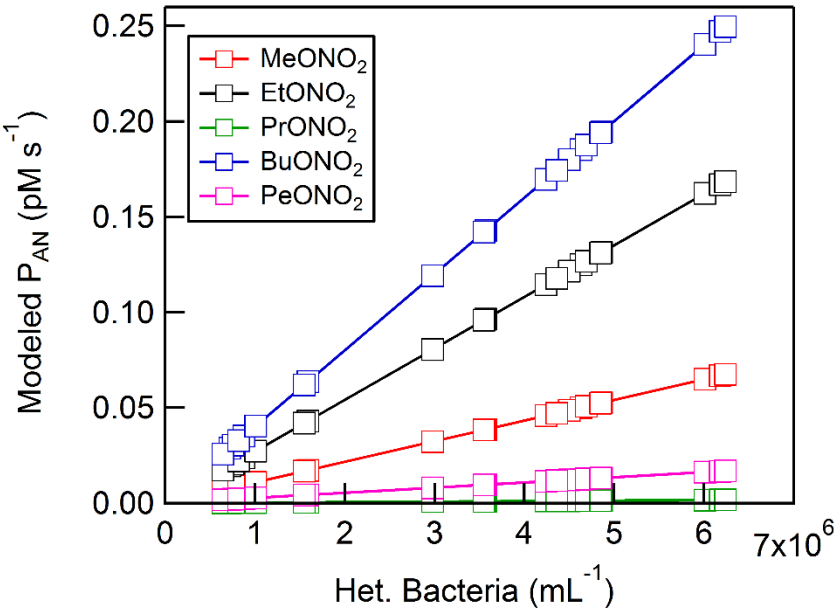

Figure S3.9 Relationship between heterotrophic bacteria concentration and waterside $RONO_2$ production rate (pM s^{-1}) used in the model to match the observed $RONO_2$ emission rates. The slope of each line is the per cell alkyl nitrate production rate (molecules s^{-1} $cell^{-1}$), corresponding to 6.5, 16.3, 0.17, 24.1, and 1.63 for C_1 to C_5 $RONO_2$ respectively.

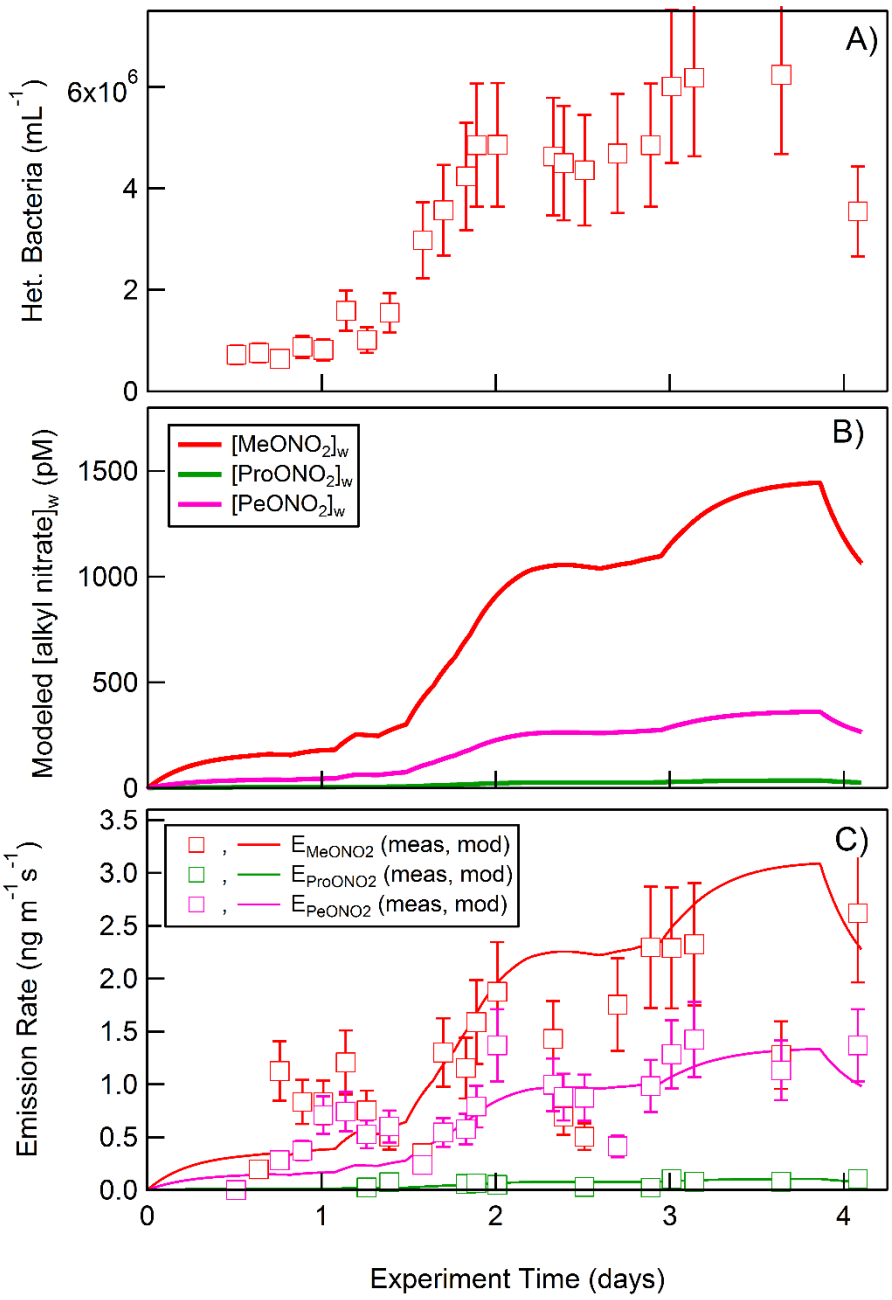

Figure S3.10 A) Measured heterotrophic bacteria concentration in the SIO wave channel during the 2011 intensive measurement campaign. B) Modelled waterside $MeONO_2$ (red), $ProONO_2$ (green), and $PeONO_2$ (pink) concentrations. C) Modelled emission rate of $MeONO_2$ (red lines), $ProONO_2$ (green lines), and $PeONO_2$ (pink lines) from equation E1, assuming a transfer velocity (k_w = 10 cm hr^{-1}). Emission rates calculated from concentration measurements of $MeONO_2$, $ProONO_2$, and $PeONO_2$ using equation E2 are shown in black and blue squares, respectively.

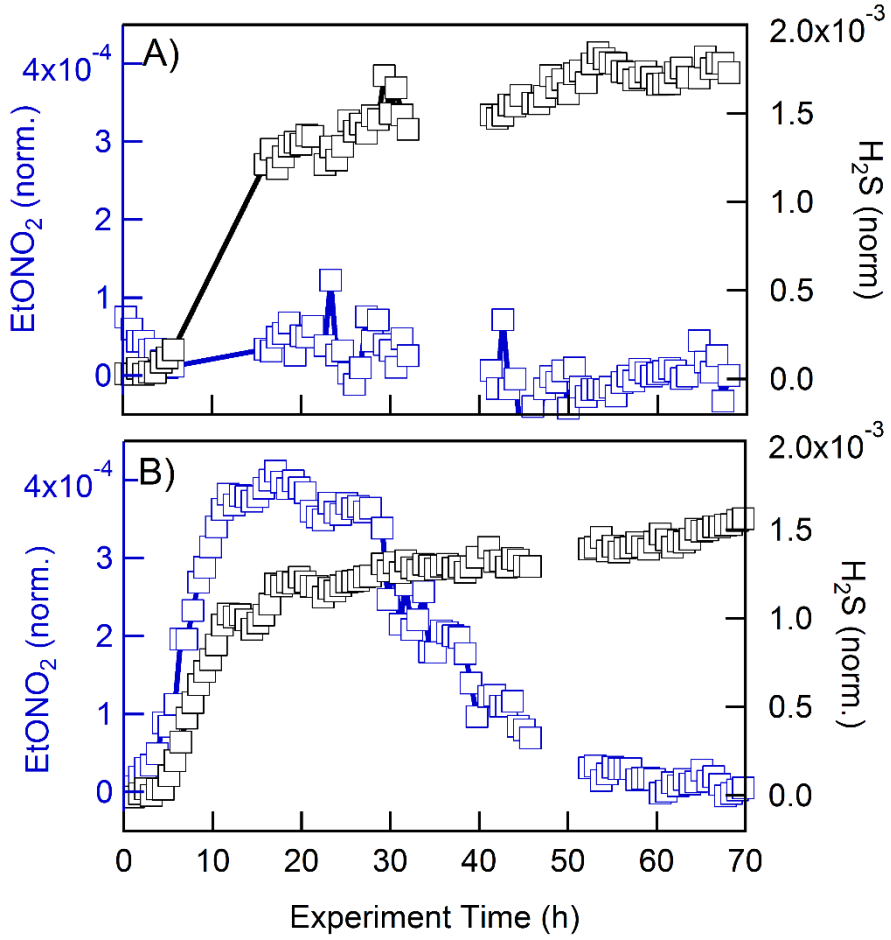

Figure S3.11 Time evolution of $EtONO_2$ and hydrogen sulphide (H_2S) over the course of the controlled flask experiment where the heterotrophic bacteria *Alteromonas* sp. AltSIO and ZoBell growth media was added to sterile seawater (A) and ambient seawater collected from surface waters at the end of the SIO pier. The $EtONO_2$ and H_2S signal intensities have been baseline corrected and normalized to the reagent count rate.

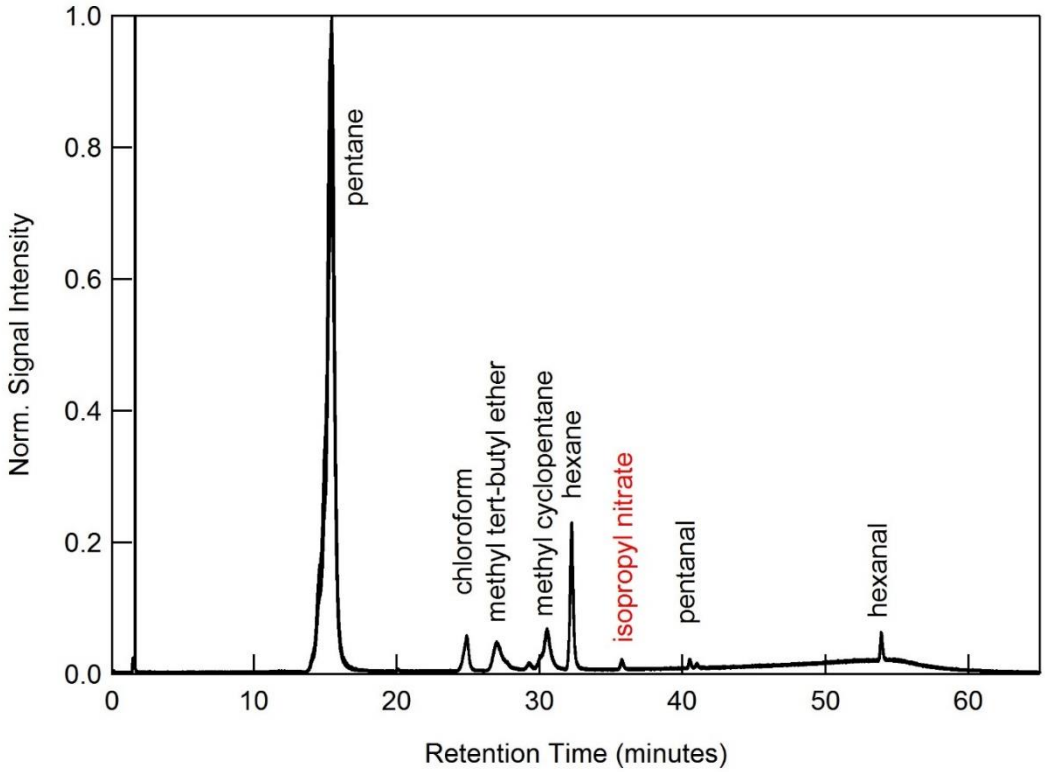

Figure S3.12 Chromatograph from GC/MS for a select unfiltered seawater sample, doped with ZoBell media. This specific sample shows the presence of isopropyl nitrate, alongside a host of other small organic molecules.

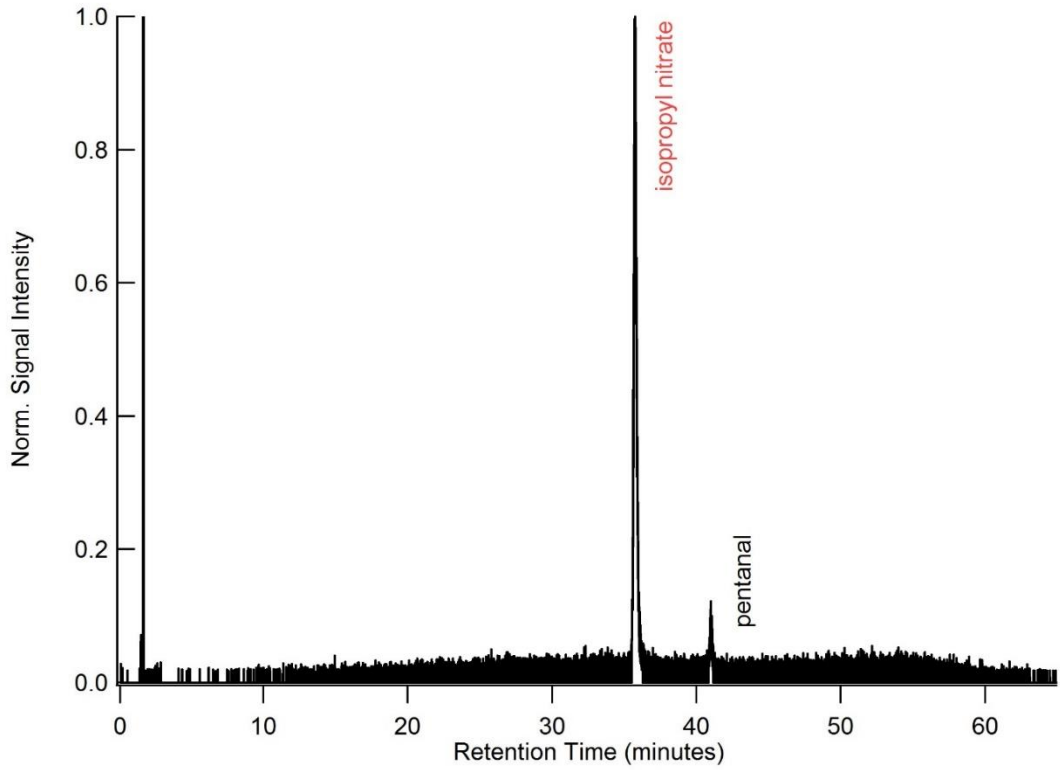

Figure S3.13 Background subtracted selected ion chromatograph from GC/MS for the same sample as Fig. S7, highlighting the enhancement of isopropyl nitrate above a control chromatogram.

Chapter 4

A controlling role for the air-sea interface in the chemical processing of reactive nitrogen in the coastal marine boundary layer

The lifetime of reactive nitrogen and the production rate of reactive halogens in the marine boundary layer are strongly impacted by reactions occurring at aqueous interfaces. Despite the potential importance of the air-sea interface in serving as a reactive surface, few direct field observations are available to assess its impact on reactive nitrogen deposition and halogen activation. Here, we present direct measurements of the vertical fluxes of the reactant-product pair N_2O_5 and $ClNO_2$ to assess the role of the ocean surface in the exchange of reactive nitrogen and halogens. We measure nocturnal N_2O_5 exchange velocities (V_{ex} = -1.66 ± 0.60 cm s^{-1}) that are limited by atmospheric transport of N_2O_5 to the air-sea interface. Surprisingly, vertical fluxes of $ClNO_2$, the product of N_2O_5 reactive uptake to concentrated chloride containing surfaces, display net deposition, suggesting that elevated $ClNO_2$ mixing ratios found in the marine boundary layer are sustained primarily by N_2O_5 reactions with aerosol particles. Comparison of measured deposition rates and *in situ* observations of N_2O_5 reactive uptake to aerosol particles indicates that N_2O_5 deposition to the ocean surface accounts for between 26-42% of the total loss rate. The combination of large $V_{ex,\ N2O5}$ and net deposition of $ClNO_2$ acts to limit NO_x

recycling rates and the production of Cl atoms by shortening the nocturnal lifetime of N_2O_5. These results indicate that air-sea exchange processes account for as much as 15% of nocturnal NO_x removal in polluted coastal regions and can serve to reduce $ClNO_2$ concentrations at sunrise by over 20%.

1. Introduction

The production rate of tropospheric ozone (O_3), a criteria air pollutant, depends critically on the concentrations of nitrogen oxides ($NO_x \equiv NO + NO_2$), volatile organic compounds (VOCs), trace oxidants (e.g., OH, NO_3, and Cl) and the wavelength dependent actinic flux. Accurate model representation of O_3 mixing ratios and the sensitivity of O_3 to changes in NO_x and VOC emissions rely heavily on a complete description of the factors that control NO_x lifetimes and in turn the concentrations of atmospheric oxidants. Modelling studies, constrained by laboratory and field observations, suggest that nocturnal processes involving the nitrate radical (NO_3) and N_2O_5, both products of NO_x oxidation, can account for as much as 50% of the NO_x removal (1). Incorporation of the heterogeneous reaction of N_2O_5 on chloride containing aerosol particles (2-3) serves as both an efficient NO_x recycling and halogen activation mechanism *via* the production of photo-labile nitryl chloride ($ClNO_2$) in both coastal (4) and continental airmasses (5).

To date, study of the impact of nocturnal processes on the lifetime of NO_x and the production of reactive halogen species in the marine boundary layer has concentrated on gas-phase reactions and heterogeneous and multiphase processes occurring on/within aerosol particles, with little attention paid to reactions occurring at the air-sea interface (6-7). With nearly half of the Earth's population living within 200 km of a saltwater coastline, a significant fraction of NO_x emissions are found near coastal waters (4, 8). As such, the chemical evolution of polluted airmasses stemming from coastal mega-cities occurs to a large extent over the ocean (e.g., Beijing plume).

If air-sea exchange of reactive nitrogen compounds is rapid and the reaction kinetics at the air-ocean and air-particle surface are comparable, we expect air-sea exchange processes to play an important role in setting the lifetime of compounds such as N_2O_5 in coastal environments. Specifically, dry deposition of N_2O_5 to the ocean surface could serve to help close the existing gap between models and measurements of N_2O_5 mixing ratios in the polluted marine boundary layer (9). In what follows, we describe direct measurements of the vertical flux of N_2O_5 and $ClNO_2$ obtained *via* eddy covariance at a polluted coastal site to provide observation-based constraints on the role of the air-sea interface in setting the lifetime of reactive nitrogen and the production rate of reactive halogens in the marine boundary layer.

The vertical flux of trace gases across the air-sea interface is a complex function of both atmospheric and oceanic processes, where gas-exchange is controlled by molecular diffusion in the interfacial regions surrounding the air-water interface (10) and the solubility and chemical reactivity of the gas in the molecular sublayer. The flux (F) of trace gas across the interface is described by E1, as a function of both the gas phase (C_g) and liquid phase (C_l) concentrations and the dimensionless gas over liquid Henry's law constant (K_H),

$$F = -K_t\left(C_g - K_H C_l\right) \qquad \text{E1}$$

Where K_t, the total transfer velocity for the gas (cm s^{-1}), encompasses all of the chemical and physical processes that govern air-sea gas exchange (11). As such, accurate, molecule-specific parameterization of K_t is critical for assessing the role of

the ocean as a net source or sink for both greenhouse gases and criteria air pollutants, and the trace gases that control their abundances in the atmosphere.

With respect to N_2O_5 air-sea exchange, we expect the reaction mechanism to closely follow that described for reactions occurring at the air-particle interface, particularly that of sea-spray aerosol. Generally, the reactive uptake of N_2O_5 to aqueous interfaces in the troposphere has been proposed to follow the concerted reaction mechanism (12-13):

$$N_2O_{5\ (gas)} \xleftrightarrow{k_1, k_{-1}} N_2O_{5\ (aq)} \qquad \text{R1}$$

$$N_2O_{5\ (aq)} + H_2O_{liq} \xrightarrow{k_2} H_2ONO_2^{+}{}_{(aq)} + NO_3^{-}{}_{(aq)} \qquad \text{R2}$$

$$H_2ONO_2^{+}{}_{(aq)} + NO_3^{-}{}_{(aq)} \xrightarrow{k_{-2}} N_2O_{5\ (aq)} + H_2O_{liq}$$

$$H_2ONO_2^{+}{}_{(aq)} + H_2O_{liq} \xrightarrow{k_3} H_3O^{+}{}_{(aq)} + HNO_{3\,(aq)} \qquad \text{R3}$$

$$H_2ONO_{2\,(aq)}^{+} + X^{-} \xrightarrow{k_4} XNO_2 + H_2O_{liq} \qquad \text{R4}$$

This mechanism is consistent with laboratory evidence that the reactive uptake of N_2O_5 to aqueous interfaces is dependent on: i) liquid water content (13), ii) nitrate (NO_3^-) and chloride (Cl^-) concentrations (13-15), and iii) the presence of organic surfactants and/or films (16-19). The $ClNO_2$ product yield, $\Phi(ClNO_2)$, following N_2O_5 hydrolysis has been shown to be a strong function of chloride concentration, where $\Phi(ClNO_2)$ is 0.8 for $[Cl^-] = 0.5$ M, increasing to 1.0 for $[Cl^-] > 1.0$ M (2, 13, 20).

Extension of laboratory determined reaction rates (21) and equilibrium constants (2, 22) to the air-sea interface would suggest that N_2O_5 deposition to the

ocean should be rapid (e.g., K_H = 1.9 x 10^{-2}, k_2 = 5 x 10^6 s^{-1}) and that $\Phi(ClNO_2)_{ocean}$ would be > 0.8, based on an oceanic [Cl^-] of 0.55 M . However, the *a priori* estimate for the magnitude and direction of the air-sea flux for $ClNO_2$ (K_H = 1.66) is less clear (2). While laboratory results suggest that $ClNO_2$ should be made at high yield at the ocean surface, it is not clear if water-side transport and subsequent chemical reactions may suppress $ClNO_2$ release back to the atmosphere. Alternatively reaction of the nitronium ion (NO_2^+) in the organic rich sea-surface microlayer (23) may also serve to reduce $\Phi(ClNO_2)_{ocean}$, a reaction that may also proceed in organic rich aqueous aerosol.

2. Results and Discussion

2.1 Eddy covariance measurements of N_2O_5 and $ClNO_2$ air-sea exchange.

Concentration and vertical flux measurements of N_2O_5 and $ClNO_2$ were made at 10 m above sea level (13 m above mean low water) from the end of the 330 m Scripps Institution of Oceanography (SIO) Pier during January and February 2013. Briefly, N_2O_5 and $ClNO_2$ mixing ratios were measured using chemical ionization time-of-flight mass spectrometry (24), utilizing I^- reagent ion chemistry (25). Spectra were saved at 10 Hz, coincident in time with measurements of 3D winds acquired with a co-located ultrasonic anemometer sampling at 20 Hz. Details on instrument calibration, inlet performance, and flux measurements can be found in the Materials and Methods section and the supplemental information.

Here, we discuss a subset of these measurements obtained on 20 February 2013 where the true wind direction ranged between 205-295°, resulting in a purely ocean fetch with pollution from Los Angeles entrained into the sampled airmass. Ten meter wind speeds (u_{10}) ranged between 6.5-11.1 m s^{-1} with a mean and standard deviation of 9.07 ± 1.29 ms^{-1}. The diel profile in N_2O_5 and $ClNO_2$ mixing ratios is shown in Fig. 4.1a-b, where N_2O_5 and $ClNO_2$ mixing ratios track one another for much of the night peaking at midnight. As expected, N_2O_5 mixing ratios drop sharply to zero at sunrise due to rapid photolysis of the nitrate radical (NO_3), which is in thermal equilibrium with N_2O_5, while $ClNO_2$ decays to zero with a time constant (τ = 2.71 hours) consistent with its photolysis lifetime (26). The magnitude of the N_2O_5 and $ClNO_2$ mixing ratios are comparable with those found in previous studies in coastal California (27).

N_2O_5 flux measurements are shown in Fig. 4.2a. As expected, N_2O_5 displays a net downward flux, into the ocean. The magnitude of the flux tracks ambient N_2O_5 mixing ratios yielding a nocturnally averaged exchange velocity (V_{ex}, or flux divided by concentration) of -1.66 ± 0.60 (1σ) cm s^{-1}. We note that a negative V_{ex} indicates a downward flux from the atmosphere to the ocean. $V_{ex,N2O5}$ can be interpreted within the resistance framework developed for O_3 dry deposition, where V_{ex} depends on the aerodynamic resistance, quasi-laminar boundary layer resistance, and the surface resistance that includes chemical reactions at the interface (28). To this end, we calculate the total transfer velocity (K_t) for N_2O_5 (E2) for comparison with the observed exchange rate,

$$K_t = \left[\frac{1}{k_a} + \frac{K_H}{k_w} \right]^{-1} \qquad \text{E2}$$

Where k_a is the air-side transfer velocity, k_w is the water-side transfer velocity, and K_H is the dimensionless gas over liquid Henry's law constant. Over the past two decades, a series of parameterizations (11 and references therein) have been developed that permit calculation of both k_a and k_w as a function of both the molecular properties of the gas (e.g., diffusivity, reactivity, solubility) and physical forcing data (e.g., wind speed). In the case of N_2O_5, the hydrolysis rate (k_2) is sufficiently fast (> 1 x 10^6 s^{-1}) that we expect N_2O_5 deposition to be limited only by the air-side transfer rate (k_a), despite its moderate solubility (K_H = 1.9 x 10^{-2}). As such, we calculate k_a (E3) following the numerical approach of Johnson (29) where the still air diffusive flux of Mackay and Yeun (30) has been added to the representation of k_a found in the NOAA COARE model (31), with a numerical representation of the wind speed dependent drag coefficient (C_D).

$$k_a = 1 \times 10^{-3} + \frac{u^*}{13.3 S_c^{\frac{1}{2}} + C_D^{-\frac{1}{2}} - 5 + \frac{\ln(S_c)}{(2\kappa)}} \qquad \text{E3}$$

Here, u^* is the friction velocity, S_c is the Schmidt number for N_2O_5, and κ is the von Karman constant (taken as 0.4). For comparison, if we neglect fast hydrolysis, N_2O_5 deposition is controlled by the surface resistance due to its moderate solubility and slow diffusion rate in water (D_l = 1.9 x 10^{-5} cm^2s^{-1}) (32). Calculations of the total transfer velocity of N_2O_5 as a function of wind speed are shown in Fig. 4.3, with (solid black lines) and without (dashed black line) surface hydrolysis. In the latter case, we

calculate k_w, again following the numerical approach of Johnson (29). Also included in Fig. 4.3 are the wind speed dependent parameterizations for $k_a(N_2O_5)$ of Liss (33) and Mackay and Yeun (30) both derived from wind tunnel studies and that of Duce et al. (34) which is calculated from micrometeorological theory. The nocturnally averaged measured N_2O_5 exchange velocity is shown in blue squares in Fig. 4.3. As shown, the observed exchange rate is on average a factor of 2.17 larger than that calculated using E3, however it is in agreement with the parameterizations of Liss (10) and Mackay and Yeun (30), to within the uncertainty and variability of the measurements. Longer term observations of F_{N2O5}, designed to capture wide variability in wind speed, will provided unique observation based constraints on k_a, while permitting the opportunity to assess the impact of entrainment of N_2O_5 and $ClNO_2$ from the free troposphere and vertical gradients in temperature and aerosol surface area on the retrieved fluxes.

Our *a priori* supposition for the direction of the $ClNO_2$ flux, based on laboratory determined reaction rates and equilibrium constants, is assumed to be out of the ocean, where hydrolyzed N_2O_5 produces NO_2^+ ions that rapidly react with Cl^- forming $ClNO_2$ in high yield at the ocean surface. Given the N_2O_5 deposition rate measured above, combined with the moderate solubility of $ClNO_2$, one would expect the magnitude of the flux to be nearly equal, yet opposite in direction to N_2O_5. Surprisingly, vertical fluxes of $ClNO_2$ show net deposition, with the exception of the period between 03:00 - 06:00, where the $ClNO_2$ flux indicates net emission from the sea-surface (Fig. 4.2B).

2.2 Modelling sea-surface chemistry of deposited N_2O_5.

To further our understanding of N_2O_5 reactions at the ocean interface, we construct a coupled atmosphere-surface ocean time-dependent box model following the framework outlined in Carpenter et al. (35). The model is constrained by the measured N_2O_5 vertical flux reported above and N_2O_5 and $ClNO_2$ reaction rates, product branching ratios, and diffusion constants as previously determined in the literature for reactions occurring at the air-particle interface. As in Carpenter et al. (35), we define a surface aqueous layer (δ) with a depth equal to the reacto-diffusive length (E4) for the N_2O_5 reaction mechanism (R1-4)

$$\delta = \sqrt{\frac{D_l}{k_r}} \qquad \text{E4}$$

where D_l is the N_2O_5 liquid phase diffusion constant ($D_l = 1.9 \times 10^{-5}$ $cm^2 s^{-1}$) (32), and k_r is the total reactivity of N_2O_5 in seawater (k_r), taken as the N_2O_5 hydrolysis rate (k_2) (21) as the lifetime of the nitronium ion (NO_2^+) product is estimated to be less than 10^{-9} s making the hydrolysis the rate limiting step in the mechanism (2). We expect the reaction to occur in a thin film (δ < 100 nm), well within the molecular sublayer (ca. 10^{-3} m) where transport is driven by molecular diffusion (28). As a result, rapid volatilization of reaction products of relatively high solubility may occur following the supersaturation of dissolved gas in the thin film. For simplicity, mass transfer velocities (K_t) and the associated vertical flux for $ClNO_2$ are calculated in the model using k_a (E1) and k_w (E2) parameterizations as described in

Johnson (29). As in Carpenter et al. (35), mixing from the bulk, where [$ClNO_2$] is taken to be zero, to the interfacial region is determined by the wind speed dependent expression for the transfer velocity.

To explore the apparent downward measured flux of $ClNO_2$, we drive the coupled atmosphere-ocean model using three plausible sets of input values in the treatment of K_t. In model case 1 (C1), our *a priori* conditions were based on existing laboratory based measurements, where model input parameters were taken as suggested in the literature: K_H ($ClNO_2$) = 1.66, $\Phi(ClNO_2)_{ocean}$ = 0.8, $k_r = 5 \times 10^6$ s^{-1}, $\delta = 1.5 \times 10^{-6}$ cm. As shown in Fig. 4.2B, this results in a strong upward flux (sea to air) of $ClNO_2$ that at its maximum is approximately half the magnitude of the N_2O_5 peak flux. This difference is due to the prescribed $ClNO_2$ product yield coupled to exchange with the bulk ocean. In model case 2 (C2), we set the model input parameters at the 90% confidence limits of those suggested in the literature, in the direction of reducing the upward flux of $ClNO_2$ (e.g., K_H ($ClNO_2$) = 0.32, $\Phi(ClNO_2)_{ocean}$ = 0.5, $k_r = 2 \times 10^5$ s^{-1}, $\delta = 7.1 \times 10^{-6}$ cm). This results in a factor of two reduction in peak $ClNO_2$ flux, but the direction of the flux is still positive and outside the uncertainty of the measurements for much of the night. In model case 3 (C3), we take Φ $(ClNO_2)_{ocean}$ = 0, suggesting that perhaps NO_2^+ does not react with Cl^- as expected, but proceeds *via* nitration reactions (36) with enriched organic material found in the sea-surface microlayer (23). It is only by setting the $ClNO_2$ product yield to zero or invoking rapid $ClNO_2$ aqueous phase reaction kinetics or hydrolysis that we can force the model near the uncertainty limits of the measurements.

For the conditions sampled here, $ClNO_2$ production rates were less than 3.0 x 10^{-3} ppt s^{-1} (calculated for the median observed k_{het}, $\Phi(ClNO_2)_{ocean}$ = 1, and $[N_2O_5]$ = 50 pptv) and the $ClNO_2$ steady-state lifetime with respect to loss to gas phase and aerosol reactions is estimated at greater than 30 hours (4). As a result, it is unlikely that significant gradients in $ClNO_2$ exist in the nocturnal marine boundary layer due to vertical gradients in the $ClNO_2$ atmospheric production rate. As such, our measurements of the vertical flux of $ClNO_2$, presented here, are most consistent with a model where the product yield of $ClNO_2$ is near zero for reactions of NO_2^+ in the sea-surface microlayer, and/or $ClNO_2$ aqueous phase reactions are significantly faster than the volatilization rate.

2.3 Relative roles of the particle and ocean surface in regulating $\gamma(N_2O_5)$.

To assess the relative roles of the ocean and aerosol surface in the net removal of N_2O_5, both reactant transport and surface reactivity must be considered. At a marine boundary layer inversion height (z_i) of 810 m, taken as the nocturnally averaged z_i observed during DYCOMS-II off the coast of San Diego (37), the total aerosol surface area ranges between 5 - 50% of the surface area of a slab ocean, based on aerosol surface area measurements made at the SIO pier. In gas-aerosol reactions, transport of the reactant to the particle surface is set by the gas-aerosol collision rate, which is a function of the mean molecular speed of the reactant and the total suspended aerosol surface area (E2). In contrast, reactions occurring at the ocean surface require turbulent transport of the reactants to the diffusive sublayer, where turbulence is suppressed and molecular diffusion controls the collision rate of the

reactant with the ocean surface. We compare N_2O_5 deposition rates (k_{dep}, E5) with N_2O_5 heterogeneous aerosol reaction rates ($k_{aerosol}$, E6), both directly measured at the SIO pier.

$$k_{dep} = -\frac{V_{ex}}{z_i} \qquad \text{E5}$$

$$k_{aerosol} = \frac{\gamma(N_2O_5)\omega S_a}{4} \qquad \text{E6}$$

Here, V_{ex} is the measured N_2O_5 exchange velocity, z_i is the marine boundary layer inversion height, $\gamma(N_2O_5)$ is the N_2O_5 reactive uptake coefficient, ω is the molecular velocity for N_2O_5, and S_a is the aerosol surface area concentration. Measurements of $k_{aerosol}$ at this location have been described previously (38), where the median $k_{aerosol}$ was observed to be 6.04 x 10^{-5} s^{-1} with an interquartile range of 4.5-7.4 x 10^{-5} s^{-1}, where $k_{aerosol}$ was a strong function of particle nitrate and organic mass fractions. As described above, the mean V_{ex} was -1.66 ± 0.60 cm s^{-1} measured at an average wind speed of 9 ms^{-1}, corresponding to a range in k_{dep} of 0.17 – 1.7 x 10^{-4} s^{-1} for z_i between 1000 and 100 m, respectively.

The relative strengths of the ocean and the aerosol surface in the net removal of N_2O_5 from the atmosphere is shown in Fig. 4.4, where the fraction of N_2O_5 lost to the ocean surface is shown as a function of k_{dep} and $k_{aerosol}$. As indicated by the dashed box, the fraction of N_2O_5 removed by the ocean surface ranges between 19 and 79% for the conditions sampled at the SIO pier, where shallow boundary layers ($1000 < z_i < 100$m) and high wind speeds combined with suppressed N_2O_5 heterogeneous reactivity, result in large fractions of N_2O_5 being lost at the air-sea interface. For z_i =

810m (37) and $k_{aerosol}$ = 6.04 x 10^{-5} s^{-1}, the fraction of N_2O_5 lost at the air-sea interface is 32%, ranging between 26-42% for the interquartile range in $k_{aerosol}$. It is important to note that the measurements described here were made at wind speeds significantly larger than the annual median wind speed measured at the SIO pier (2.1 m s^{-1}). Based on the parameterized dependence of K_t on wind speed, it is expected that the range in k_{dep} reported in Fig. 4.4 may be a factor of 3 smaller at lower wind conditions, resulting in the fraction of N_2O_5 removed by the ocean surface to between 7 - 55% (1000 > z_i > 100m). In addition, increased aerosol surface area concentrations under low wind speeds, due to reduced dilution of aerosol from an urban source, may also serve to reduce the fraction of N_2O_5 removed by the ocean surface at low wind speed.

2.4 NO_x removal rates and $ClNO_2$ production.

At present, the majority of steady-state box model analyses as well as regional scale chemical transport models designed to assess nocturnal NO_x chemistry do not include either N_2O_5 or $ClNO_2$ deposition to the ocean surface or the possibility for reaction at the air-sea interface (39-40). Here, we use a 0-D time-dependent box model to assess the impact of air-sea exchange on NO_x removal rates and Cl atom production rates in the polluted marine boundary layer. The box model was run under four different N_2O_5 deposition rates at two different values of $\Phi(ClNO_2)_{ocean}$, 0 and 0.8. It is important to note that the impact of N_2O_5 loss mechanisms on NO_x removal rates and Cl atom production is coupled to nitrate radical (NO_3) chemistry, where reaction of NO_3 with dimethyl sulphide (DMS) can act as the primary loss process for

nocturnal nitrogen oxides. In the model described here, DMS concentrations are set to 100 pptv, corresponding to a loss rate of 2.6 x 10^{-3} s^{-1} for NO_3. Model details can be found in the supporting information as well as the materials and methods section.

To assess the importance of deposition processes on reactive nitrogen and halogen budgets in coastal, polluted regions, we first examine the fraction of NO_x present at sunset, $[NO_x]_{sunset}$, that is lost to terminal sinks at night as a function of the N_2O_5 exchange velocity and $ClNO_2$ product yield.

$$F\left(NO_x\ lost\right) = \frac{\left[NO_x\right]_{Sunset} - \left[NO_x\right]_{Sunrise}}{\left[NO_x\right]_{Sunset}} \qquad \text{E7}$$

As shown in Fig. 4.5a, constraining the model with the measured V_{ex} (-1.66 cm s^{-1}), z_i = 500 m and our best estimate of the yield of $ClNO_2$ produced at the ocean surface ($\Phi(ClNO_2)_{ocean} = 0$), results in an approximate 14% increase in the fraction of NO_x that is lost to terminal sinks at night, as compared to the model that neglects deposition (0.58 to 0.66). This trend shown in Fig. 4.5a describes the increasing fraction of NO_x that is deposited to the ocean surface, where at the limit of $\Phi(ClNO_2)_{ocean} \rightarrow 1$, approximately half of deposited N_2O_5 is returned to the atmosphere as $ClNO_2$ and in the limit of $\Phi(ClNO_2)_{ocean} \rightarrow 0$, all of the deposited N_2O_5 is terminally lost from the atmosphere. Model scenarios that neglect deposition or prescribe a high $ClNO_2$ product yield at the air-sea interface are efficient in recycling NO_x, where as much as 50% of reacted N_2O_5 is returned as NO_2 in the early morning following the photolysis of $ClNO_2$ (Fig. 4.5b). Further, these model scenarios will

result in higher concentrations of $ClNO_2$ at sunrise, as compared to models that include deposition and low $\Phi(ClNO_2)_{ocean}$.

Our observations suggest that N_2O_5 deposited to the ocean surface is terminally lost, thus limiting NO_x recycling rates and Cl atom production that would otherwise be sustained by heterogeneous mechanisms at the air-particle interface. As shown in Fig. 4.5b, including deposition to the ocean surface and neglecting $ClNO_2$ surface production results in nearly a 20% reduction in the concentration of $ClNO_2$ at sunrise, as compared to a model that does not include N_2O_5 deposition. For comparison, including deposition to the ocean surface at the rates measured here, with a high $ClNO_2$ surface yield (0.8) results in nearly a 10% increase in the concentration of $ClNO_2$ at sunrise. This analysis highlights the sensitivity of the nocturnal nitrogen and halogen budget to N_2O_5 deposition and the resulting chemistry in the sea-surface microlayer.

2.5 Atmospheric Implications

We present an analysis of the first direct measurements of N_2O_5 and $ClNO_2$ air-sea exchange using eddy covariance. Our results indicate that N_2O_5 deposition to the ocean surface is rapid (V_{ex} = -1.66 ± 0.60 cm s^{-1}). We find no evidence for net $ClNO_2$ production at the air-sea interface in this study, suggesting either that rates of aqueous phase reactions of $ClNO_2$ in the sea-surface microlayer (SML) are competitive with volatilization, or that the product yield for $ClNO_2$ is small in the organic rich SML. Comparison with direct measurements of the N_2O_5 loss rate to

aerosol particles at the same sampling location indicates that the ocean surface serves on average to remove 32% of N_2O_5 in the marine boundary layer under the conditions sampled here (assuming z_i = 810m). Our results suggest that future measurements of the exchange velocities of N_2O_5 under a wide range of wind conditions will provide needed constraints on parameterizations of the air-side transfer rate (k_a). We hypothesize that measurements of the flux of $ClNO_2$ will display large spatiotemporal variability and be responsive to the chemical composition and concentration of dissolved organic material in the surface ocean due to the competition reactions of the nitronium ion with dissolved organic matter (DOM) and halogen ions. Our results suggest that regional modelling efforts designed to assess the impact of nocturnal nitrogen chemistry on oxidant loadings in coastal polluted environments need to properly represent air-sea interactions for adequate representation of the lifetime of both N_2O_5 and $ClNO_2$.

More broadly, we show that direct measurements of trace gas vertical fluxes when combined with *in situ* determinations of the reactive uptake to aerosol particles provides an experimental constraint on the lifetime and reactivity of trace gases to the wide array of available surfaces in the marine boundary layer. These results indicate that under conditions of shallow boundary layer heights, uptake to the ocean surface can outpace uptake to aerosol surfaces, highlighting the vast difference in the chemical composition, morphology, phase, and pH of the aerosol and ocean surface. The results presented here highlight the future utility of combining high sensitivity and precision time-of-flight mass spectrometric measurements of reactant and product pairs with micrometeorological techniques for direct, *in situ* study of chemical reactions

occurring at the air-sea interface. This approach will permit study of complex interfacial processes under ambient conditions, where coupled biological, chemical, and physical mechanisms often prohibit the extension of laboratory results to environmental conditions.

3. Materials and Methods

3.1 Sampling location

Concentration and vertical flux measurements of N_2O_5 and $ClNO_2$ were made at 10 m from the northwest boom of the 330 m Scripps Institution of Oceanography (SIO) Pier during February 2013. Air sampled at this location is impacted by local emissions in the La Jolla cove region as well as regional pollution attributed to both San Diego and Los Angeles. The observations presented here are for time periods were winds were sustained from the west (true wind direction between 205-295°) so as to ensure an ocean fetch. Backward air trajectories indicate that air sampled during these time periods was influenced by the Los Angeles plume, thus sustaining concentrations of N_2O_5 well above that observed in clean, marine air (41).

3.2 N_2O_5 and $ClNO_2$ concentration measurements

N_2O_5 and $ClNO_2$ mixing ratios were measured using chemical ionization time-of-flight mass spectrometry (24), utilizing I^- reagent ion chemistry (25). N_2O_5 sensitivities were determined using the output of a portable N_2O_5 generation system, described previously (42), where N_2O_5 is made *in situ* from the dark reaction of NO_2 and O_3, and subsequent reaction of the NO_3 product with NO_2. $ClNO_2$ sensitivities

were determined by passing the output of the N_2O_5 source over concentrated NaCl slurry for unit conversion of N_2O_5 to $ClNO_2$ (4, 25, 43). We sample N_2O_5 and $ClNO_2$ through a 17 m, 3/8" O.D. PFA tube. The inlet manifold is constructed of fluoropel coated glass, closely resembling that of Ellis et al. (44), where air is drawn through a critical orifice, reducing the sample line pressure to 200 mbar. The resulting mass flow rate (10 slpm) results in a laminar flow profile, with a measured gas exchange time for the inlet of 0.7 s.

3.3 N_2O_5 and $ClNO_2$ flux measurements

Mass spectra, acquired at 80 kHz, were saved at 10 Hz, coincident with measurements of 3D winds acquired with a co-located ultrasonic anemometer sampling at 20 Hz (Gill Instruments, HS-50). Fluxes were determined by the eddy covariance technique (45). In this method, the vertical turbulent flux is equal to the covariance of deviations of vertical wind speed (w) and mixing ratio from the mean (c), $F = \langle w'c' \rangle$. Details on the application of time of flight mass spectrometry to eddy covariance flux measurement can be found elsewhere (46) and described in more detail in the Supplemental Information.

3.4 Time dependent air-sea model

The chemical evolution of the nocturnal boundary layer was tracked using a one time-dependent dimensional box model, where coupled differential equations were solved using custom code written in MATLAB, analyzed with the built in ordinary differential equation solvers. As time propagates in the model, we calculate

the production and loss of NO, NO_2, O_3, N_2O_5, NO_3, HNO_3, $ClNO_2$ to gas-phase and heterogeneous reactions occurring on/within aerosol particles, as well as air-sea exchange with the ocean surface. The model is initialized with concentrations representative of those measured at the SIO pier, and reaction rates from the NASA JPL Chemical Kinetics and Photochemical Data for Use in Atmospheric Studies, Evaluation Number 14. Detailed descriptions of the modelling efforts described here can be found in the supporting information.

4. Acknowledgements

This research was supported by the National Science Foundation CAREER Award to THB (Grant No. AGS-1151430). We thank Byron Blomquist (University of Hawaii) and Joel Thornton (University of Washington) for helpful discussions and Christian McDonald (SIO), Nicole Campbell (UCSD), and Katy Zimmerman (UCSD) for assistance in the set-up for the pier observations.

Chapter 4, in full, is a reprint of the material as it appears in the *Proceedings of the National Academy of Sciences* 2014 with slight modifications. Kim, M.J., Farmer, D.K., and T.H. Bertram (2014), "A controlling role for the air-sea interface". *Proc. Natl. Acad. Sci. U. S. A.*111:3943-3948. The dissertation author was the primary investigator and author of this paper.

Figures

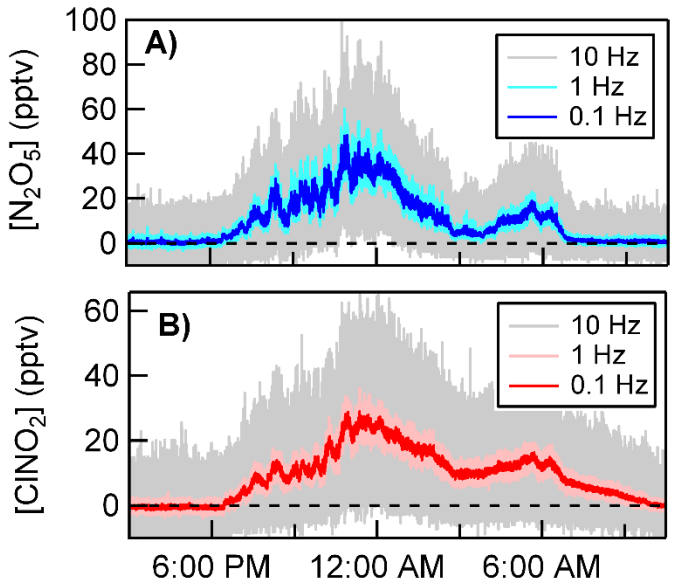

Figure 4.1 N_2O_5 and $ClNO_2$ mixing ratios (a and b) as measured from the SIO pier in La Jolla, CA on 20 February 2013 at 0.1, 1, and 10 Hz time resolution.

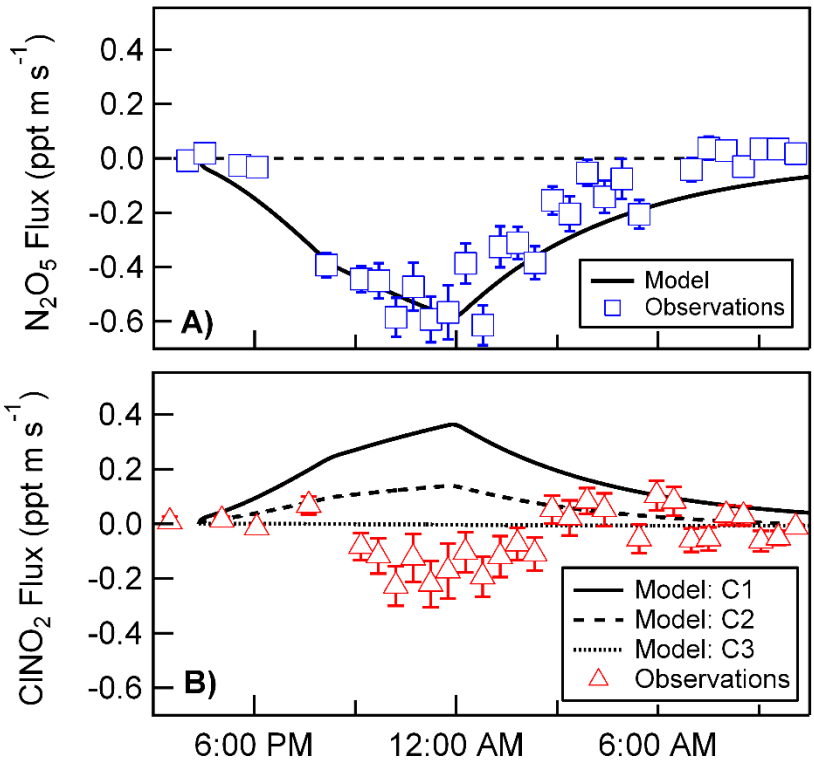

Figure 4.2 Measured vertical fluxes of N_2O_5 and $ClNO_2$. Errors are determined for each 30-minute flux segment as the covariance between vertical wind speed and concentration at lag times significantly longer than the delay (or lag) time. Calculated $ClNO_2$ vertical fluxes (lines, panel b), as determined from the coupled time dependent ocean-atmosphere model, constrained by the measured N_2O_5 vertical fluxes (panel a). Three different model scenarios are shown and described in detail in the supplemental information: C1) (*a priori*) model inputs taken as suggested in the literature (e.g., K_H ($ClNO_2$) = 1.66, Φocean ($ClNO_2$) = 0.8, $k_r = 5 \times 10^6$ s^{-1}, $\delta = 1.5 \times 10^{-6}$ cm), C2) model inputs taken as 90% confidence limits of those suggested in the literature (e.g., K_H ($ClNO_2$) = 0.32, Φocean ($ClNO_2$) = 0.5, $k_r = 2 \times 10^5$ s^{-1}, $\delta = 7.1 \times 10^{-6}$ cm), and C3) same as C2, with Φocean ($ClNO_2$) = 0.

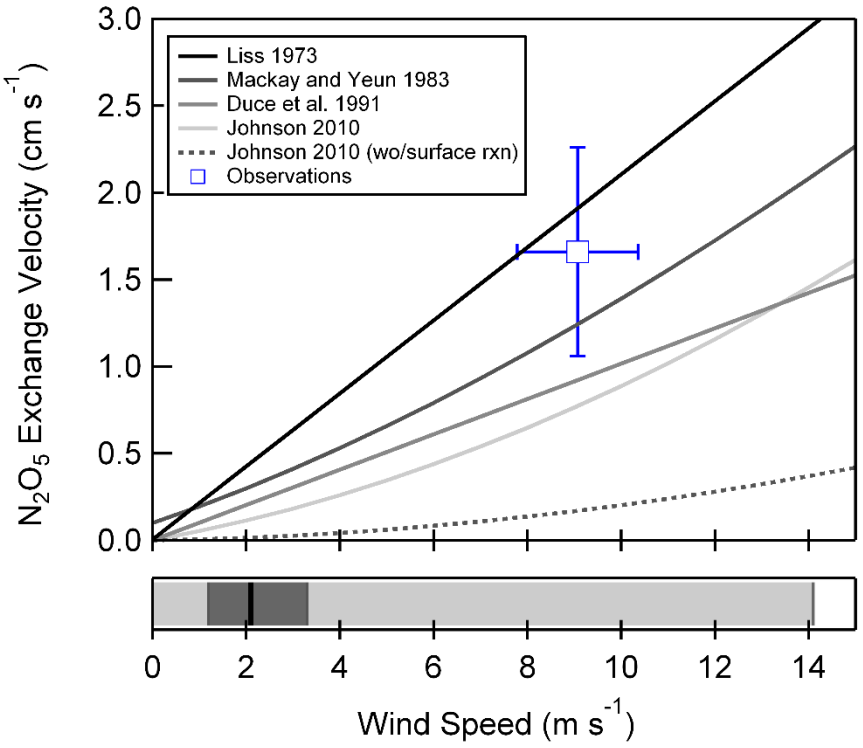

Figure 4.3 Average N_2O_5 exchange velocity (V_{ex}, cm s^{-1}) as a function of 10 m wind speed (m s^{-1}). Modelled exchange velocities, determined *via* E3 [Johnson 2010] are shown using the dimensionless gas over liquid Henry's Law Constant, K_H (N_2O_5) = 1.9 x 10^{-2} with and without incorporation of N_2O_5 hydrolysis (k_r = 5 x 10^6 s^{-1}). Parameterizations of Liss (1973), Mackay and Yeun (1983) and Duce (1991) are also shown for comparison. The bottom panel shows the 2012 annual median (black line), interquartile range (dark grey shaded region) and full range (light grey shaded region) for 10 m wind speed measured at the SIO pier.

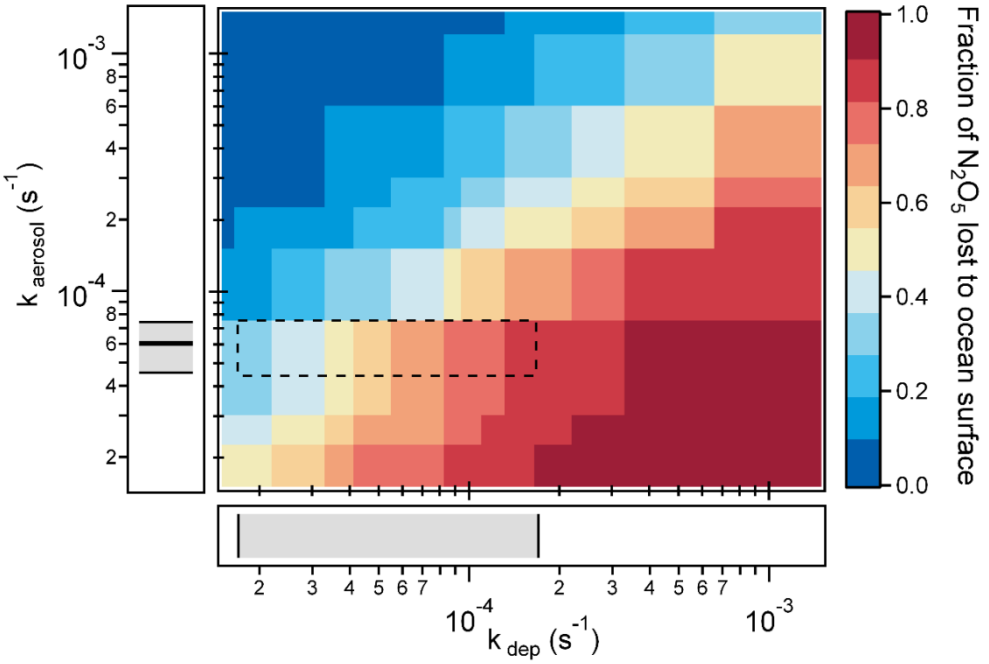

Figure 4.4 Fraction of the total N_2O_5 removal attributed to deposition to the ocean shown as a function of the N_2O_5 deposition rate (k_{dep}) and the heterogeneous loss rate to aerosols ($k_{aerosol}$). The boxed region represents the range in k_{dep} and $k_{aerosol}$ measured at the SIO pier in La Jolla, CA. The median and interquartile range in the observed $k_{aerosol}$ is shown on the ordinate, while the range in the observed k_{dep} (based on a marine boundary layer inversion height (z_i) of 100-1000 m, at an average wind speed of 9.1 ± 1.3 ms^{-1}) is shown on the abscissa.

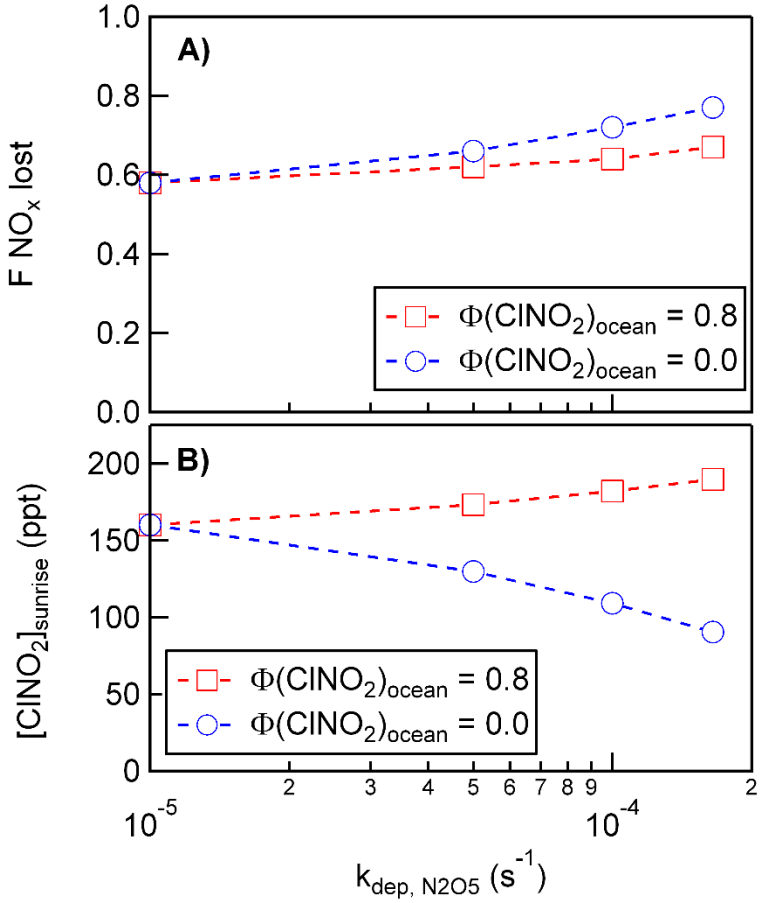

Figure 4.5 (a) Model calculations of the fraction of available NO_x ($[NO_x]_{sunset}$) lost during a 12-hr night and the mixing ratio of $ClNO_2$ at sunrise as a function of the prescribed N_2O_5 exchange velocity and $ClNO_2$ product yield ($\Phi(ClNO_2)_{ocean}$). Calculations were conducted using a 0-D time dependent box model constrained by the mean N_2O_5 reactive uptake coefficients and particle surface area (SA) concentrations measured at this site ($\gamma(N_2O_5)$ = 0.005, SA = 500 μm^2 cm^3). The model was initialized with the following conditions: T_{air} = 283 K, T_{water} = 287 K, $[O_3]_i$ = 60 ppb, $[NO_x]_i$ = 1.0 ppb, $\gamma(NO_3)$ = 0 and NO_3 reactivity = 0.16 min^{-1}.

References

1. Alexander B, *et al.* (2009) Quantifying atmospheric nitrate formation pathways based on a global model of the oxygen isotopic composition ($D^{17}O$) of atmospheric nitrate. *Atmos Chem Phys* 9(14):5043-5056.

2. Behnke W, George C, Scheer V, & Zetzsch C (1997) Production and decay of $ClNO_2$, from the reaction of gaseous N_2O_5 with NaCl solution: Bulk and aerosol experiments. *J Geophys Res-Atmos* 102(D3):3795-3804.

3. Finlayson-Pitts BJ, Ezell MJ, & Pitts JN (1989) Formation of chemically active chlorine compounds by reactions of atmospheric NaCl particles with gaseous N_2O_5 and $ClONO_2$. *Nature* 337(6204):241-244.

4. Osthoff HD, *et al.* (2008) High levels of nitryl chloride in the polluted subtropical marine boundary layer. *Nature Geoscience* 1(5):324-328.

5. Thornton JA, *et al.* (2010) A large atomic chlorine source inferred from mid-continental reactive nitrogen chemistry. *Nature* 464(7286):271-274.

6. Aldener M, *et al.* (2006) Reactivity and loss mechanisms of NO3 and N2O5 in a polluted marine environment: Results from in situ measurements during New England Air Quality Study 2002. *J Geophys Res-Atmos* 111(D23).

7. Huff DM, Joyce PL, Fochesatto GJ, & Simpson WR (2011) Deposition of dinitrogen pentoxide, N2O5, to the snowpack at high latitudes. *Atmos Chem Phys* 11(10):4929-4938.

8. Hinrichsen D (1998) *Coastal Waters of the World: Trends, Threats, and Strategies* (Island Press, Washington).

9. Wagner NL, *et al.* (2012) The sea breeze/land breeze circulation in Los Angeles and its influence on nitryl chloride production in this region. *J Geophys Res-Atmos* 117.

10. Liss PS & Slater PG (1974) Flux of gases across air-sea interface. *Nature* 247(5438):181-184.

11. Carpenter LJ, Archer SD, & Beale R (2012) Ocean-atmosphere trace gas exchange. *Chemical Society Reviews* 41(19):6473-6506.

12. Thornton JA, Braban CF, & Abbatt JPD (2003) N_2O_5 hydrolysis on sub-micron organic aerosols: the effect of relative humidity, particle phase, and particle size. *Physical Chemistry Chemical Physics* 5(20):4593-4603.

13. Bertram TH & Thornton JA (2009) Toward a general parameterization of N_2O_5 reactivity on aqueous particles: the competing effects of particle liquid water, nitrate and chloride. *Atmos Chem Phys* 9(21):8351-8363.

14. Mentel TF, Sohn M, & Wahner A (1999) Nitrate effect in the heterogeneous hydrolysis of dinitrogen pentoxide on aqueous aerosols. *Physical Chemistry Chemical Physics* 1(24):5451-5457.

15. Wahner A, Mentel TF, Sohn M, & Stier J (1998) Heterogeneous reaction of N_2O_5 on sodium nitrate aerosol. *J Geophys Res-Atmos* 103(D23):31103-31112.

16. Anttila T, Kiendler-Scharr A, Tillmann R, & Mentel TF (2006) On the reactive uptake of gaseous compounds by organic-coated aqueous aerosols: Theoretical analysis and application to the heterogeneous hydrolysis of N_2O_5. *Journal of Physical Chemistry A* 110(35):10435-10443.

17. Cosman LM & Bertram AK (2008) Reactive uptake of N_2O_5 on aqueous H_2SO_4 solutions coated with 1-component and 2-component monolayers. *Journal of Physical Chemistry A* 112(20):4625-4635.

18. McNeill VF, Patterson J, Wolfe GM, & Thornton JA (2006) The effect of varying levels of surfactant on the reactive uptake of N_2O_5 to aqueous aerosol. *Atmos Chem Phys* 6:1635-1644.

19. Escoreia EN, Sjostedt SJ, & Abbatt JPD (2010) Kinetics of N_2O_5 hydrolysis on secondary organic aerosol and mixed ammonium bisulfate-secondary organic aerosol particles. *Journal of Physical Chemistry A* 114(50):13113-13121.

20. Roberts JM, *et al.* (2009) Laboratory studies of products of N_2O_5 uptake on Cl^- containing substrates. *Geophysical Research Letters* 36.

21. Griffiths PT, *et al.* (2009) Reactive uptake of N_2O_5 by aerosols containing dicarboxylic acids: Effect of particle phase, composition, and nitrate content. *Journal of Physical Chemistry A* 113(17):5082-5090.

22. Fried A, Henry BE, Calvert JG, & Mozurkewich M (1994) The Reaction Probability of N2o5 with Sulfuric-Acid Aerosols at Stratospheric Temperatures and Compositions. *J Geophys Res-Atmos* 99(D2):3517-3532.

23. Hunter KA & Liss PS (1977) Input of organic material to oceans: Air-sea interactions and organic chemical composition of sea-surface. *Marine Chemistry* 5(4-6):361-379.

24. Bertram TH, *et al.* (2011) A field-deployable, chemical ionization time-of-flight mass spectrometer. *Atmospheric Measurement Techniques* 4(7):1471-1479.

25. Kercher JP, Riedel TP, & Thornton JA (2009) Chlorine activation by N_2O_5: simultaneous, in situ detection of $ClNO_2$ and N_2O_5 by chemical ionization mass spectrometry. *Atmospheric Measurement Techniques* 2(1):193-204.

26. Nelson HH & Johnston HS (1981) Kinetics of the Reaction of Cl with ClNO and $ClNO_2$ and the Photochemistry of $ClNO_2$. *Journal of Physical Chemistry* 85(25):3891-3896.

27. Riedel TP, *et al.* (2012) Nitryl chloride and molecular chlorine in the coastal marine boundary layer. *Environ Sci Technol* 46(19):10463-10470.

28. Fairall CW, Helmig D, Ganzeveld L, & Hare J (2007) Water-side turbulence enhancement of ozone deposition to the ocean. *Atmos Chem Phys* 7:443-451.

29. Johnson MT (2010) A numerical scheme to calculate temperature and salinity dependent air-water transfer velocities for any gas. *Ocean Science* 6(4):913-932.

30. Mackay D & Yeun ATK (1983) Mass-transfer coefficient correlations for volatilization of organic solutes from water. *Environ Sci Technol* 17(4):211-217.

31. Fairall CW, Bradley EF, Hare JE, Grachev AA, & Edson JB (2003) Bulk parameterization of air-sea fluxes: Updates and verification for the COARE algorithm. *Journal of Climate* 16(4):571-591.

32. Robinson GN, Worsnop DR, Jayne JT, Kolb CE, & Davidovits P (1997) Heterogeneous uptake of $ClONO_2$ and N_2O_5 by sulfuric acid solutions. *J Geophys Res-Atmos* 102(D3):3583-3601.

33. Duce RA, *et al.* (1991) The atmospheric input of trace species to the world ocean. *Global Biogeochemical Cycles* 5(3):193-259.

34. Carpenter LJ, *et al.* (2013) Atmospheric iodine levels influenced by sea surface emissions of inorganic iodine. *Nature Geoscience* 6(2):108-111.

35. Heal MR, Harrison MAJ, & Cape JN (2007) Aqueous-phase nitration of phenol by N_2O_5 and $ClNO_2$. *Atmos Environ* 41(17):3515-3520.

36. Faloona I, *et al.* (2005) Observations of entrainment in eastern Pacific marine stratocumulus using three conserved scalars. *Journal of the Atmospheric Sciences* 62(9):3268-3285.

37. Riedel TP, *et al.* (2012) Direct N_2O_5 reactivity measurements at a polluted coastal site. *Atmos Chem Phys* 12(6):2959-2968.

38. Brown SS & Stutz J (2012) Nighttime radical observations and chemistry. *Chemical Society Reviews* 41(19):6405-6447.

39. Saiz-Lopez A & von Glasow R (2012) Reactive halogen chemistry in the troposphere. *Chemical Society Reviews* 41(19):6448-6472.

40. Draxler RR & Rolph GD (2013) HYSPLIT (HYbrid Single-Particle Lagrangian Integrated Trajectory) Model access via NOAA ARL READY Website (NOAA Air Resources Laboratory, Silver Spring, MD).

41. Bertram TH, Thornton JA, & Riedel TP (2009) An experimental technique for the direct measurement of N_2O_5 reactivity on ambient particles. *Atmospheric Measurement Techniques* 2(1):231-242.

42. Thaler RD, Mielke LH, & Osthoff HD (2011) Quantification of nitryl chloride at part per trillion mixing ratios by thermal dissociation cavity ring-down spectroscopy. *Analytical Chemistry* 83(7):2761-2766.

43. Ellis RA, *et al.* (2010) Characterizing a Quantum Cascade Tunable Infrared Laser Differential Absorption Spectrometer (QC-TILDAS) for measurements of atmospheric ammonia. *Atmospheric Measurement Techniques* 3(2):397-406.

44. Baldocchi DD, Hicks BB, & Meyers TP (1988) Measuring biosphere-atmosphere exchanges of biologically related gases with micrometeorological methods. *Ecology* 69(5):1331-1340.

45. Farmer DK, *et al.* (2011) Eddy covariance measurements with high-resolution time-of-flight aerosol mass spectrometry: a new approach to chemically resolved aerosol fluxes. *Atmospheric Measurement Techniques* 4(6):1275-1289.

Supporting Information

Site location and airmass trajectories

Concentration measurements of N_2O_5 and $ClNO_2$ were made at 10 m above sea level from the northwest boom of the 330 m Scripps Institution of Oceanography (SIO) Pier (Latitude 32° 52.0188 N, Longitude 117° 15.4350) during January-February 2013. The SIO pier is located in La Jolla, CA, approximately 20 km north of downtown San Diego. At a length of 330 m, the pier extends well past the region of wave breaking. The 3D sonic anemometer (Gill Instruments Ltd, UK, Model: HS-50) was mounted to the NW boom, extending an additional 4 m off the end of the pier, this effectively eliminating flow distortion caused by the pier itself when winds are between 180-360°. The chemical ionization time-of-flight mass spectrometer (described below) was housed within an existing temperature controlled container at the end of the pier.

Backward air trajectories for the site are computed using the HYSPLIT model (1). As shown in Fig. S4.1, for the intensive sampling period discussed in this paper (20 February 2013), backward air trajectories indicate that the air sampled at SIO pier was primarily from the west/northwest, consistent with local measurements of true wind direction. The trajectory analysis indicates that air sampled at SIO was likely influenced by the Los Angeles plume approximately 6-12 hours prior to sampling.

N_2O_5 and $ClNO_2$ concentration measurements and uncertainties

N_2O_5 and $ClNO_2$ mixing ratios were measured using chemical ionization time-of-flight mass spectrometry discussed in detail previously (2). Here, we utilize I^-

reagent ion chemistry (3), detecting N_2O_5 as the $I^-N_2O_5$ adduct and $ClNO_2$ as the I^-ClNO_2 adduct. N_2O_5 sensitivities were determined using the output of a portable N_2O_5 generation system, described previously (4), where N_2O_5 is made *in situ* from the dark reaction of NO_2 and O_3, and subsequent reaction of the NO_3 product with NO_2. $ClNO_2$ sensitivities were determined by passing the output of the N_2O_5 source over concentrated NaCl slurry for unit conversion of N_2O_5 to $ClNO_2$ (3, 5). In this study, we sample N_2O_5 and $ClNO_2$ through a 17 m, 3/8" O.D. PFA tube. The inlet manifold is constructed of fluoropel coated glass, closely resembling that of Ellis et al. (6). Here, air is drawn through a critical orifice, reducing the sample line pressure to 200 mbar, by a Varian TriScroll 600. The resulting mass flow rate (10 slpm) results in a laminar flow profile, with a measured gas exchange time for the inlet of 0.7 seconds. The hybrid inlet was primarily designed for concentration measurements and run in the laminar flow regime to minimize analyte-wall collisions. As a consequence, the laminar inlet (Re = 2000) displayed frequency attenuation above 1 Hz in laboratory tests and calculations (7). The impact of this on our flux measurements is discussed below.

N_2O_5 and $ClNO_2$ flux measurements and uncertainties

Eddy covariance fluxes were calculated from vertical wind speed and concentration measurements similarly to those described in the literature for other time-of-flight mass spectrometers (8). Mixing ratios of N_2O_5 and $ClNO_2$ were determined by chemical ionization mass spectrometry during a continuous 30 minute

sampling period bookended by 1 minute of background sampling with zero air. For both N_2O_5 and $ClNO_2$, ambient count rates are corrected by subtracting interpolated baseline count rates between zero air sampling periods. The flux is determined as the covariance of vertical wind speed and baseline corrected mass spectrometer signal over a continuous 29.8 minute time period. We note that throughout the flux calculation, the mass spectrometer signal is in units of cps, and the calculated half-hour flux is initially in units of cps·m/s. This half-hour flux is converted to mixing ratio by applying an N_2O_5 and $ClNO_2$ sensitivity factor determined by laboratory experiments described previously. We note that this is mathematically identical to calculating the flux in units of concentration. The temporal difference between the sonic anemometer sampling an airmass and the CI-ToFMS measurement (i.e. the time taken for air to flow through the sampling line and into the mass spectrometer) is considered in the flux calculations by applying a time lag to the anemometer data. The lag time is calculated by identifying using an autocorrelation analysis (9). Average lagtimes during significant (nocturnal) flux periods were 1.7 seconds, similar to the 0.7 second lagtime calculated from inlet residence time (Fig. S4.3).

The error for each half-hour flux was determined empirically from baseline fluctuations in the cross correlation function by calculating the covariance between vertical wind speed and mass spectrometer signal at lag times of 90 to 120 seconds, significantly longer than the calculated lag time (10). Based on this calculated error (σ_{flux}), we determine a detection limit for each half-hour flux measurement period as 2 x σ_{Flux} (8). A flux detection limit was computed from the mean covariance during the same extended lag periods. Detection limits ranged from 0.0026 to 4.9 ppt m/s. To

test the stationarity criterion for eddy covariance calculations, we compared the half hour flux measurement with the mean of six consecutive 5-minute fluxes (11). If the overall flux and mean of the 5-minute periods do not agree within 30%, 12 N_2O_5 and 9 $ClNO_2$ half-hour flux periods are rejected out of the total 43 flux periods. We note that all of the rejected flux periods have small or near-zero fluxes. If the rejection criterion is raised to 35%, 8 of the N_2O_5 and 9 of the $ClNO_2$ flux periods are rejected. For the data reported here, a 30% rejection criteria was applied.

Spectral Analysis

Comparison of power spectra and cospectra between the sensible heat flux and the N_2O_5 and $ClNO_2$ fluxes demonstrate the validity of applying eddy covariance flux calculations to the trace gas datasets (Fig. S4.4, S4.5). The cumulative flux contributions as a function of frequency (ogive, Fig. S4.4) demonstrate the similarity in frequency-dependence for all three scalars, with eddies with frequencies between 0.02 and 0.3 Hz carrying the majority of the trace gas flux. Little or no attenuation is observed for N_2O_5, while cospectra and ogives of $ClNO_2$ suggest some loss of flux at the high frequencies (>3 Hz). This attenuation is expected as the laminar flow in the sampling lines will cause smearing of high frequency fluctuations. However, comparison to the sensible heat flux shows that 86-96% ($ClNO_2$ and N_2O_5 respectively) of the total flux occurs at frequencies less than 1 Hz, confirming that while present, attenuation introduces only a small systematic bias (i.e. underestimation of flux) to the flux data. Due to this small error and the difficulties in predicting spectra for reactive trace gases, we do not apply a correction to the fluxes. The

frequency-multiplied cospectra (e.g. Fig. S4.5) demonstrate the clearly distinguishable flux signal. The negative cospectral power density in Fig. S4.5 indicates the N_2O_5 is depositing from the atmosphere to the ocean surface. Similar to the ogive plots, the cospectra show that the bulk of the flux signal is carried by eddies in the 0.02 to 0.2 Hz range. For a wind speed of 10 m/s, this corresponds to eddies in the nocturnal boundary layer on the order of 50 - 500 m.

Supplemental Figures

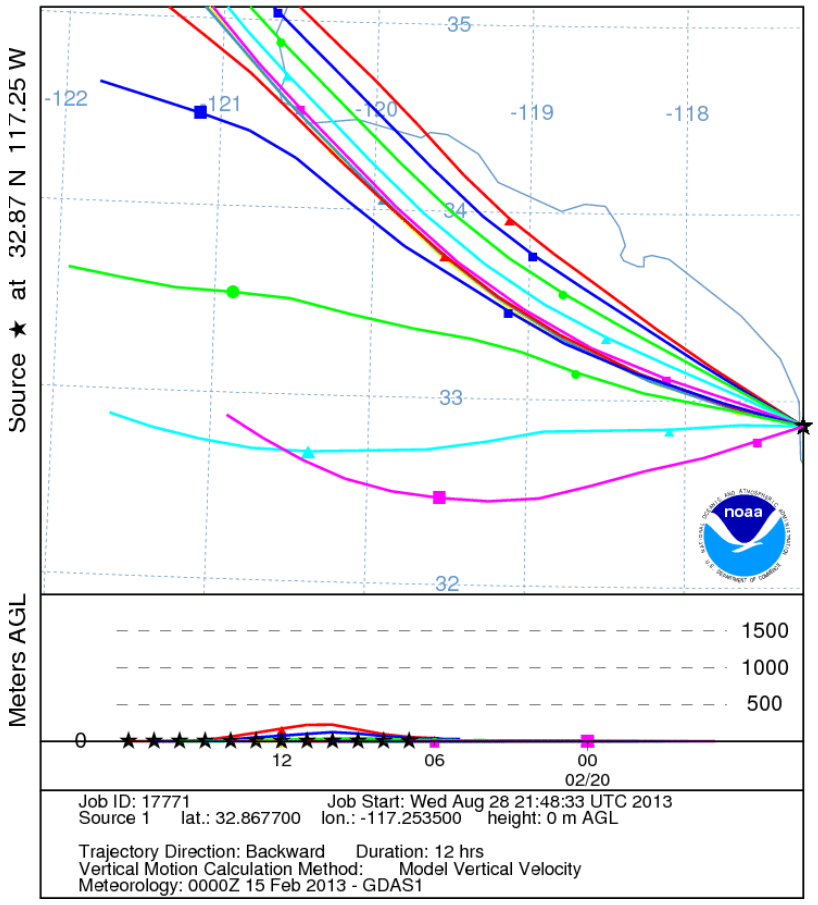

Figure S4.6 HYSPLIT back trajectories for the night of 20 February 2013, indicating persistent north westerly winds (1). Each marking represents a 6 hour time interval with the trajectories terminating at the SIO pier (32.87° N, -117.25° W).

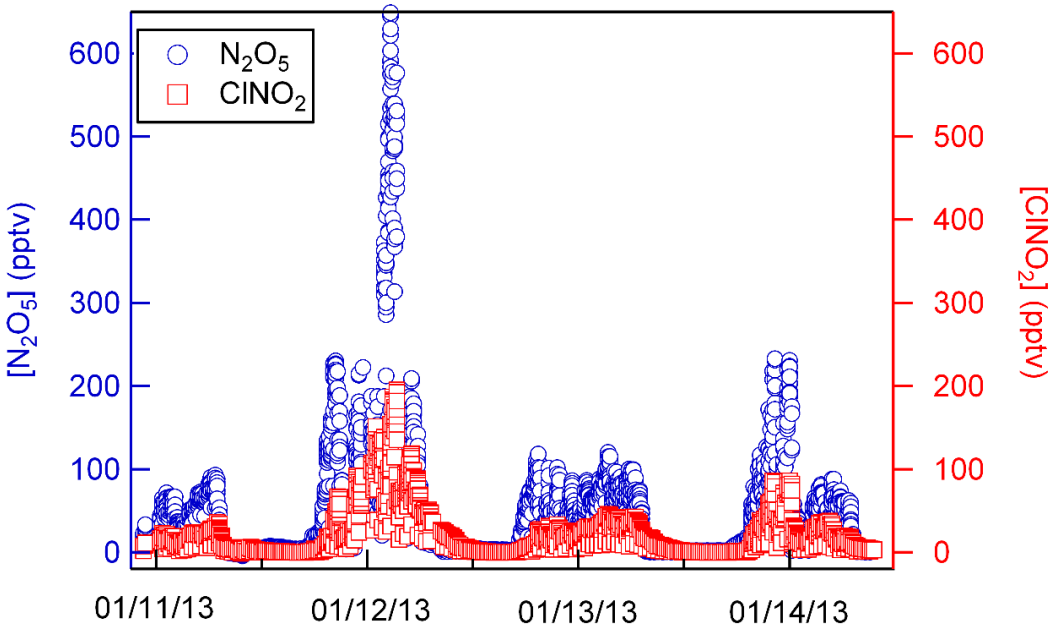

Figure S4.7 Characteristic time series of N_2O_5 and $ClNO_2$ as sampled from the SIO pier, indicating large night-night variability in the observed mixing ratios.

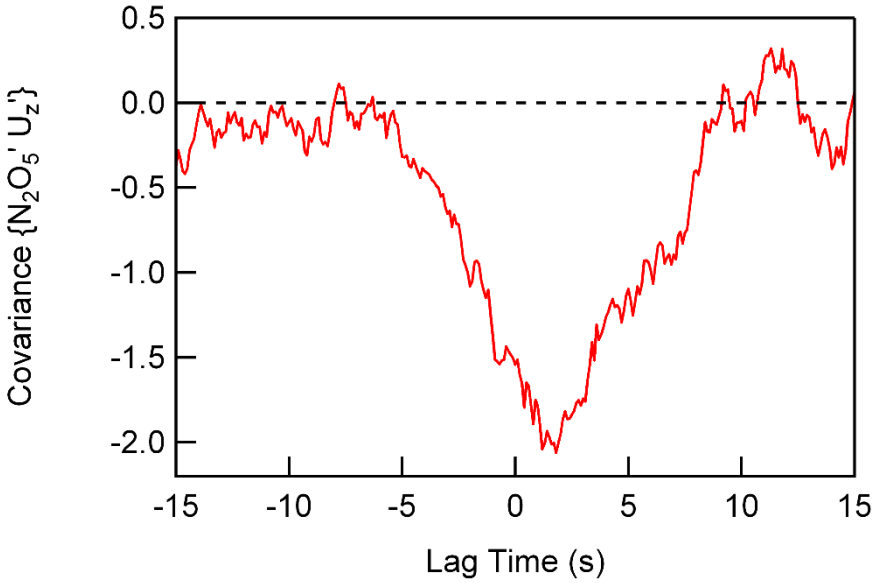

Figure S4.8 The correlation between N_2O_5 and vertical wind speed as a function of lagtime for the flux period 20:55 to 21:25 on 20 February 2013 shows that the maximum absolute covariance occurs at 1.2 seconds.

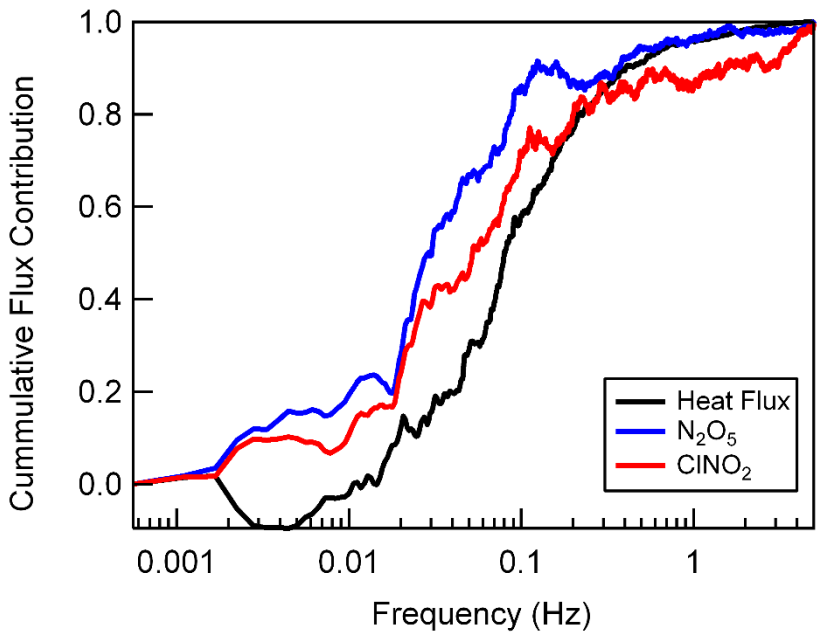

Figure S4.9 A representative ogive, or normalized cumulative flux distribution, for N_2O_5, $ClNO_2$ and sensible heat flux between 21:57 to 22:27 on 20 February 2013.

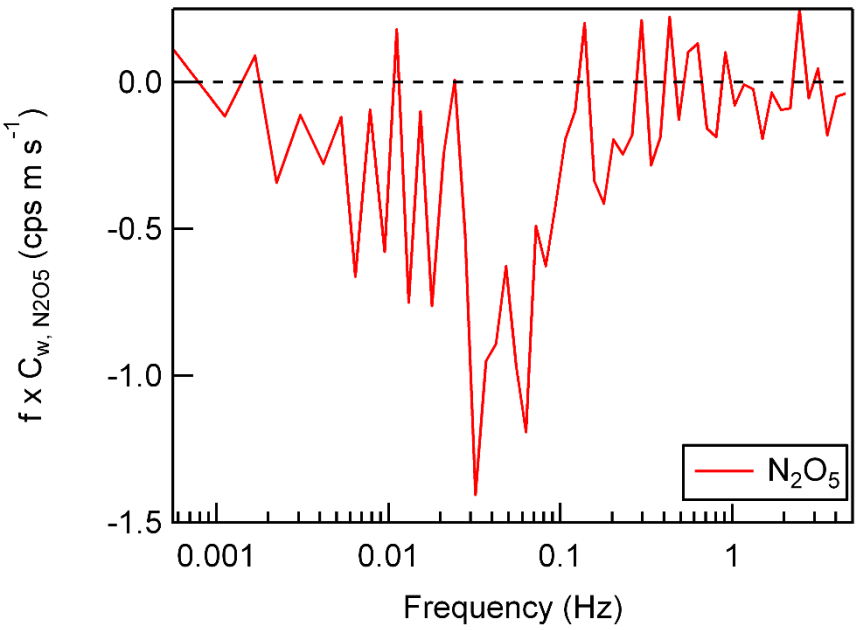

Figure S4.10 Cospectral density of N_2O_5 and vertical wind speed for the flux period between 21:57 to 22:27 on 20 February 2013 as a function of frequency demonstrates that the deposition of N_2O_5, with the majority of the flux signal carried by eddies in the 0.02 - 0.2 Hz range and negligible contribution of white noise.

Supplemental References

1. Draxler RR & Rolph GD (2013) *HYSPLIT (HYbrid Single-Particle Lagrangian Integrated Trajectory) Model access via NOAA ARL READY Website (http://www.arl.noaa.gov/HYSPLIT.php)* (NOAA Air Resources Laboratory, College Park, MD).

2. Bertram TH*, et al.* (2011) A field-deployable, chemical ionization time-of-flight mass spectrometer. *Atmospheric Measurement Techniques* 4(7):1471-1479.

3. Kercher JP, Riedel TP, & Thornton JA (2009) Chlorine activation by N_2O_5: simultaneous, in situ detection of $ClNO_2$ and N_2O_5 by chemical ionization mass spectrometry. *Atmospheric Measurement Techniques* 2(1):193-204.

4. Bertram TH, Thornton JA, & Riedel TP (2009) An experimental technique for the direct measurement of N_2O_5 reactivity on ambient particles. *Atmospheric Measurement Techniques* 2(1):231-242.

5. Mielke LH, Furgeson A, & Osthoff HD (2011) Observation of $ClNO_2$ in a mid-continental urban environment. *Environ Sci Technol* 45(20):8889-8896.

6. Ellis RA*, et al.* (2010) Characterizing a Quantum Cascade Tunable Infrared Laser Differential Absorption Spectrometer (QC-TILDAS) for measurements of atmospheric ammonia. *Atmospheric Measurement Techniques* 3(2):397-406.

7. Lenschow DH & Raupach MR (1991) The attenuation of fluctuations in scalar concentrations through sampling tubes. *J Geophys Res-Atmos* 96(D8):15259-15268.

8. Farmer DK, *et al.* (2011) Eddy covariance measurements with high-resolution time-of-flight aerosol mass spectrometry: a new approach to chemically resolved aerosol fluxes. *Atmospheric Measurement Techniques* 4(6):1275-1289.

9. Farmer DK, Wooldridge PJ, & Cohen RC (2006) Application of thermal-dissociation laser induced fluorescence (TD-LIF) to measurement of HNO_3, sigma alkyl nitrates, sigma peroxy nitrates, and NO_2 fluxes using eddy covariance. *Atmos Chem Phys* 6:3471-3486.

10. Wienhold FG, Welling M, & Harris GW (1995) Micrometeorological measurement and source region analysis of nitrous-oxide fluxes from an agricultural soil. *Atmos Environ* 29(17):2219-2227.

11. Foken T & Wichura B (1996) Tools for quality assessment of surface-based flux measurements. *Agr Forest Meteorol* 78(1-2):83-105.

Conclusion

This dissertation has provided novel observational constraints on the marine sources and sinks of two classes of reactive trace gases: biogenic volatile organic compounds (BVOCs) and reactive nitrogen species (NOy ≡ NOx + alkyl nitrates + N_2O_5 + $ClNO_2$ + peroxynitrates + nitric acid + others). Observations made under ambient and realistic, simulated marine conditions were performed on a custom-built chemical ionization time-of-flight mass spectrometer (CI-ToFMS) using a suite of different reagent ion chemistries. Sampling conditions represented both pristine and polluted conditions. Here, the research results will be reviewed, followed by their broader implications for atmospheric chemistry and compelling future directions for these lines of questioning.

Chapter 1

Previous chemical ionization methods for the sensitive detection of BVOCs such as isoprene and monoterpenes have typically employed ionization reactions that result in significant fragmentation. To this end, in Chapter 1, benzene dimer cations were revisited as a chemical reagent for the sensitive ionization of novel BVOC molecules (i.e. DMS, sesquiterpenes). They were also characterized on the CI-ToFMS for previously known targets such as isoprene and α-pinene, the most common monoterpene isomer. Laboratory results indicated good sensitivity, varying humidity dependencies and product ions at nominal or clustered product ions. In-field

comparison to simultaneous measurements of DMS in the remote boundary layer showed excellent agreement (R^2 = 0.80) providing good validation for BVOC measurements in pristine environments.

The development of a sensitive and accurate detection method for BVOCs such as DMS and isoprenoids (i.e. isoprene, monoterpenes and sesquiterpenes) represents an important technical advancement that may aid the characterization of these poorly understood yet highly reactive species in pristine marine and continental environments. Of particular intrigue are their potential application to the quantification of sesquiterpene molecules. Sesquiterpenes are a class of isoprenoid isomers whose lifetimes are thought to range from seconds to minutes, which is even more reactive than isoprene and monoterpene species that are known to drive global SOA production rates. Gains in sensitivity presented by benzene dimer cations over traditional methods also have the potential to drive increased frequency of marine observations of BVOC in particular, where isoprenoid mixing ratios are typically several factors lower over continental regions. These gains also allow its application to rich but analytically challenging measurement methods such as eddy covariance, which are discussed in Chapter 2.

Chapter 2

Benzene dimer cations were utilized during the High Wind Gas Exchange Study (HiWinGS) while targeting direct measurements of BVOC air-sea exchange rates over this five-week deployment in low chlorophyll-α and high wind conditions. Eddy covariance flux measurements of DMS and monoterpenes were positive,

indicating that the ocean is a source for these two well-known secondary organic aerosol (SOA) precursors. Measured DMS emission rates agreed well ($R^2 = 0.69$) with observations from the University of Hawaii's atmospheric pressure ionization mass spectrometer with an isotopically-labelled standard (APIMS-ILS). Monoterpene emission rates were positive in remote sampling regions several hundred nautical miles from shore confirming their marine origin. However, emission rates were elevated in coastal regions which is likely due to both elevated primary productivity as well as possible continental influences. Due to the low abundance of chlorophyll-α over the duration of the sampling period, the positive identification of monoterpenes suggests that this traditional biological marker may be a poor indicator for the production of these higher isoprenoids in the water column.

This work represents the first direct measurement of monoterpene air-sea exchange and confirms that the surface ocean is a source for these highly reactive SOA precursors. The lack of correlation between monoterpene and isoprene emission rates supports results from various laboratory tests that indicate the production rates of these two molecules can vary with different environment stressors, between different species and even amongst related microbial strains. Further, the decoupling of monoterpene emissions from measured chlorophyll-α concentrations suggests that its current parameterization in numerical models warrants revisiting the biochemical, trophic or environmental controls over monoterpene net emission rates. Future investigations would benefit from sampling from a larger range of environmental conditions as well as better biological and chemical characterization of the water column to examine the drivers of monoterpene and isoprene production.

Chapter 3

The NO_x limited remote marine boundary layer is alternately characterized by regions of net ozone production and destruction largely determined by NO_x from the chemical, thermal and photolytic processing of reactive nitrogen (NO_y). In equatorial regions, observations of alkyl nitrate indicate these molecules comprise a significant fraction of NO_y. Photochemical production mechanisms have provided plausible production mechanisms to account for the high levels of supersaturation (up to 800%) in the surface layer. However, elevated levels of alkyl nitrates below the mixed layer indicate that an alternative light-independent production pathway exists at depth. Alkyl nitrate measurements taken from the headspace of a physically and biologically realistic oceanic mesocosm demonstrated short-chained, even carbon number alkyl nitrates were highly correlated ($R^2 > 0.89$) with heterotrophic bacteria levels. Subsequent flask experiments utilizing bacterial monocultures in both raw and sterile seawater matrices exhibited behavior consistent with the enzymatic processing of a pool of dissolved organic matter or amino acids to produce two radical precursors for the formation of alkyl nitrates, the alkyl peroxy radical and nitric oxide.

Genes for these enzymes are widely distributed among genetic sequences of marine bacterial strains, indicating a potentially significant and widespread source of these critical ozone precursor molecules. Projections of future marine bacteria abundance indicate elevated levels of strains by as much as 50% in certain regions. The potential impacts on future distributions of short-lived greenhouse gases and oxidants in the remote marine boundary layer could be influenced by these and other

significant biogeochemical shifts. Future investigations into this production mechanism should simplify the modeled marine systems further by raising bacterial strains in matrices of varying levels of amino acids or fatty acid substrates. Confirming the expression of the nitric oxide synthase gene expression would also be a valuable confirmation of this enzymatically mediated production pathway.

Chapter 4

In the polluted coastal atmosphere, physical removal of N_2O_5, a reactive nitrogen species, can play a controlling role in determining the regional NO_x budget. The heterogeneous uptake of N_2O_5 on sea spray aerosol particles are known to be a major loss process whose impacts on NO_x and the halogen budget is dependent on the chemistry of an individual sea spray particle. Chapter 4 demonstrated that the sea surface microlayer also acts as a sink for N_2O_5, but unlike sea spray aerosol, does not regenerate NO_x or activate halogens through the production of photolabile nitryl halides, such as $ClNO_2$. Modeled results showed air-sea exchange comprises 26-42% of total N_2O_5 loss for typical nocturnal conditions at SIO Pier and up to 15% loss of NO_x and 20% loss of $ClNO_2$ at sunrise.

These results have significant potential implications for air quality modelling in coastal polluted regions where air-sea exchange is not current included as a loss process for this tropospheric ozone precursor. About 44% of the global population lives within 200 km of a coastline, where accurate understanding of ozone production and NO_x emissions dictate action on behalf of public health.

Beyond these broader impacts, measurements of surface reactive gas exchange also provide mechanistic insights into the physical controls of air-sea exchange. Air sea exchange rates are controlled at the air-sea interface by diffusive transfer rates of gaseous molecules across either air- or water-side laminar sublayers. Thus, air-sea exchange can typically be categorized as either water or air-side controlled, typically based on their solubility or reactivity. Few are a mixture of both, for example, acetone. Measurements of water-side controlled gases are more common (i.e. CO_2, BVOCs, noble gases, inert tracers) and thus their parameterizations are well-developed particularly in low to moderate wind speeds. Air-side controlled gases tend to be very water soluble or surface active, thus are harder to measure and less understood. Previous measurements of air-side controlled gases have been limited primarily to water vapor and ozone. While N_2O_5 is not a very soluble molecule, its hydrolysis rate is extremely fast and thus, overall vertical flux is only limited by diffusion across the atmospheric laminar sublayer. In this manner, the application of the CI-ToFMS to eddy covariance measurements of a suite of reactive trace gases of varying physical and chemical properties (in identical environmental conditions) could provide valuable insights to the controls of air-sea exchange and improve more physically based parameterizations.